D O C T O R A L   T H E S I S

CHARACTERIZATION OF VISCOELASTIC PROPERTIES OF BITUMEN BY MEANS OF NANOINDENTATION AS BASIS FOR MULTISCALE MODELING OF ASPHALT

D I S S E R T A T I O N

CHARAKTERISIERUNG DER VISKOELASTISCHEN EIGENSCHAFTEN VON BITUMEN MITTELS NANOINDENTATION ALS GRUNDLAGE FÜR DIE MEHRSKALENMODELLIERUNG VON ASPHALT

---

ausgeführt zum Zwecke der Erlangung des akademischen Grades eines
Doktors der technischen Wissenschaften

eingereicht an der Technischen Universität Wien
Fakultät für Bauingenieurwesen

von

Dipl.-Ing. Andreas Jäger
Matrikelnummer 9825014
Anzendorf 18, A - 3382 Loosdorf, Österreich

Referent: Univ.Prof. Dipl.-Ing. Dr.techn. Roman Lackner
              FG Computational Mechanics, Technische Universität München
              Arcisstraße 21, 80333 München, Deutschland

Koreferent: Univ.Prof. Dipl.-Ing. Dr.techn. Philippe Kurt Zysset
              Institut für Leichtbau und Struktur-Biomechanik,
              Technische Universität Wien
              Gußhausstraße 27-29, 1040 Wien, Österreich

Wien, im März 2008   ....

Danksagung

Diese Dissertation entstand im Rahmen meiner Tätigkeit als Forschungsassistent am Institut für Mechanik der Werkstoffe und Strukturen der Technischen Universität Wien und als Mitarbeiter im Christian Doppler (CD) Laboratorium für "Gebrauchsverhaltensorientierte Optimierung flexibler Straßenbefestigungen". Das Gelingen dieser Arbeit verdanke ich zahlreichen Kollegen und Freunden bei denen ich mich mit diesen Zeilen herzlich bedanken will.

Ganz besonderer Dank gilt meinem Betreuer Prof. Roman LACKNER, der maßgebend an der Erstellung dieser Dissertation beteiligt war. Er hat mich schon während meiner Diplomarbeit hervorragend betreut und ist mir immer mit Rat und Tat zur Seite gestanden.

Herrn Prof. Philippe Zysset danke ich recht herzlich für die Übernahme des Koreferats meiner Arbeit.

Auch Prof. Ronald BLAB, Klaus STANGL, Karl KAPPL, Markus SPIEGL und Michael WISTUBA, mit denen ich im CD-Labor zusammengearbeitet habe, möchte ich an dieser Stelle nicht unerwähnt lassen. Das gute Arbeitsklima und die fruchtvollen Diskussionen werden mir in guter Erinnerung bleiben.

Das Arbeiten am Institut hat mir immer großen Spass bereitet. Sei es im Institutsalltag, beim gemeinsamen Mittagessen, bei den gelegentlichen Kaffeejausen oder bei der Organisation und Durchführung von Konferenzen, das Klima war immer ausgezeichnet. Dafür gebührt einerseits allen Kollegen und den beiden Institutsvorständen, Prof. Josef EBERHARDSTEINER und Prof. Herbert MANG, aber ganz besonders Martina PÖLL Dank. Sie war und ist die gute Seele des Instituts und hat alle möglichen und unmöglichen Probleme immer prompt und unbürokratisch erledigt.

Bei Elisabeth AIGNER und Josef FÜSSL möchte ich mich speziell bedanken. Ich betrachte es als besonderes Privileg mit Kollegen arbeiten zu dürfen, die ich auch zu meinen besten Freunden zähle.

Nicht zuletzt bedanke ich mich bei meinen Eltern, Freunden, Verwandten und Bekannten die mich die letzten Jahre begleitet haben und mir abseits des Studiums immer eine große und wichtige Stütze waren.

Kurzfassung

Im Rahmen des Christian Doppler Laboratoriums für "Gebrauchsverhaltensorientierte Optimierung flexibler Straßenbefestigungen", das 2002 an der Technischen Universität Wien gegründet wurde, wird ein Mehrskalenmodell für Asphalt entwickelt. Das Ziel dieses Mehrskalenmodells ist die Verknüpfung des makroskopischen Verhaltens von Asphalt mit der Materialzusammensetzung und den Materialeigenschaften der einzelnen Bestandteile auf niedrigeren Betrachtungsebenen. Diese Dissertation, die vier Publikationen enthält, beschäftigt sich mit der Identifikation von Materialeigenschaften auf der niedrigsten Ebene der Betrachtung des zuvor erwähnten Mehrskalenmodells, der *Bitumen*-Ebene. Zu diesem Zweck wird die Nanoindentation (NI) eingesetzt. Während sich die Publikationen A, B und C mit der Entwicklung von neuen Methoden zur Bestimmung von viskoelastischen Materialparametern auf Basis von NI-Versuchsdaten beschäftigen, wird in Publikation D das thermo-rheologische Verhalten von Bitumen und seinen Phasen untersucht:

- Die Form der Indenterspitze hat einen offensichtlichen Einfluss auf die zu bestimmenden Modellparameter. In **Publikation A** ("Identifizierung von viskoelastischen Eigenschaften mittels Nanoindentation unter Berücksichtigung der realen Spitzengeometrie") wird dieser Einfluss untersucht. Dabei werden bestehende Modelle zur Bestimmung von viskoelastischen Modellparametern auf durch die Standardkalibrierung des Nanoindenters bekannte allgemeine Spitzenformen erweitert. Basierend auf der analytischen Lösung der Eindringung einer starren Spitze in einen viskoelastischen Halbraum, werden die Modellparameter mittels Rückrechnung von der gemessenen Last-Eindringungsgeschichte bestimmt. Die vorgestellte Methode wird durch die Bestimmung der viskoelastischen Eigenschaften von Bitumen im Bereich kleiner Zeitmaßstäbe veranschaulicht.

- Im allgemeinsten Fall zeigt das indentierte Material sowohl viskoelastische wie auch plastische Deformationen. In **Publikation B** ("Bestimmung der viskoelastischen Eigenschaften auf kleinen Längenmaßstäben mittels Nanoindentation unter Berücksichtigung von viskoelastisch-plastischem Materialverhalten") wird der Effekt von plastischen Deformationen auf die identifizierten viskoelastischen Modellparameter untersucht. Beginnend mit vorhandenen analytischen Lösungen für eine starre Spitze, die in ein rein viskoelastisches Material eindringt, werden zwei Methoden zur Berücksichtigung von plastischen Deformationen im Rahmen der Bestimmung von viskoelastischen Modellparametern präsentiert. Bei der so genannten Doppelindentation werden im ersten Lastzyklus plastische Deformationen induziert, während für den zweiten Lastzyklus rein viskoelastische Deformationen angenommen werden. Das Ziel der Verwendung von kugelförmigen Spitzenformen statt den herkömmlichen pyramidenförmigen Spitzen ist auf der anderen Seite die Vermeidung von plastischen Deformationen während dem Indentationsprozess. Die Leistungsfähigkeit beider

Methoden wird durch die Bestimmung der viskoelastischen Parameter von drei unterschiedlichen Polymeren veranschaulicht.

- Für niedrig viskose Materialien können zur Parameteridentifikation statt der üblichen Kriechversuche auch zyklische Nanoindentationsversuche eingesetzt werden. In **Publikation C** ("Identifikation von viskoelastischen Modellparametern mittels zyklischer Nanoindentation") wird eine Methode zur Bestimmung von viskoelastischen Modellparametern aus Versuchsdaten von zyklischen Nanoindentationsversuchen vorgestellt. Dabei werden der komplexe Modul und der Phasenwinkel des getesteten Materials aus den gemessenen Amplituden der Kraft und der Eindringung und der Phasenverschiebung beider Maximalwerte bestimmt. Die Parameter für ein bestimmtes viskoelastisches Modell werden über den Vergleich der experimentell erhaltenen Speicher- und Verlustmoduli mit den zugehörigen analytischen Ausdrücken des jeweiligen Modells ermittelt. Die vorgestellte Methode wird auf Polyethylen angewendet, und die erhaltenen Ergebnisse werden mit Ergebnissen von statischen Nanoindentations-Kriechversuchen und makroskopischen Biegebalkenrheometer-Versuchen evaluiert.

- Die Identifizierung der viskoelastischen Eigenschaften von Bitumen und seinen Materialphasen wird schließlich in **Publikation D** ("Charakterisierung von Bitumen auf der Mikroebene – Rückrechnung von viskoelastischen Eigenschaften mittels Nanoindentation") vorgestellt. Zu diesem Zweck wird die Methode zur Bestimmung der viskoelastischen Materialparameter, die in Publikation A präsentiert wurde, auf zwei fraktionale Kriechmodelle erweitert, die zur Beschreibung des viskoelastischen Verhaltens von Bitumen verwendet werden. Es wird eine Parameterstudie bezüglich des Einflusses der Belastungsrate, der Maximallast und der Temperatur vorgestellt. Während die Belastungsrate nur einen geringfügigen Einfluss auf die Parameter hat, hat eine Erhöhung der Maximallast eine signifikante Variation der identifizierten Modellparameter zur Folge. Dieser Effekt wird durch die Mikrostruktur von Bitumen, die eine ähnliche charakteristische Länge wie die Nanoindentationsversuche hat, erklärt. Diese Mikrostruktur wird durch die Anwendung der so genannten Raster-Indentationstechnik visualisiert und zeigt eine hochviskose strangartige Struktur, die in eine niedrigviskose Matrix eingebettet ist.

Die für Bitumen und seine Phasen erhaltenen viskoelastischen Parameter dienen als Eingangsgrößen im Rahmen des zuvor erwähnten Mehrskalenmodells, das einerseits die Mikrostruktur mit den mechanischen Eigenschaften von Bitumen verknüpft, und andererseits den Einfluss von Bitumen auf das makroskopische Verhalten von Asphalt erfasst.

Abstract

Within the Christian Doppler Laboratory for "Performance Based Optimization of Flexible Pavements", which was installed in 2002 at Vienna University of Technology, a multiscale model for asphalt is developed. The aim of this multiscale model is to relate the macroscopic behavior of asphalt to the material composition and the properties of constituents at finer scales of observation. This thesis, comprising four publications, deals with the identification of material properties at the finest observation scale introduced within the mentioned multiscale model, i.e., the *bitumen*-scale. For this purpose, the nanoindentation (NI) technique is employed. Whereas Publications A, B, and C focus on the development of novel methods for the identification of viscoelastic parameters from NI-test data, Publication D is concerned with the characterization of the different material phases of bitumen and their thermo-rheological behavior:

- Obviously, the shape of the indenter tip has an impact on the identified model parameters. In **Publication A** ("Identification of viscoelastic properties by means of nanoindentation taking the real tip geometry into account") this impact is investigated by extending schemes for identification of viscoelastic model parameters towards general tip geometries, accessible through the calibration of the NI-testing equipment. Based on the analytical solution for the penetration of a rigid tip into a viscoelastic halfspace, model parameters are determined via back-calculation from the measured load-penetration history. The presented approach is illustrated by the identification of short-term viscoelastic properties of bitumen.

- However, in the most general case, the penetrated material exhibits both viscoelastic and plastic deformation. In **Publication B** ("Finer-scale extraction of viscoelastic properties from nanoindentation characterized by viscoelastic-plastic response") the effect of plastic deformation on the identification of viscoelastic model parameters is investigated. Starting from existing analytical solutions for a rigid tip penetrating a material experiencing viscoelastic deformation only, two methods for the consideration of plastic deformation during the identification of viscoelastic model parameters are presented. As regards the so-called double-indentation technique, plastic deformation is induced during the first load cycle, while exclusively viscoelastic deformation is assumed in the course of the second load cycle. The aim of using spherical indenter geometries instead of commonly used pyramidal indenters, on the other hand, is to avoid plastic deformation during the indentation process. The performance of both methods is illustrated by the identification of viscoelastic parameters of three different types of polymers.

- In case of materials exhibiting large viscous deformation, cyclic nanoindentation may be employed for parameter identification instead of (static) nanoindentation creep tests. In **Publication C** ("Identification of viscoelastic model parameters by

means of cyclic nanoindentation testing") cyclic nanoindentation for identification of viscoelastic material parameters is presented. Hereby, the complex modulus and the phase angle of the material sample are determined from the measured amplitudes of force and penetration and the phase shift between the peak values. The parameters for a specific viscoelastic model are obtained by comparing the experimentally-obtained storage and loss moduli with the analytical expressions for the respective viscoelastic model. The proposed technique is illustrated for low-density polyethylene, and assessed by (static) nanoindentation creep tests and macroscopic bending beam rheometer tests.

- Finally, the identification of viscoelastic properties of bitumen and its material phases is presented in **Publication D** ("Microscale characterization of bitumen – back-analysis of viscoelastic properties by means of nanoindentation"). For this purpose, the back-analysis scheme proposed in Publication A is extended towards consideration of two fractional creep models, employed for the representation of the viscoelastic behavior of bitumen. A parameter study focusing on the influence of loading rate, maximum load, and temperature on the identified model parameters is presented. Whereas the loading rate is found to show marginal influence on the parameters, the increase in the maximum load results in a significant variation in the identified model parameters. This effect is explained by the bitumen microstructure present at the scale of NI testing. This microstructure is visualized by the so-called grid indentation technique, showing a high-viscous string-like structure embedded into a low-viscous matrix.

The obtained viscoelastic parameters for bitumen and its phases shall serve as input for upscaling within the aforementioned multiscale model for asphalt, finally enabling the link between the bitumen microstructure and its mechanical properties, on the one hand, and the macroscopic behavior of asphalt, on the other hand.

Contents

Introductory remarks

Industrial context

Due to the continuously increasing road traffic within the European Union and changing loading conditions as a consequence of new trends in the automobile and tire industry, new prediction tools for the performance assessment of the road infrastructure are required. As regards flexible pavements, the performance strongly depends on the complex thermo-rheological behavior of asphalt consisting of bitumen as the binder material, aggregates, and air voids. The main failure mechanisms affecting the performance of pavements are rutting at higher temperatures, cracking at low temperatures, and fatigue failure under repeated load cycles (see Figure 1 for the governing failure mechanisms). The proper-
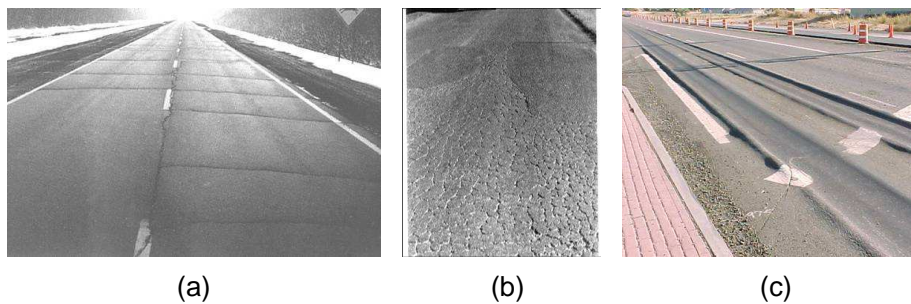
Figure 1: Governing failure mechanisms for flexible pavements: (a) low-temperature cracking, (b) fatigue failure under repeated load cycles, and (c) rutting at high temperatures

ties of bitumen, which define the aforementioned thermo-rheological behavior, provide the low viscosity at high temperatures ($T > 135$ °C), necessary for the construction and compaction of high-quality asphalt layers. The viscosity of bitumen increases for decreasing temperatures, and should be significantly higher at temperatures of about 70 °C in order to minimize the development of permanent deformation (rutting) during hot summer periods. The increase of viscosity and, hence, the increase of stiffness are, on the other hand, unfavorable for the low-temperature performance of asphalt. Insufficient relaxation capacity combined with temperature drops during cold winter days can lead to low-temperature cracking in flexible pavements.

Multiscale model for asphalt

In order to meet the mentioned requirements at the different temperature regimes, asphalt layers may be optimized by adapting the mix design (e.g., binder/aggregate-ratio), by using different constituents (e.g., different bitumen or filler type), and by the allowance of additives (e.g., polymers to modify bitumen). The development of a prediction tool for the mechanical properties of the so-obtained large variety of asphalt mixtures is a challenging task and is the goal of the research work within the Christian Doppler (CD) Laboratory for "Performance-Based Optimization of Flexible Pavements", installed in 2002 at Vienna University of Technology. For this purpose, a multiscale model for asphalt is currently developed (Lackner et al. 2004) (see Figure 2), providing access to the macroscopic ma-
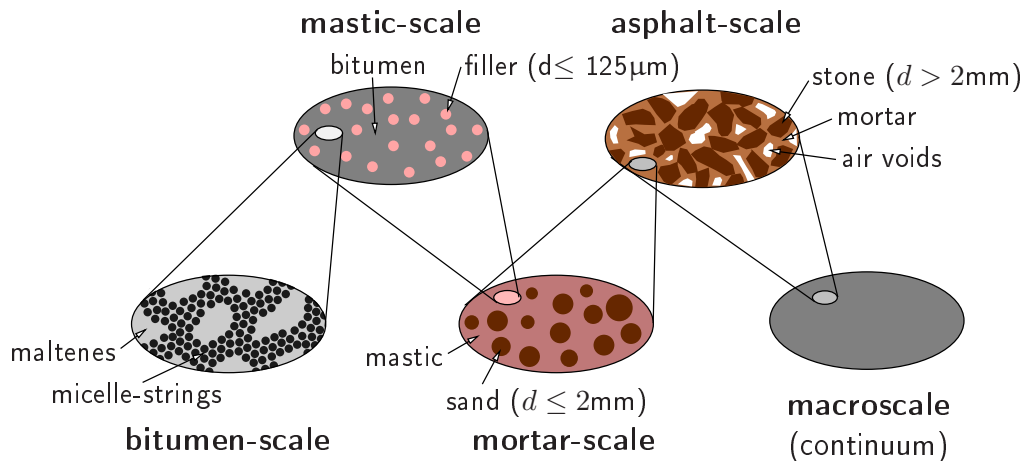
Figure 2: Multiscale model for determination of macroscopic material behavior of asphalt

terial behavior of asphalt via upscaling of information from finer scales of observation towards the macroscale. Hereby, four additional observation scales are introduced below the macroscale:

1. The *bitumen*-scale accounts for the heterogeneous nature of bitumen, consisting of different hydrocarbons with a large variety of molecular weight and polarity (Shell-Bitumen-U.K. 1990). The complex chemical composition results in a string-like microstructure embedded in a matrix substance (Rozeveld et al. 1997; Stangl et al. 2006).

2. At the *mastic*-scale, bitumen and filler (aggregates with $\varnothing \leq 125$ μm) are building up a matrix-inclusion microstructure.

3. In addition to the homogenized mastic, aggregates with 125 μm $\leq \varnothing \leq 2$ mm are taken into account at the *mortar*-scale.

4. The mixture of mortar with aggregates characterized by $\varnothing \geq 2$ mm, where the maximum diameter may range from 8 to 32 mm, is considered at the *asphalt*-scale. In contrast to the *mortar*-scale, air voids are introduced at this scale.

At each scale of observation, the characteristics (such as material morphology and material properties) of the constituents present at this scale are obtained either from the next-finer scale via upscaling or are specified by respective **identification experiments** (see Figure 3). The shift of information from the finer scales of observation towards the *macro*scale requires appropriate homogenization methods. Upscaling of rheological properties of bitumen-aggregate composites is performed in the framework of continuum micromechanics formulating the Mori-Tanaka scheme (Mori and Tanaka 1973) in the Laplace-Carson space (Aigner and Lackner 2007; Aigner et al. 2007). Upscaling of strength properties, on the other hand, is performed using numerical limit analysis formulations (Makrodimopoulos and Martin 2006; Krabbenhoft et al. 2005), giving lower and upper bounds for the effective strength of asphalt (Füssl et al. 2008).

The results from homogenization are assessed by **validation experiments**. For this purpose, novel testing equipment was installed and testing procedures were developed at the CD-Laboratory focusing on the low- and high-temperature behavior of asphalt (Spiegl 2007; Kappl 2007). In fact, the performance of each homogenization step within the multiscale model is assessed by the respective validation experiments.

Based on the properties of the constituents, e.g., bitumen strings and matrix at the *bitumen*-scale, and the knowledge of the composition and microstructure, the macroscopic material properties of asphalt can be determined by the multiscale model shown in Figure 2. Moreover, changes in composition and microstructure of asphalt resulting from e.g. chemical processes (oxidation of bitumen) can be considered at the respective observation scale, and their effects on macroscopic material properties can be evaluated.

Outline of the thesis

This thesis focuses on the identification of material parameters at the lowest scale of observation of the aforementioned multiscale model, i.e., the *bitumen*-scale. For this purpose, the nanoindentation (NI) technique is employed. Since the 1990-ties, nanoindentation is used for the identification of elastic material parameters and the so-called hardness, at the nano- and micrometer range from materials exhibiting elastic and plastic material response (Oliver and Pharr 1992). More recently, NI was also employed for characterization of materials showing mainly time-dependent response (with negligible plastic deformations). Hereby, the viscoelastic properties are determined from back calculation of parameters from the increase of penetration during the so-called holding phase of the NI test (constant load) (see, e.g., (Cheng et al. 2000, 2005; Sakai 2002; Vandamme and Ulm 2006)). Besides (static) nanoindentation creep tests, also cyclic nanoindentation was
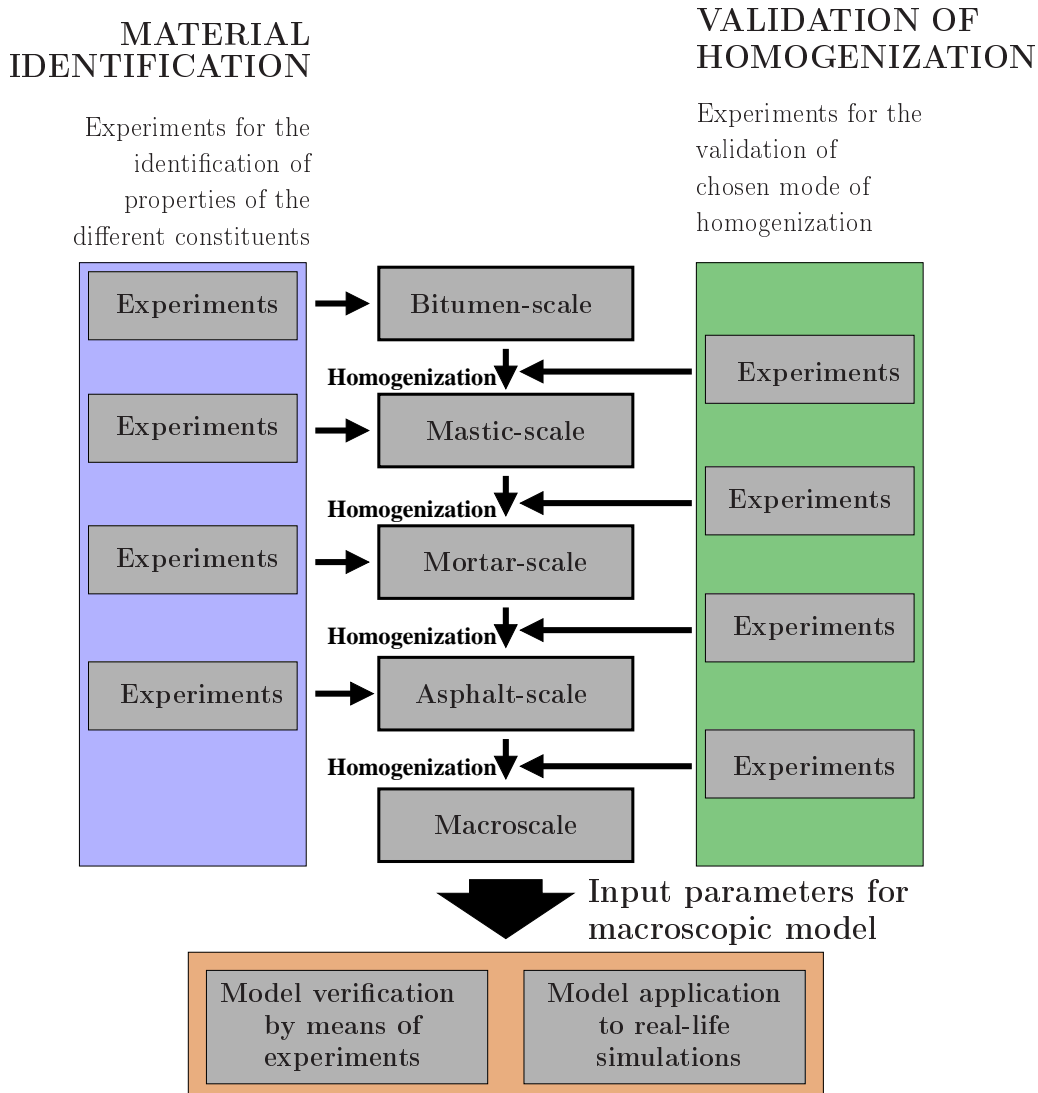
Figure 3: Experiments required for the development of a bottom-up multiscale model for asphalt

proposed for the characterization of materials showing time-dependent material behavior (Oliver and Pharr 1992; Pethica and Oliver 1987; Loubet et al. 1995; Syed Asif et al. 1999, 2001).

A proper identification of material properties at finer scales is of great importance for the success and acceptance of the aforementioned multiscale model. In this context, the impact of the shape of the indenter tip on the identified model parameters is investigated in **Publication A**. Hereby, existing analytical solutions for the penetration of a rigid tip into a viscoelastic halfspace, provided for exact tip geometries (perfect cone or perfect sphere), are extended towards tip geometries, generally accessible through the calibration of the NI-testing equipment. Using the so-obtained solutions, a parameter-identification scheme is proposed, allowing identification of model parameters for three selected vis-

coelastic models via back-calculation from the measured load-penetration curve. The presented approach is illustrated by the identification of short-term viscoelastic properties of bitumen.

However, the parameter identification scheme presented in Publication A is only applicable to materials showing mainly viscoelastic material response. In the most general case, the penetrated material exhibits in addition to viscoelastic also plastic deformation. In **Publication B**, the effect of plastic deformation on the identification of viscoelastic material parameters is investigated. Starting from existing analytical solutions for a rigid tip penetrating a viscoelastic material (see Publication A), two methods for the consideration of plastic deformation are presented. As regards the so-called double indentation technique, the effect of plastic deformation is determined by adapting the load history considering two load cycles per indent. Hereby, plastic deformation is induced in the first load cycle, whereas the second load cycle, which is assumed to cause only viscoelastic deformation, is employed for back-calculation of viscoelastic parameters. In the second method, spherical indenter geometries are employed instead of commonly used pyramidal indenters in order to avoid plastic deformation by reducing the stresses under the indenter during the indentation process. Both methods as well as the standard (single) indentation method are applied to three different polymers giving access to the model parameters for the fractional dash-pot used to describe the viscoelastic behavior. The so-obtained creep-compliance functions are compared with the respective macroscopic creep-compliance functions obtained from bending-beam rheometer tests.

Whereas the parameter identification in Publications A and B is based on (static) nanoindentation creep tests, **Publication C** deals with the identification of viscoelastic properties from cyclic nanoindentation tests. Hereby, an oscillating load is applied to the tip and the amplitude of the penetration history and phase shift between the peak values for the penetration and the prescribed load history are measured. With these two parameters, the complex modulus and the phase angle of the material sample can be determined. In several studies, dealing with the characterization of polymers by means of cyclic nanoindentation, the viscoelastic behavior of the polymers was, if at all, described by a Kelvin–Voigt model. In Publication C, a tool for identification of parameters for various linear viscoelastic models, representing the time-dependent behavior of the material sample, is presented. The proposed technique for parameter identification is illustrated for low-density polyethylene. In order to assess the performance of the presented method, the obtained model parameters are compared with results from (static) nanoindentation creep tests and bending-beam-rheometer tests.

Finally, the thermo-rheological behavior of bitumen and its material phases is studied in **Publication D** by means of the nanoindentation technique. Hereby, the parameter-identification scheme presented in Publication A is extended towards consideration of fractional-creep models. This type of model is found to describe the short- as well as the long-term viscoelastic behavior of bitumen (Lackner et al. 2005). Based on the identified

model parameters, the influence of loading rate, maximum load, and temperature on these parameters is investigated for five selected types of bitumen. Furthermore, the bitumen microstructure and the mechanical behavior of the different bitumen phases is studied by application of the so-called grid indentation technique and compared with results from environmental scanning electron microscopy.

Publication A

Identification of viscoelastic properties by means of nanoindentation taking the real tip geometry into account (Jäger et al. 2007a)

Authored by Andreas Jäger, Roman Lackner, and Josef Eberhardsteiner
Published in *Meccanica*, Volume 42, pages 293–306

Motivated by recent progress in viscoelastic indentation analysis, the identification of viscoelastic properties from nanoindentation test data taking the real tip geometry into account is presented in this paper. Based on the elastic solution of the indentation problem, the corresponding viscoelastic solution is obtained by the application of the method of functional equations. This general solution, which accounts for the real geometric properties of the indenter tip, is specialized for the case of a trapezoidal load history, commonly employed in nanoindentation testing. Three deviatoric creep models, the single dash-pot, the Maxwell, and the three-parameter model are considered. The so-obtained expressions allow us to determine viscoelastic model parameters via back calculation from the measured load-penetration history. The presented approach is illustrated by the identification of short-term viscoelastic properties of bitumen. Hereby, the influence of loading rate, maximum load, and temperature on the model parameters is investigated.

A.1   Introduction

The main goal of nanoindentation (NI) is the identification of mechanical properties of the indented material. During NI measurements, a tip with defined shape penetrates the specimen surface with the indentation load P [N] and the penetration h [m] recorded as a function of time. Commonly, each indent consists of a loading, holding, and unloading phase (see Figure A.1). The hardness of the material, defined as $H = P_{\max}/A_{\mathrm{c}}$ [Pa], is ob-
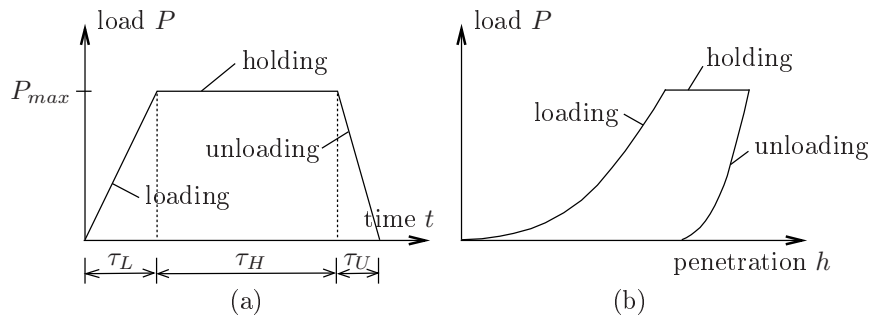

Figure A.1: Illustration of (a) load history and (b) load-penetration curve of NI tests

tained from the loading phase of the NI test. Hereby, A_{c} [m^2] is the horizontal projection of the contact area and $P_{\max}$ [N] denotes the applied maximum load. According to Sneddon (1965) and Oliver and Pharr (1992), Young's modulus E of materials exhibiting elastic or elastoplastic behavior is obtained from the relation between the measured initial slope of the unloading curve $S = dP/dh|_{h=h_{\max}}$ and the indentation modulus $M = E/(1 - \nu^2)$, reading

$$S = \frac{2}{\sqrt{\pi}} M \sqrt{A_{\mathrm{c}}} \ , \tag{A.1}$$

where ν is the Poisson's ratio.

Parameter identification of materials exhibiting, in addition to elastic and plastic material response, time-dependent behavior (e.g., polymers, bitumen, etc.) requires back calculation of the parameters from the holding phase of the measured penetration history $h(t)$. Recently, analytical solutions for the indentation of axisymmetric, rigid tips into a viscoelastic halfspace were reported in Cheng et al. (2005) for spherical tips and in Vandamme and Ulm (2006) for perfect conical tips.

Whereas both Cheng et al. (2005) and Vandamme and Ulm (2006) considered indenter tips characterized by exact geometric properties, the shape of real indenter tips varies in consequence of the production process and in the course of testing due to attrition. By means of calibration, NI-testing equipment give access to the real tip geometry (Oliver and Pharr 1992). In order to consider the so-obtained geometrical properties of the tip for back-calculation of material parameters, analytical solutions for the indentation of a tip into a viscoelastic material, taking the real tip geometry into account, are presented

in this paper. For this purpose, the geometrical representation of the indenter tip (with $A_{\text{tip}} = C_0 f(\rho)^2$ for perfect conical tips) is extended to

$$A_{\text{tip}}(\rho) = \rho^2 \pi = C_0 f(\rho)^2 + C_1 f(\rho) \ , \qquad (A.2)$$

where A_{tip} [m^2] is the area of the cross section and ρ [m] and $f(\rho)$ [m] are the corresponding radius and distance from the apex of the axisymmetric tip, respectively (see Figure A.2). C_0 [-] and C_1 [m] are constants describing the tip shape, which are generally provided during calibration of the NI-testing equipment. In a first step, we will solve the elastic indentation problem for the indenter shape given in Equation (A.2). According to Lee and Radok (1960), the viscoelastic solution is obtained by replacing the operators of the elastic solution by the Laplace transforms of the associated viscoelastic operators. Back transformation gives access to the solution for viscoelastic indentation in the time domain. Finally, the viscoelastic solutions are employed for the identification of viscoelastic properties of bitumen from NI-test data.

A.2 Elastic indentation problem

For the solution of the elastic indentation problem, i.e., a rigid indenter penetrating the elastic halfspace, the so-called Sneddon solution (Sneddon 1965) is employed. According to Sneddon (1965), the relation between the penetration h [m] and the corresponding load P [N] is given for an axisymmetric indenter tip of shape $f(\rho)$ (see Figure A.2) by

$$h = a \int_{\rho=0}^{a} \frac{f'(\rho) d\rho}{\sqrt{a^2 - \rho^2}} \qquad P = 2 \frac{E}{1 - \nu^2} \int_{\rho=0}^{a} \frac{\rho^2 f'(\rho) d\rho}{\sqrt{a^2 - \rho^2}} \ . \qquad (A.3)$$

Hereby, a [m] is the radius of the projected contact area A_{c}, ρ [m] is the radius of the axisymmetric tip, $f(\rho)$ [m] is a smooth function describing the tip shape, and $f' = df/d\rho$.

For the case of conical indenters, $f(\rho) = \rho/\tan\alpha$, where α is the semi-apex angle. Accordingly, for the commonly used Berkovich indenter, which may be represented by a cone of $\alpha = 70.32°$, $f(\rho)$ becomes linear in ρ. In general, however, because of inaccuracies during the tip-production process and attrition, the aforementioned linear relation is nonlinear. During calibration of the NI-testing equipment, this nonlinearity is specified, following the procedure outlined in Oliver and Pharr (1992):

1. Perform indents in a material with given elastic properties (e.g., fused quartz) in the depth range of the indentation experiments;

2. Compute the projected contact area $A_{\text{c}} = \pi/4(S/M)^2$, where S [N/m] is the initial unloading slope of the load-penetration curve and M is the indentation modulus, with $M = E/(1 - \nu^2)$, where $E = 72$ GPa and $\nu = 0.17$ for fused quartz;
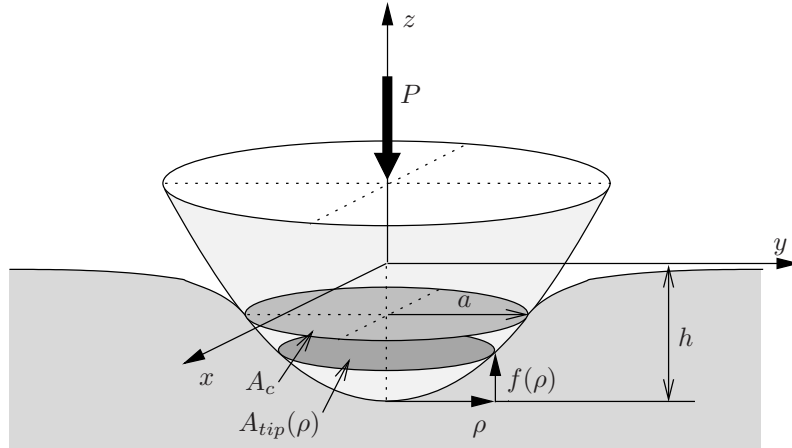
Figure A.2: Contact between a rigid axisymmetric tip of shape $f(\rho)$ and an infinite halfspace (P is the applied load, h is the penetration, a is the contact radius, and A_c is the projected area of contact)

3. Plot A_c as a function of the contact depth h_c, with $h_\mathrm{c} = h - 0.75P/S$, and approximate the so-obtained function by

$$A_\mathrm{c} = C_0 h_\mathrm{c}^2 + C_1 h_\mathrm{c} \ , \tag{A.4}$$

where C_0 [-] and C_1 [m] are constants describing the tip shape.

Replacing A_c and h_c in Equation (A.4) by $\rho^2\pi$ and $f(\rho)$, respectively, $f(\rho)$ is obtained as

$$f(\rho) = \frac{1}{2C_0}\left(\sqrt{C_1^2 + 4C_0\rho^2\pi} - C_1\right) \ . \tag{A.5}$$

For the case of a conical indenter with a semi-apex angle α, where $C_0 = \pi\tan^2\alpha$ and $C_1 = 0$, Equation (A.5) gives $f(\rho) = \rho/\tan\alpha$. Figure A.3 shows the tip-shape function $f(\rho)$ and the area function $A_\mathrm{c}(h_\mathrm{c})$ for a perfect Berkovich tip ($C_0 = 24.5$ and $C_1 = 0$) and a real Berkovich tip with a value of C_1 deviating from zero.

Inserting Equation (A.5) into Equations (A.3) gives the penetration and the applied load as a function of the contact radius a,

$$h = a\sqrt{\frac{\pi}{C_0}}\arctan\frac{2a\sqrt{C_0\pi}}{C_1} \tag{A.6}$$

$$P = 4\pi\frac{E}{1-\nu^2}\frac{2a^3}{3C_1}\ {}_2F_1\left(1/2; 2; 5/2; -\frac{4a^2C_0\pi}{C_1^2}\right) \ , \tag{A.7}$$

where ${}_2F_1(a; b; c; z)$ denotes a hypergeometric function, defined by (see, e.g., Abramowitz and Stegun (1972))

$$ {}_2F_1(a; b; c; z) = \frac{\Gamma(c)}{\Gamma(b)\Gamma(c-b)}\int_0^1 \frac{t^{b-1}(1-t)^{c-b-1}}{(1-tz)^a}dt \ , \tag{A.8}$$

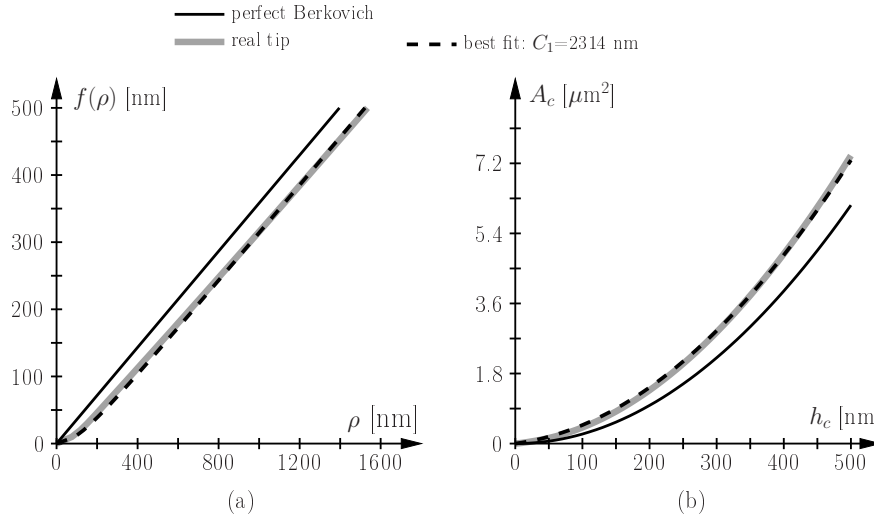which is only valid for $\mathrm{Re}(c) > \mathrm{Re}(b) > 0$.

Figure A.3: (a) Tip-shape function $f(\rho)$ and (b) area function $A_c(h_c)$ of a perfect Berkovich tip ($C_0 = 24.5$ and $C_1 = 0$), and a real Berkovich tip with $C_0 = 24.5$ and $C_1 = 2314$ nm

A.3   Viscoelastic indentation problem − Application to trapezoidal load history

In the following, the elastic indentation problem outlined in the previous section is extended to linear viscoelasticity. For this purpose, the following two methods may be employed:

1. *Laplace transform method:* The Laplace transform method consists in removing the time variable in the viscoelastic problem by employing the Laplace transformation to the time-dependent equations (Lee 1955). From the solution of the so-obtained associated elastic problem, the time-dependent solution is obtained by application of the inverse Laplace transformation. However, this method is restricted to problems, where the interface between deformation and stress boundaries does not change with time, which is not the case for indentation problems.

2. *Method of functional equations:* In the case of the considered indentation problems, the method of functional equations, developed by Lee and Radok (1960), consists in replacing the elastic constants in the solution of the equivalent elastic boundary value problem by the Laplace transforms of the associated viscoelastic operators. This method is not restricted to fixed boundary conditions and remains valid as long as the contact area increases monotonically with time (Lee and Radok 1960).

Due to the restrictions of the Laplace transform method, the method of functional equations (see also Vandamme and Ulm (2006) and Cheng et al. (2005)) is employed to determine the viscoelastic solution for tip shapes described by Equation (A.2). Hereby,

the result for the solution of the indentation in an elastic halfspace (Equation (A.7)) is rewritten in the form

$$P = MF(a) . \tag{A.9}$$

Thus, the solution is split into the material dependent indentation modulus M, with $M = E/(1 - \nu^2)$, and the function $F(a)$ depending only on geometric properties, such as the tip shape (represented by the constant parameters C_0 and C_1) and the unknown contact radius a, reading

$$F(a) = 4\pi \frac{2a^3}{3C_1} \, _2F_1\left(1/2; 2; 5/2; -\frac{4a^2 C_0 \pi}{C_1^2}\right) . \tag{A.10}$$

Following the method of functional equations, the viscoelastic solution for the indentation problem is obtained by replacing the elastic operators P, M, and $F(a)$ in Equation (A.9) by their Laplace transforms $\widehat{P(s)}$, $\widehat{M(s)}$, and $\widehat{F(a(s))}$, giving

$$\widehat{P(s)} = \widehat{M(s)}\widehat{F(a(s))} . \tag{A.11}$$

Re-arrangement yields an expression for the Laplace transform of the function $F(a(s))$ as

$$\widehat{F(a(s))} = \frac{\widehat{P(s)}}{\widehat{M(s)}} = \frac{1}{s\widehat{M(s)}} s\widehat{P(s)} = \widehat{\bar{Y}(s)} s\widehat{P(s)} , \tag{A.12}$$

where $1/(s\widehat{M(s)})$ was replaced by the Laplace transform of $\bar{Y}(t)$, in the following referred to as indentation compliance function. Considering that (i) a multiplication by s in the Laplace domain is equivalent to a derivation in the time domain and (ii) a multiplication of two Laplace-transformed functions is equivalent to the convolution product of the two functions in the time domain, $F(a(t))$ is obtained from Equation (A.12) as

$$F(a(t)) = \int_0^t \bar{Y}(t - \tau)\frac{d}{d\tau}P(\tau)d\tau . \tag{A.13}$$

Finally, combining Equations (A.10) and (A.13) allows determination of the unknown contact radius $a(t)$. With $a(t)$ at hand, Equation (A.6) provides access to the history of the penetration, $h(t)$.

The method of functional equations is restricted to increasing contact areas, and may be applied only to monotonically increasing and constant load histories (Lee and Radok 1960). Since indentation tests are commonly conducted under load control, Equation (A.13) is specified to the trapezoidal load history depicted in Figure A.1(a), reading

$$P(t) = \begin{cases} P_L(t) = t/\tau_L P_{max} & \text{for} \quad 0 \le t \le \tau_L \\ P_H(t) = P_{max} & \text{for} \quad \tau_L \le t \le \tau_L + \tau_H \\ P_U(t) = \dfrac{\tau_L + \tau_H + \tau_U - t}{\tau_U} P_{max} & \text{for} \quad \tau_L + \tau_H \le t \\ & \qquad \le \tau_L + \tau_H + \tau_U \end{cases} , \tag{A.14}$$

where τ_{L}, τ_{H}, and τ_{U} are the loading, holding, and unloading durations, respectively. Considering the load history $P(t)$ given in Equation (A.14) in Equation (A.13), the function $F(a(t))$ becomes for the loading and holding regime

$$F_{\mathrm{L}}(a(t)) = \int_0^t \bar{Y}(t-\tau)\frac{d}{d\tau}P_{\mathrm{L}}(\tau)d\tau = \frac{P_{\max}}{\tau_{\mathrm{L}}}\int_0^t \bar{Y}(t-\tau)d\tau \qquad (\mathrm{A.15})$$

$$F_{\mathrm{H}}(a(t)) = \int_0^{\tau_{\mathrm{L}}} \bar{Y}(t-\tau)\frac{d}{d\tau}P_{\mathrm{L}}(\tau)d\tau + \int_{\tau_{\mathrm{L}}}^t \bar{Y}(t-\tau)\frac{d}{d\tau}P_{\mathrm{H}}(\tau)d\tau$$

$$= \frac{P_{\max}}{\tau_{\mathrm{L}}}\int_0^{\tau_{\mathrm{L}}} \bar{Y}(t-\tau)d\tau \; . \qquad (\mathrm{A.16})$$

Based on F_{L} and F_{H} in Equations (A.15) and (A.16), the history of the penetration, $h(t)$, for the loading and holding time is determined in three steps:

1. The indentation compliance function $\bar{Y}(t)$ appearing in Equations (A.15) and (A.16) is determined for the considered viscoelastic model;

2. $F_{\mathrm{L}}(a(t))$ and $F_{\mathrm{H}}(a(t))$ are computed using Equations (A.15) and (A.16); and

3. The contact radius $a(t)$ and, hence, via Equation (A.6), the penetration $h(t)$ are determined by combining the expressions for $F_{\mathrm{L}}(a(t))$ and $F_{\mathrm{H}}(a(t))$ with Equation (A.10).

In the following subsections, these three steps are described in more detail.

A.3.1   Determination of the indentation compliance function $\bar{Y}(t)$

The indentation compliance function $\bar{Y}(t)$ is determined for three deviatoric creep models, i.e., (i) the single dash-pot (DP), (ii) the Maxwell (MX) model, and (iii) the three-parameter (3P) model (see Figure A.4). In the case of elastic material response, the
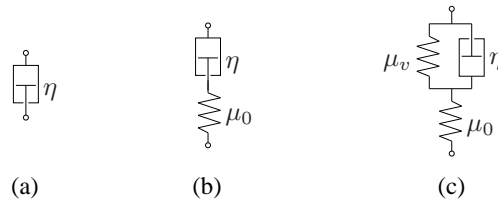

Figure A.4: Viscoelastic deviatoric creep models considered in this study: (a) the single dash-pot (DP), (b) the Maxwell (MX) model, and (c) the three-parameter (3P) model

indentation modulus M can be expressed by the bulk modulus k and the shear modulus

μ_0, reading

$$M = \frac{E}{1 - \nu^2} = \frac{\frac{9k\mu_0}{3k+\mu_0}}{1 - \left(\frac{3k-2\mu_0}{6k+2\mu_0}\right)^2} = 4\mu_0 \frac{3k + \mu_0}{3k + 4\mu_0} \ . \tag{A.17}$$

By the way of application of the method of functional equations, the elastic constants k and μ_0 in Equation (A.17) are replaced by the associated Laplace-transformed operators $\widehat{k(s)}$ and $\widehat{\mu(s)}$, reading

$$\widehat{M(s)} = 4\widehat{\mu(s)} \frac{3\widehat{k(s)} + \widehat{\mu(s)}}{3\widehat{k(s)} + 4\widehat{\mu(s)}} \ , \tag{A.18}$$

where $\widehat{k(s)} = k$ for the case of deviatoric creep only. The shear relaxation modulus, on the other hand, is time dependent, and is given by (see, e.g., Findley et al. (1989)):

$$\widehat{\mu_{\mathrm{DP}}(s)} = (s\mathcal{L}\{J_{\mathrm{DP}}\})^{-1} = (s\mathcal{L}\{t/\eta\})^{-1} = s\eta \ , \tag{A.19}$$

$$\widehat{\mu_{\mathrm{MX}}(s)} = (s\mathcal{L}\{J_{\mathrm{MX}}\})^{-1} = (s\mathcal{L}\{1/\mu_0 + t/\eta\})^{-1} = \left(\frac{1}{\mu_0} + \frac{1}{s\eta}\right)^{-1} \ , \tag{A.20}$$

$$\begin{aligned}\widehat{\mu_{\mathrm{3P}}(s)} &= (s\mathcal{L}\{J_{\mathrm{3P}}\})^{-1} = \left(s\mathcal{L}\left\{\frac{1}{\mu_0} + \frac{1}{\mu_{\mathrm{v}}}\left[1 - \exp\left(-\frac{\mu_{\mathrm{v}}}{\eta}t\right)\right]\right\}\right)^{-1} \\ &= \left(\frac{1}{\mu_0} + \frac{1}{\mu_{\mathrm{v}} + s\eta}\right)^{-1} \ , \end{aligned} \tag{A.21}$$

where $\mathcal{L}\{\bullet(t)\}$ denotes the Laplace transformation of $\bullet(t)$. Considering $\widehat{\mu(s)}$ of the different viscoelastic models given in Equations (A.19) to (A.21) in Equation (A.18) and applying the inverse Laplace transformation to $\bar{Y}(s) = 1/(s\widehat{M(s)})$, $\bar{Y}(t)$ is obtained as

$$\bar{Y}_{\mathrm{DP}}(t) = \frac{1}{4}\left\{\frac{t}{\eta} + \frac{1}{k}\left[1 - \exp\left(-\frac{3k}{\eta}t\right)\right]\right\} \ , \tag{A.22}$$

$$\bar{Y}_{\mathrm{MX}}(t) = \frac{1}{4}\left\{\frac{1}{\mu_0} + \frac{t}{\eta} + \frac{1}{k}\left[1 - \frac{\mu_0}{\mu_0 + 3k}\exp\left(-\frac{3k\mu_0}{\eta(\mu_0 + 3k)}t\right)\right]\right\} \ , \tag{A.23}$$

$$\begin{aligned}\bar{Y}_{\mathrm{3P}}(t) = {} & \frac{1}{4}\left\{\frac{1}{\mu_0} + \frac{1}{\mu_{\mathrm{v}}}\left[1 - \exp\left(-\frac{\mu_{\mathrm{v}}}{\eta}t\right)\right] + \frac{3(\mu_0 + \mu_{\mathrm{v}})}{\mu_0\mu_{\mathrm{v}} + 3k(\mu_0 + \mu_{\mathrm{v}})}\right. \\ & \left.\left[1 - \frac{\mu_0^2}{(\mu_0 + 3k)(\mu_0 + \mu_{\mathrm{v}})}\exp\left(-\frac{\mu_0\mu_{\mathrm{v}} + 3k(\mu_0 + \mu_{\mathrm{v}})}{\eta(\mu_0 + 3k)}t\right)\right]\right\} \ . \end{aligned} \tag{A.24}$$

In the case of incompressible materials, where $k = \infty$, Equations (A.22) to (A.24) simplify to:

$$\bar{Y}_{\mathrm{DP}}(t) = \frac{1}{4}\frac{t}{\eta} \,, \tag{A.25}$$

$$\bar{Y}_{\mathrm{MX}}(t) = \frac{1}{4}\left(\frac{1}{\mu_0} + \frac{t}{\eta}\right) \,, \tag{A.26}$$

$$\bar{Y}_{\mathrm{3P}}(t) = \frac{1}{4}\left\{\frac{1}{\mu_0} + \frac{1}{\mu_{\mathrm{v}}}\left[1 - \exp\left(-\frac{\mu_{\mathrm{v}}}{\eta}t\right)\right]\right\} \,. \tag{A.27}$$

A.3.2   Determination of $F(a(t))$

Considering the indentation compliance functions $\bar{Y}(t)$ for the three viscoelastic models given in Equations (A.22) to (A.24) in Equations (A.15) and (A.16), the function $F(a(t))$ is obtained for the loading and holding regime, $F_{\mathrm{L}}(a(t))$ and $F_{\mathrm{H}}(a(t))$, for the three considered viscoelastic models as

$$
\begin{aligned}
F_{\mathrm{L\text{-}DP}}(a(t)) &= \frac{P_{\max}}{\tau_{\mathrm{L}}}\int_0^t \bar{Y}(t-\tau)d\tau \\
&= \frac{P_{\max}}{4\tau_{\mathrm{L}}}\left\{\frac{1}{k}t + \frac{1}{2\eta}t^2 - \frac{\eta}{3k^2}\left(1 - \exp\left(-\frac{3k}{\eta}t\right)\right)\right\} \,, \tag{A.28}
\end{aligned}
$$

$$
\begin{aligned}
F_{\mathrm{H\text{-}DP}}(a(t)) &= \frac{P_{\max}}{\tau_{\mathrm{L}}}\int_0^{\tau_{\mathrm{L}}} \bar{Y}(t-\tau)d\tau \\
&= \frac{P_{\max}}{4\tau_{\mathrm{L}}}\left\{\frac{\tau_{\mathrm{L}}}{k} + \frac{1}{2\eta}(2t-\tau_{\mathrm{L}})\tau_{\mathrm{L}}\right. \\
&\quad \left. + \frac{\eta}{3k^2}\left(\exp\left(-\frac{3k}{\eta}t\right)\left[1 - \exp\left(\frac{3k}{\eta}\tau_{\mathrm{L}}\right)\right]\right)\right\} \,, \tag{A.29}
\end{aligned}
$$

$$
\begin{aligned}
F_{\mathrm{L\text{-}MX}}(a(t)) &= \frac{P_{\max}}{4\tau_{\mathrm{L}}}\left\{\frac{\mu_0+k}{\mu_0 k}t + \frac{1}{2\eta}t^2\right. \\
&\quad \left. - \frac{\eta}{3k^2}\left(1 - \exp\left(-\frac{3\mu_0 k}{\eta(\mu_0+3k)}t\right)\right)\right\} \,, \tag{A.30}
\end{aligned}
$$

$$
\begin{aligned}
F_{\mathrm{H\text{-}MX}}(a(t)) &= \frac{P_{\max}}{4\tau_{\mathrm{L}}}\left\{\frac{\mu_0+k}{\mu_0 k}\tau_{\mathrm{L}} + \frac{1}{2\eta}(2t-\tau_{\mathrm{L}})\tau_{\mathrm{L}} + \frac{\eta}{3k^2}\left(\exp\left(-\frac{3\mu_0 k}{\eta(\mu_0+3k)}t\right)\right.\right. \\
&\quad \left.\left. \left[1 - \exp\left(\frac{3\mu_0 k}{\eta(\mu_0+3k)}\tau_{\mathrm{L}}\right)\right]\right)\right\} \,, \tag{A.31}
\end{aligned}
$$

$$
\begin{aligned}
F_{\text{L-3P}}(a(t)) &= \frac{P_{\max}}{4\tau_{\text{L}}} \Bigg\{ \frac{3\mu_0^2 \eta}{(\mu_0\mu_{\text{v}} + 3k(\mu_0 + \mu_{\text{v}}))^2} \\
&\quad \left(-1 + \exp\left(-\frac{\mu_0\mu_{\text{v}} + 3k(\mu_0 + \mu_{\text{v}})}{\eta(\mu_0 + 3k)} t \right) \right) \\
&\quad + \frac{(\mu_0 + \mu_{\text{v}})(4\mu_0\mu_{\text{v}} + 3k(\mu_0 + \mu_{\text{v}}))}{\mu_0\mu_{\text{v}}(\mu_0\mu_{\text{v}} + 3k(\mu_0 + \mu_{\text{v}}))} t \\
&\quad + \frac{\eta}{\mu_{\text{v}}^2} \left(-1 + \exp\left(-\frac{\mu_{\text{v}}}{\eta} t \right) \right) \Bigg\} \,, \quad\quad\quad\quad \text{(A.32)}
\end{aligned}
$$

$$
\begin{aligned}
F_{\text{H-3P}}(a(t)) &= \frac{P_{\max}}{4\tau_{\text{L}}} \Bigg\{ \left(\frac{1}{\mu_0} + \frac{1}{\mu_{\text{v}}} + \frac{3(\mu_0 + \mu_{\text{v}})}{\mu_0\mu_{\text{v}} + 3k(\mu_0 + \mu_{\text{v}})} \right) \tau_{\text{L}} \\
&\quad - \frac{\eta}{\mu_{\text{v}}^2} \left(\exp\left(-\frac{\mu_{\text{v}}}{\eta} t \right) \left[-1 + \exp\left(\frac{\mu_{\text{v}}}{\eta} \tau_{\text{L}} \right) \right] \right) \\
&\quad - \frac{3\eta\mu_0^2}{(\mu_0\mu_{\text{v}} + 3k(\mu_0 + \mu_{\text{v}}))^2} \left(\exp\left(-\frac{\mu_0\mu_v + 3k(\mu_0 + \mu_{\text{v}})}{\eta(\mu_0 + 3k)} t \right) \right. \\
&\quad \left. \left[-1 + \exp\left(\frac{\mu_0\mu_{\text{v}} + 3k(\mu_0 + \mu_{\text{v}})}{\eta(\mu_0 + 3k)} \tau_{\text{L}} \right) \right] \right) \Bigg\} \,. \quad \text{(A.33)}
\end{aligned}
$$

A.3.3   Determination of $a(t)$ and $h(t)$

The history of the contact radius, $a(t)$, is obtained from combining the expressions for $F_{\text{L}}(a(t))$ and $F_{\text{H}}(a(t))$ given in Equations (A.28) to (A.33) with Equation (A.10). The so-obtained (nonlinear) expression for $a(t)$ is solved numerically, employing a Newton-iteration scheme. With $a(t)$ at hand, the history of the penetration, $h(t)$, is given by Equation (A.6) for a given load history $P(t)$ and the material model describing the behavior of the viscoelastic half space.

A.3.4   Illustrative example

The developed mode of determination of the penetration history $h(t)$ provides insight into the influence of the tip shape on NI results, as illustrated for a DP-type material in Figure A.5. According to Figure A.5(a), the largest penetration is obtained for the perfect Berkovich. Any variation of the indenter tip from the perfect Berkovich tip results in a reduction of the penetration. Figure A.5(b) shows the deviation of the penetration depth from the Berkovich response, giving deviations found in the tens of percent.
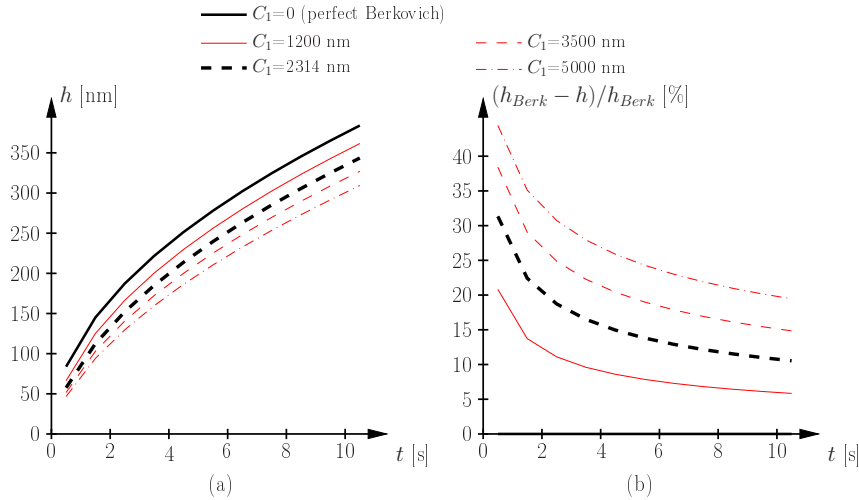
Figure A.5: Indentation of viscoelastic halfspace (DP-model with $\eta = 100$ MPa·s) for different tip shapes: (a) Penetration history of the holding period; (b) deviation of penetration depth from response obtained from perfect Berkovich indenter ($C_0 = 24.5$; load history: $P_{\max} = 10 \ \mu$N, $\tau_{\mathrm{L}} = 0.5$ s, $\tau_{\mathrm{H}} = 10$ s)

A.4 Application – identification of viscoelastic properties of bitumen

A.4.1 Introductory remarks

Bitumen is the binder material of asphalt and determines its complex thermo-rheological behavior which, at high temperatures ($T > 135$ °C), provides the low viscosity of asphalt required for the construction and compaction process of high-quality asphalt layers. During hot summer periods, this viscosity should be significantly higher in order to avoid the development of permanent deformations in asphalt pavements (rutting), requiring costly repair work and reducing the traffic safety. The desirable increase of viscosity from hot to medium temperatures ($0 < T < 70$ °C) is, on the other hand, disadvantageous at low temperatures ($T < 0$ °C), causing low-temperature cracking in asphalt pavements in consequence of thermal-shrinkage strains associated with cooling during changing weather conditions.

In general, the viscosity of bitumen is found to decrease linearly with increasing temperature in the log(viscosity)-temperature diagram (see Figure A.6 (Partal et al. 1999)). The viscosity and its change with increasing temperature is influenced by several factors:

1. The chemical composition and the molecular weight distribution of the crude oil;

2. The so-called cut point, i.e., the temperature during the distillation process (the

higher the cut point, the higher the viscosity), and air blowing after the distillation process (increase of viscosity due to bitumen oxidation); and

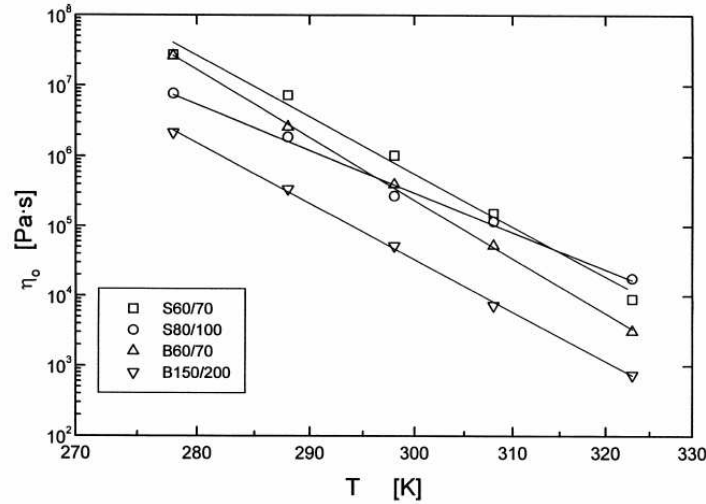3. The allowance of additives (commonly polymers).

Figure A.6: Temperature dependence of the zero-shear-rate limiting viscosity for different types of bitumen (Partal et al. 1999)

In order to gain insight in the origin of the bitumen viscosity, the viscous properties of one chosen type of bitumen (B50/70, see Table A.1) are determined, employing the parameter-identification procedure outlined in the previous section.

Table A.1: Properties of considered type of bitumen (B50/70)

penetration depth [1/10 mm] (ÖNORM EN 1426 2000):	49
breaking point by Fraß [°C] (ÖNORM EN 12593 2000):	-13
softening point [°C] (ÖNORM EN 1427 2000):	50.5

elemental analysis [mass-%]:	
carbon	83.04
hydrogen	10.38
nitrogen	1.11
sulfur	5.05
Σ	99.58

A.4.2   Specimen preparation and test protocol

In addition to the identification of model parameters, the application of the so-called grid indentation technique (Ulm et al. 2005) gives access to the morphology of bitumen in the μm range and allows application of statistical techniques for the interpretation of NI-test results. Hereby, several indents are performed on a specified grid (e.g., 10×10 indents). The distance between two adjacent grid points is adjusted to the characteristic dimension of the bitumen microstructure and the maximum penetration.

The bitumen samples were prepared by heating and pouring into a sample holder. The bitumen surface obtained from pouring (as opposed to low-temperature fracture) exhibits the appropriate smoothness for NI testing. Two studies were performed, focusing on

- The influence of the loading rate and the maximum load on the determined model parameters and

- The temperature dependence of the model parameters.

A.4.3   Presentation of results and discussion

In order to determine model parameters for bitumen from NI data, the analytical solutions for $F_{\mathrm{L}}(a(t))$ and $F_{\mathrm{H}}(a(t))$ (see Equations (A.28) to (A.33)) are specialized for incompressible materials, i.e., for $k = \infty$, giving

$$F_{\text{L-DP}}(a(t)) \;=\; \frac{P_{\max}}{8\tau_{\mathrm{L}}\eta}t^2 \tag{A.34}$$

$$F_{\text{H-DP}}(a(t)) \;=\; \frac{P_{\max}}{8\eta}(2t - \tau_{\mathrm{L}}) \tag{A.35}$$

$$F_{\text{L-MX}}(a(t)) \;=\; \frac{P_{\max}}{4\tau_{\mathrm{L}}}\left\{\frac{1}{\mu_0}t + \frac{1}{2\eta}t^2\right\} \tag{A.36}$$

$$F_{\text{H-MX}}(a(t)) \;=\; \frac{P_{\max}}{4}\left\{\frac{1}{\mu_0} + \frac{1}{2\eta}(2t - \tau_{\mathrm{L}})\right\} \tag{A.37}$$

$$F_{\text{L-3P}}(a(t)) \;=\; \frac{P_{\max}}{4\tau_{\mathrm{L}}}\left\{\left(\frac{1}{\mu_0} + \frac{1}{\mu_{\mathrm{v}}}\right)t + \frac{\eta}{\mu_{\mathrm{v}}^2}\left[-1 + \exp\left(-\frac{\mu_{\mathrm{v}}}{\eta}t\right)\right]\right\} \tag{A.38}$$

$$F_{\text{H-3P}}(a(t)) \;=\; \frac{P_{\max}}{4\tau_{\mathrm{L}}}\left\{\left(\frac{1}{\mu_0} + \frac{1}{\mu_{\mathrm{v}}}\right)\tau_{\mathrm{L}}\right.$$

$$\left. -\frac{\eta}{\mu_{\mathrm{v}}^2}\exp\left(-\frac{\mu_{\mathrm{v}}}{\eta}t\right)\left[-1 + \exp\left(\frac{\mu_{\mathrm{v}}}{\eta}\tau_{\mathrm{L}}\right)\right]\right\}\;. \tag{A.39}$$

Taking into account that the MX and the DP model are special cases of the more general 3P model, giving the MX model for $\mu_{\mathrm{v}} = 0$ and the DP model for $\mu_{\mathrm{v}} = 0$, $\mu_0 = \infty$, the

3P model is employed in the following for the identification of model parameters. Hereby, the error between the experimentally-obtained function $F_{\exp}(a(t))$[1] for the holding period and the analytical result given in Equation (A.39) is minimized by adapting the unknown shear moduli μ_0 and μ_{v}, and the viscosity η (see Figure A.7). The mentioned error is
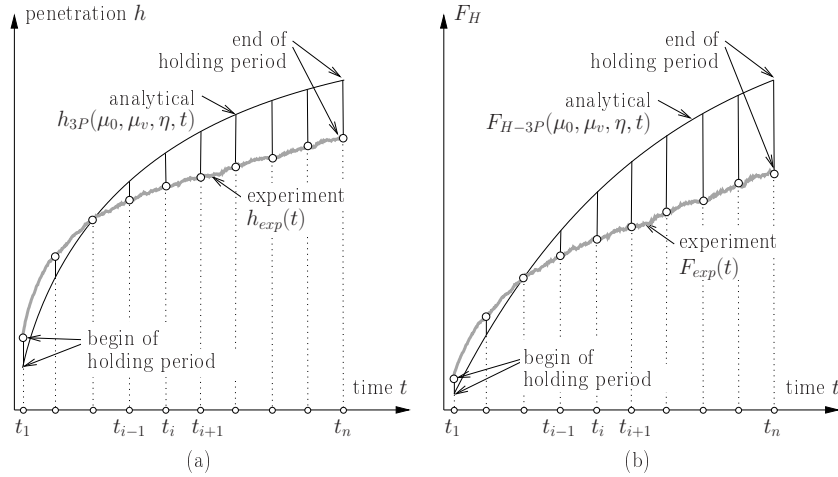

Figure A.7: Illustration of error between model response and NI-test data (holding period): (a) penetration history $h(t)$ and (b) function F_{H}

defined by

$$R_{3\mathrm{P}}(\mu_0, \mu_{\mathrm{v}}, \eta) = \frac{e(\mu_0, \mu_{\mathrm{v}}, \eta)}{u} \ , \tag{A.40}$$

with

$$e^2(\mu_0, \mu_{\mathrm{v}}, \eta) = \sum_{i=1}^{n} [F_{\exp}(t_i) - F_{\mathrm{H}\text{-}3\mathrm{P}}(\mu_0, \mu_{\mathrm{v}}, \eta, t_i)]^2 \text{ and} \tag{A.41}$$

$$u^2 = \sum_{i=1}^{n} F_{\exp}^2(t_i) \ ,$$

where n was set equal to 10. The error given in Equation (A.40) was minimized by adapting μ_0, μ_{v}, and η, using a simplex iteration (Press et al. 1996). With the model parameters at hand, the history of the contact radius, $a_{3\mathrm{P}}(t_i)$, is determined from Equation (A.10) using a Newton-iteration scheme. Subsequently, $h_{3\mathrm{P}}(t_i)$ is computed from Equation (A.6) (see, e.g, Figure A.7(a)). The procedure employed for parameter identification is summarized in Figure A.8.

In order to check the existence of a global minimum of the error $R_{3\mathrm{P}}$, the influence of the model parameters on the error $R_{3\mathrm{P}}$ is studied. Figure A.9 shows contour-plots of

---

[1]$F_{\exp}(a(t))$ is determined from the penetration history using Equations (A.6) and (A.10) and $C_0 = 24.5$; C_1 is adapted to the penetration at the end of the holding period using the NI-equipment calibration data

1. Obtain maximum penetration, $h_{\max}$, from indentation data

2. Compute C_1 for $h_{\max}$ according to Equation (A.4) using a Newton-iteration scheme ($C_0 = 24.5$, $A_{\mathrm{c}}(h_{\mathrm{c}})$ is provided from the NI-equipment calibration)

3. Select n equidistant data points within the holding period for error minimization

4. DO $i=1,n$

   (a) Compute contact radius $a_{\exp}(t_i)$ from Equation (A.6) using a Newton-iteration scheme

   (b) Compute $F_{\exp}(a(t_i))$ from Equation (A.10)

   ENDDO

5. Identify model parameters μ_0, μ_{v}, and η using a simplex iteration (Press et al. 1996)

   (a) Determine start values based on analytical results for perfect conical indentation (Vandamme and Ulm 2006)

   (b) Minimize error $R_{3\mathrm{P}}$ given in Equation (A.40)

The penetration history corresponding to the identified model parameters may be obtained from Equations (A.39), (A.10), and (A.6), giving $F_{\mathrm{H\text{-}3P}}(t)$, $a_{3\mathrm{P}}(t)$, and finally $h_{3\mathrm{P}}(t)$.

Figure A.8: Flowchart for identification of model parameters for *one* indent

the error as a function of the model parameters (one parameter is kept constant for each plot). Whereas the spring in series (μ_0) only slightly changes the error, variation of the parameters of the Kelvin-Voigt unit (η and μ_{v}) significantly affects the error. The distribution of error $R_{3\mathrm{P}}$ shown in Figure A.9 indicates the existence of one global minimum.

The presented parameter-identification scheme was applied to the considered type of bitumen tested at -1 °C. Hereby, 100 indents in a 10×10 grid were performed. Figure A.10 shows the frequency plots for the Young's modulus E_0, with $E_0 = 3\mu_0$ using Poisson's ratio $\nu = 0.5$ for incompressible materials, the shear modulus μ_{v}, the viscosity η, and the error $R_{3\mathrm{P}}$. The computed mean value of the error $R_{3\mathrm{P}}$ does not exceed 4 %, confirming the proper choice of the 3P model for fitting the short-term viscoelastic response of bitumen. The obtained frequency plots are approximated by a Gaussian distribution, giving mean values and standard deviations for the model parameters. For the considered type of bitumen (B50/70) the mean values of the model parameters at $T = -1$ °C are: $E_0 = 3\mu_0 = 2.0$ GPa, $\mu_{\mathrm{v}} = 0.022$ GPa, and $\eta = 0.15$ GPa·s.
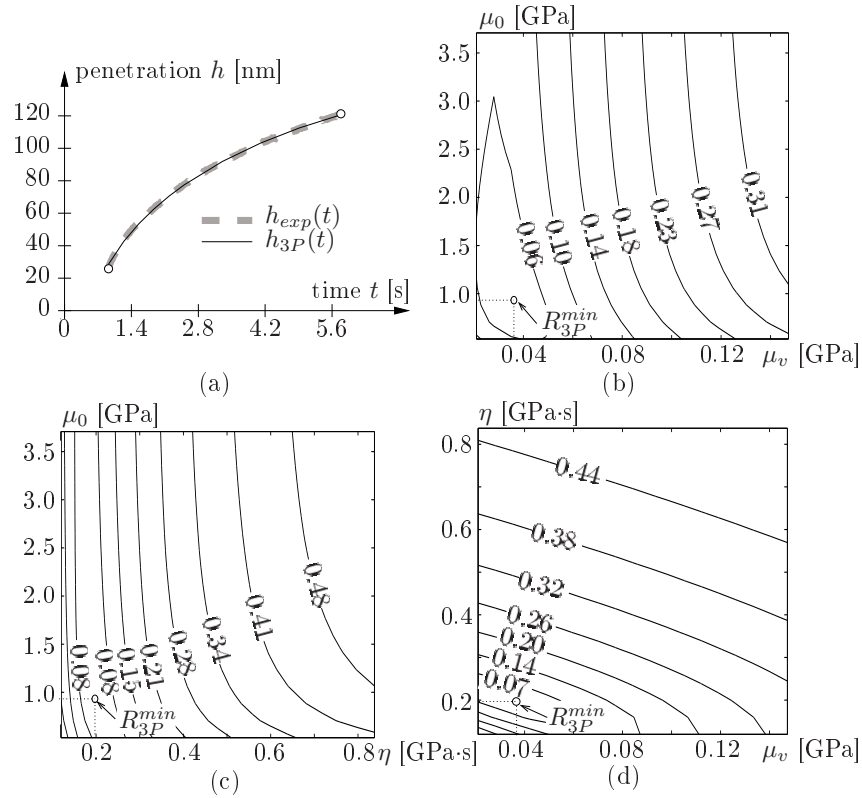
Figure A.9: Influence of model parameters on error $R_{3\mathrm{P}}$: (a) time-penetration curve (NI-test conditions: $T = -1$ °C, $P_{\max} = 10$ μN, $\dot{P} = dP/dt = 40$ μN/s, $\tau_{\mathrm{H}} = 5$ s), and error $R_{3\mathrm{P}}$ within the parameter range $0.120 < \eta < 0.838$, $0.0210 < \mu_{\mathrm{v}} < 0.147$, $0.530 < \mu_0 < 3.71$ keeping (b) $\eta = 0.199$, (c) $\mu_{\mathrm{v}} = 0.0351$, and (d) $\mu_0 = 0.883$ constant
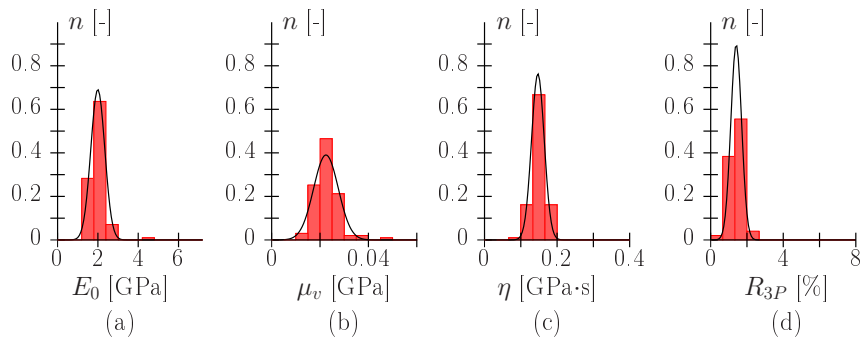

Figure A.10: Identification of model parameters for B50/70 tested at -1 °C: frequency plots of (a) Young's modulus of spring in series $E_0 = 3\mu_0$ [GPa], (b) shear modulus of spring in parallel μ_{v} [GPa], (c) viscosity of the dashpot η [GPa·s], and (d) error $R_{3\mathrm{P}}$ [%] (NI-test conditions: $P_{\max} = 20$ μN, $\dot{P} = dP/dt = 40$ μN/s, $\tau_{\mathrm{H}} = 5$ s)

Figure A.11 shows the mean values of the 3P-model parameters for different loading rates

and different values for the maximum load identified from grid indentations on bitumen B50/70 at -1 °C ($\dot{P} = dP/dt$ =20, 40, 80, 160 μN/s; P_{max} =10, 20, 50, 120, 240 μN). Whereas the influence of the loading rate on the parameters is small for all considered
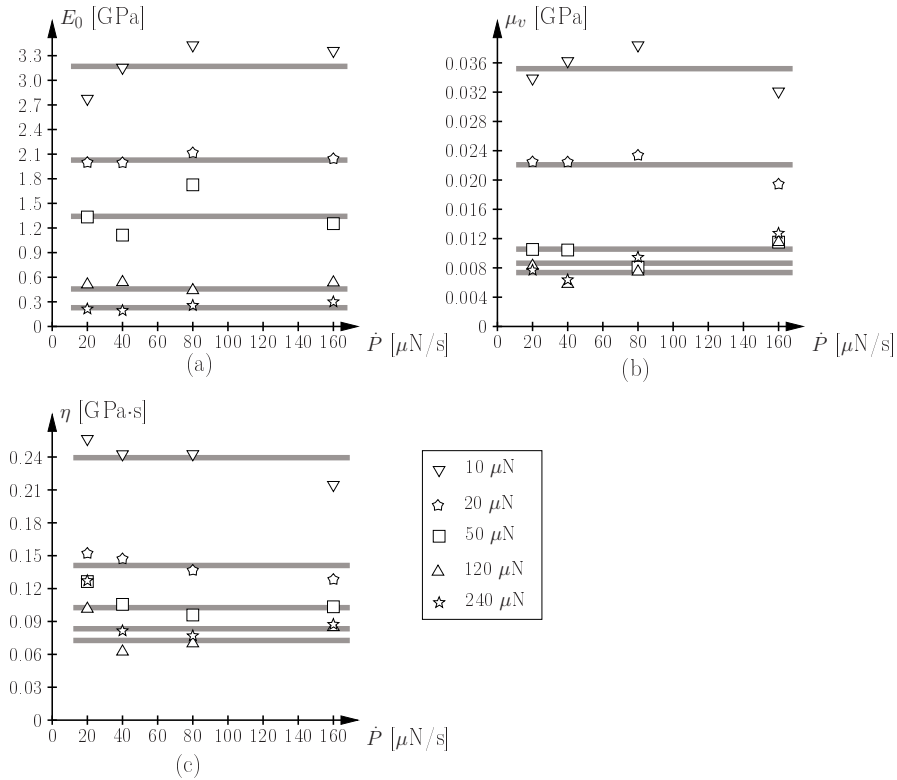

Figure A.11: Influence of loading rate on 3P-model parameters: (a) Young's modulus of spring in series E_0 [GPa], (b) shear modulus of spring in parallel μ_v [GPa], (c) viscosity of the dash-pot η [GPa·s] (bitumen B50/70 tested at T =-1 °C; P_{max} =10, 20, 50, 120, 240 μN; $\dot{P} = dP/dt$ =20, 40, 80, 160 μN/s; τ_H =5 s (for P_{max} = 10, 20 μN) and 10 s (for P_{max} = 50, 120, 240 μN))

load levels, the maximum load itself has a significant impact on the obtained model parameters. By increasing the maximum load, the model parameters decrease until they reach a limiting value. The error R_{3P} (Equation A.40), reflecting the deviation between NI-test data and model response, is always smaller than 4 %. Accordingly, an extension of the employed 3P-model would, of course, further reduce the aforementioned deviation, but would not eliminate the observed load-dependency of the identified model parameters. Thus, the variation of the identified model parameters with the maximum load and, consequently, with the penetration depth is explained by the bitumen microstructure, consisting of high-viscous strings embedded into a low-viscous matrix (Stangl et al. 2006).

Accounting for the thermo-rheological behavior of bitumen, the influence of temperature on the model parameters is studied by conducting NI tests at different temperatures.

Figures A.12(a), (b), and (c) show mean values of the 3P-model parameters for bitumen B50/70 tested at T =-4.5, -1, 2, 5.5, and 9 °C. All three parameters exhibit the same temperature dependence, decreasing from -4.5 to -1 °C, slightly increasing from -1 to 2 °C, and finally decreasing again from 2 to 9 °C. The increase from -1 to 2 °C might be explained by thermo-rheological processes, observed during testing of bitumen by means of modulated differential scanning calorimetry (Jäger 2004).

Additionally, the variation of (i) the relaxation time of the Kelvin-Voigt unit τ_{KV}, with $\tau_{\mathrm{KV}} = \eta/\mu_{\mathrm{v}}$ [s], and (ii) the relaxation/creep time τ_{3P}, with $\tau_{\mathrm{3P}} = \eta/(E_0/3 + \mu_{\mathrm{v}})$ [s], involving all three parameters of the 3P model, with the temperature is depicted in Figures A.12(d) and (e). Whereas τ_{KV} remains approximately constant from -4.5 to 2 °C and increases from 2 to 9 °C, τ_{3P} decreases continuously with increasing temperature. This decrease of τ_{3P} reflects the decreasing elastic behavior of bitumen with increasing temperature.

The temperature dependence of η depicted in Figure A.13 is well-described by an Arrhenius-type law at temperatures above 2 °C, reading:

$$\frac{1}{\eta} = \frac{1}{\bar{\eta}(\bar{T})} \exp\left[-\frac{E_{\mathrm{a}}}{R}\left(\frac{1}{T} - \frac{1}{\bar{T}}\right)\right] , \qquad (A.42)$$

where $\bar{T}$ [K] is the reference temperature, $R = 8.31$ J/MOL/K is the gas constant, and E_{a} [J/MOL] is the activation energy. The ratio of the activation energy and the gas constant, E_{a}/R, for temperatures above 2 °C is obtained as 14600 K. Interestingly, the activation energy computed for the whole tested temperature range (dashed line in Figure A.13), with $E_{\mathrm{a}}/R = 9700$ K, agrees very well with the value obtained from macroscopic bending-beam-rheometer tests of bitumen, revealing a value of E_{a}/R of 9000 K (Lackner et al. 2005).

A.5   Concluding remarks

The identification of viscoelastic properties from nanoindentation-test (NI-test) data taking the real tip geometry into account was presented in this paper. Hereby, the shape of the real tip was approximated by an axisymmetric indenter, with the constants C_0 and C_1 describing the tip shape. Based on the elastic solution of the indentation problem for this indenter shape (Sneddon 1965), the corresponding viscoelastic solution was determined for three deviatoric creep models: (i) the single dash-pot, (ii) the Maxwell, and (iii) the three-parameter model. With the penetration histories for the different viscoelastic models at hand, a parameter-identification procedure for the model parameters was presented.

The application of this procedure was illustrated by determination of the viscoelastic properties of bitumen. For this purpose, NI tests were performed for different loading
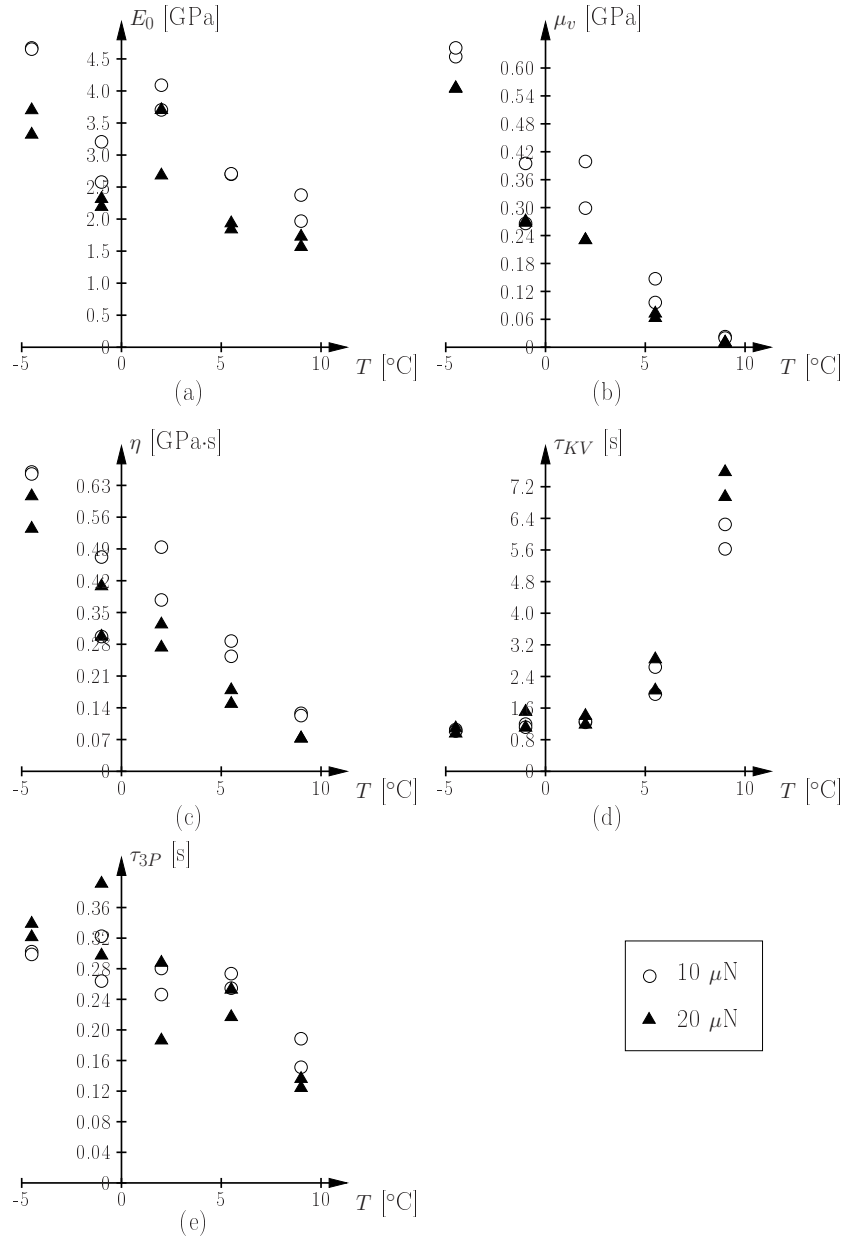
Figure A.12: Temperature dependence of 3P-model parameters: (a) E_0 [GPa],
    (b) μ_v [GPa], (c) η [GPa·s], (d) relaxation time of Kelvin-Voigt unit, τ_KV
    [s], and (e) relaxation/creep time τ_3P [s] involving all three parameters of
    the 3P model (NI-test conditions: P_max =10, 20 μN, $\dot{P} = dP/dt$ =20, 40
    μN/s, τ_H =10 s)

rates, maximum loads, and at different temperatures, and the respective model parameters
were identified. Based on the so-obtained parameters, the following conclusions can be
drawn:

1. An increase of the maximum load resulted in decreasing values for the identified
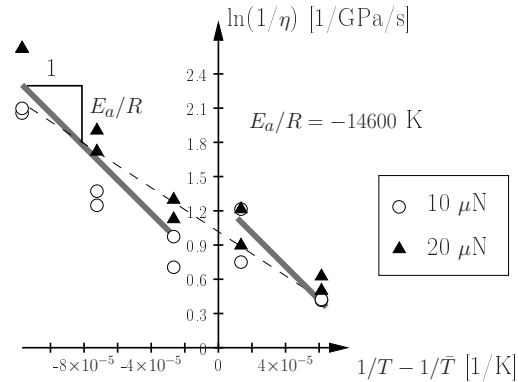
Figure A.13: Identification of Arrhenius-type law describing the temperature dependence of η [GPa·s] ($\bar{T} = 273$ K)

model parameters. This effect was explained by the heterogenity of the bitumen microstructure, consisting of both high-viscous strings embedded into a low-viscous matrix.

2. In contrast to the maximum load, affecting the bitumen microstructure to a different extent, the loading rate – which affects the time-dependent, viscoelastic model response and, therefore, reflects the performance of the employed parameter-identification tool – showed no influence on the identified parameters.

3. The temperature dependence of the viscosity η was successfully described by an Arrhenius-type law.

The three-parameter model employed for parameter identification gave excellent agreement between the experimentally-obtained NI-penetration curves and the model response. This agreement in the short-term creep response of bitumen was also observed in the course of bending-beam-rheometer (BBR) tests. However, as reported in Lackner et al. (2005), for an extended time range of testing, the non-linear dash-pot is able to capture both the short- *and* long-term response of bitumen (Lackner et al. 2005). The extension of the presented parameter-identification approach to more complex visco-elastic models, including the nonlinear dash-pot model, is a topic of ongoing research.

Publication B

Finer-scale extraction of viscoelastic properties from nanoindentation characterized by viscoelastic-plastic response (Jäger and Lackner 2007)

Authored by Andreas Jäger and Roman Lackner
Accepted for publication in *Strain*

Motivated by recent progress in viscoelastic indentation analysis, the identification of viscoelastic properties from materials exhibiting elastic, viscous and plastic material behavior by means of nanoindentation is dealt with in this paper. Based on existing solutions for pure viscoelastic material behavior, two methods allowing us to consider the effect of plastic deformation are presented: (i) the so-called double-indentation technique, with the second indentation characterized by pure viscoelastic material response and (ii) the use of spherical indenter geometries instead of commonly used pyramidal indenters avoiding plastic deformation at all. Both methods are applied to three different polymers, giving access to the model parameters of the fractional dash-pot which is used to describe the viscoelastic behavior. The results obtained are compared with results from standard (single) indentation tests using a Berkovich indenter. Moreover, the influence of the maximum load, determining the amount of plastic material response, on the identified model parameters is investigated. Finally, the creep-compliance functions identified by nanoindentation are compared with the respective macroscopic creep-compliance functions obtained from bending-beam rheometer tests.

B.1   Introduction

Recent progress in both finer-scale experimentation (atomic force microscopy, nanoindentation, etc.) and theoretical and numerical upscaling schemes provides the basis for the development of so-called multiscale models, taking finer scales of observation for describing and predicting macroscopic material behavior into account. The success of multiscale models is strongly linked to the proper identification of material properties at finer scales, serving as input for the upscaling schemes mentioned. In this paper, extraction of viscoelastic material parameters by means of the nanoindentation technique is presented. Parameter identification of materials exhibiting only elastic and time-dependent material response is based on the measured increase of penetration during the so-called holding phase of the measured penetration history (Cheng et al. 2000, 2005; Larrson and Carlsson 1998; Sakai and Shimizu 2001; Sakai 2002; Lu et al. 2003; Oyen and Cook 2003; Oyen et al. 2004; Oyen 2005; Cheng and Cheng 2004; Vandamme and Ulm 2006; Jäger et al. 2007a,b) (see Figure B.1(a)). Hereby, experimental data are compared with the respective
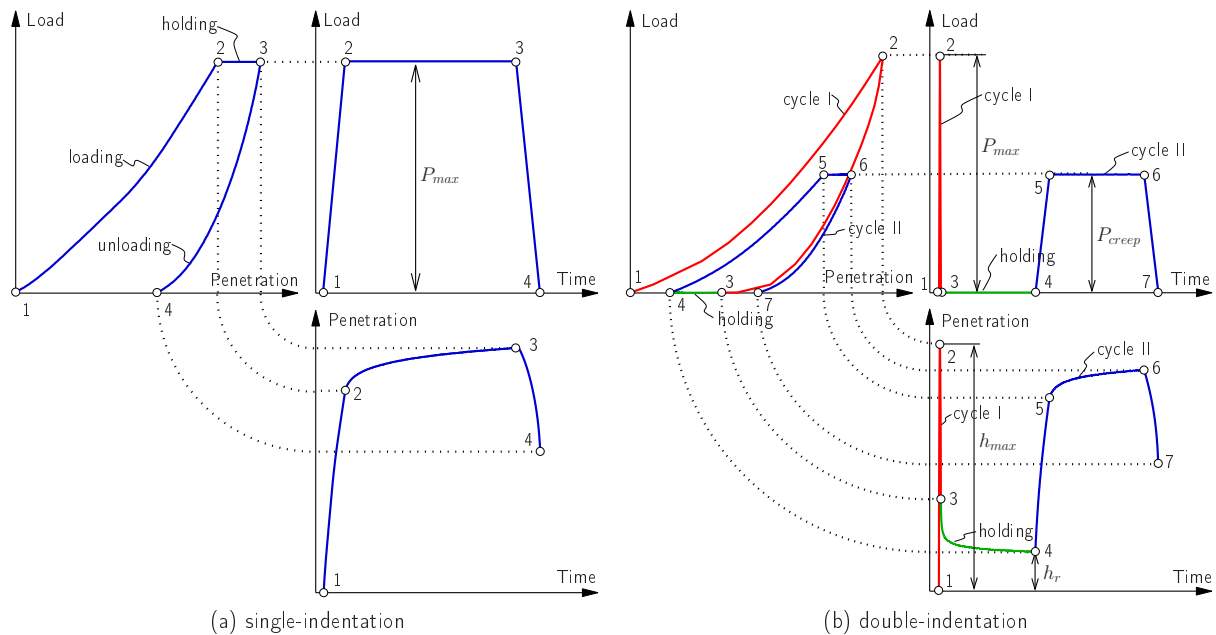

Figure B.1: Load-penetration curve, load history, and penetration history for (a) single-indentation test and (b) double-indentation test on material exhibiting elastic, viscous, and plastic material response

data from analytical solution for the mathematical problem of a rigid indenter penetrating a viscoelastic medium (Lee 1955; Radok 1957; Lee and Radok 1960; Hunter 1960; Graham 1965, 1967; Yang 1966; Ting 1966, 1968), giving access to the parameters of the underlying viscoelastic model. Such back-analysis schemes, however, are only applicable to materials showing no plastic behavior. In case of plastic deformation occurring during the loading phase of nanoindentation tests, both plastic and viscoelastic deformations

would be assigned to the viscoelastic material response, leading to wrong parameters for the underlying viscoelastic model overestimating the viscoelastic material response (Oyen and Cook 2003; Shimizu et al. 1999; Sakai et al. 2002; Zhang et al. 2005). In order to account for the effect of plastic deformation, two methods are presented in this paper: (i) the double-indentation technique and (ii) use of spherical indenter geometries instead of the commonly used pyramidal indenters.

As regards the double-indentation technique (see Section B.2), the effect of plastic deformation is determined by adapting the experimental setup (change of load history) and considered in the employed parameter-identification scheme. The motivation for using spherical indenter geometries, on the other hand, is to avoid the development of plastic deformation by reducing the stresses under the indenter during the indentation process. Therefore, the experimental setup used for a single indentation (trapezoidal load history) may be employed when using spherical indenters and the parameter identification scheme must be extended towards spherical tip geometries (see Section B.3). In order to assess the performance of the two methods presented, tests on three polymers are conducted using either a Berkovich or a cono-spherical tip and employing both the single- as well as the double-indentation method (see Section B.4). The model parameters identified from the experimental data are presented and discussed in Section B.5. Concluding remarks are given in Section B.6.

B.2   Single- versus double indentation

Recently, pre-loading of the material was performed by Zhang et al. (2005), leading to the so-called double-indentation technique (see Figure B.1(b)). Hereby, the load history is characterized by two load cycles, with the first cycle (pre-loading) leading to plastic deformation and the second cycle showing only viscoelastic deformation. Thus, the latter is suitable for back calculation of viscoelastic properties using analytical solutions for the respective viscoelastic indentation problem. The second load cycle is characterized by the penetration of a tip into the imprint resulting from the first load cycle. In the elastic case, this reloading cycle may be described by the contact problem of two conforming solids (Steuermann 1939; Perrson 1964; Goodman and Keer 1965; Johnson 1992). More refined models, considering, e.g., the shape of the plastic imprint, were presented in Stilwell and Tabor (1961), Pharr and Bolshakov (2002), and Sakai (2003). In this paper, the concept of effective indenters as proposed in Sakai (2003) is employed. According to Sakai (2003), the reloading indentation process (second cycle) into a plastic imprint (stemming from the first cycle) can be approximated by the indentation of a tip with an effective tip shape into a flat undeformed surface. Hereby, the face angle β of the original pyramidal indenter is replaced by an effective face angle $\beta_{\text{eff}} = \beta - \beta_{\text{r}}$, with $\tan \beta_{\text{r}} = h_{\text{r}}/h_{\text{c}} \tan \beta$. Hereby, h_{r} is the residual penetration after the first load cycle and h_{c} is the contact height at maximum load of the first load cycle. Following this idea, adaptation of the tip-shape

function $f(\rho)$ (see Figure B.2), already used in the identification scheme reported in Jäger et al. (2007a), is proposed in this paper. Hereby, the effective tip shape is given as
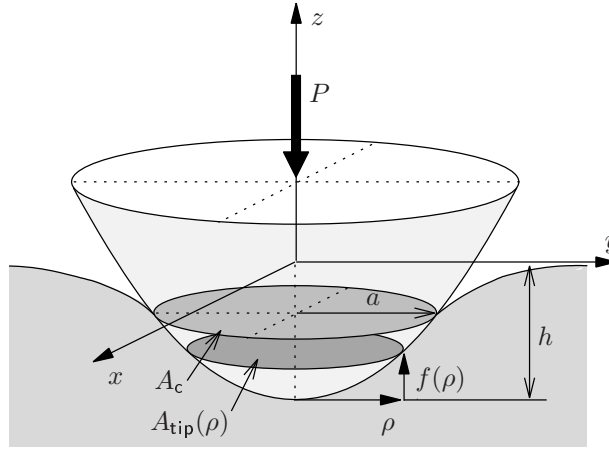

Figure B.2: Contact between rigid axisymmetric indenter of shape $f(\rho)$ and an infinite half-space (P is the applied load, h is the penetration, and a is the contact radius)

$$f_{\text{eff}}(\rho) = (1 - \frac{h_{\text{r}}}{h_{\text{max}}})f(\rho) \ , \tag{B.1}$$

where h_{c} was replaced by h_{max} (penetration at point 2 see Figure B.1(b)) in order to avoid the use of wrong values of h_{c} resulting from negative values of S, i.e., the initial unloading slope of the load-penetration curve, occurring during testing of low viscous materials. The residual penetration h_{r} is the value of the penetration at point 4 (see Figure B.1(b)), accounting for the viscoelastic deformation taking place during the holding period after unloading, reducing the residual penetration depth. The identification of model parameters is identical to the identification scheme proposed in Jäger et al. (2007a), considering the holding phase of the second load cycle and the effective tip shape $f_{\text{eff}}(\rho)$.

B.3   Parameter identification of viscoelastic properties

For identification of viscoelastic properties, the procedure outlined in Jäger et al. (2007a) and Jäger et al. (2007b) is followed. Hereby, the tip shape is approximated by the distance

$$f(\rho) = \frac{1}{2C_0} \left(\sqrt{C_1^2 + 4C_0\rho^2\pi} - C_1 \right) \ . \tag{B.2}$$

from the apex of the axisymmetric tip as a function of the radius ρ [m] (see Figure B.2), giving the cross-section area of the tip, A_{tip}, as

$$A_{\text{tip}}(\rho) = \rho^2\pi = C_0 f(\rho)^2 + C_1 f(\rho) \ , \tag{B.3}$$

Similar to the procedure proposed in Thurn and Cook (2002), the tip shape is described by two constants, C_0 [-] and C_1 [m], which are obtained from calibration of the nanoindentation-testing equipment (see Section B.4). With these two constants and the function $f(\rho)$ both, perfect cones with a semi-apex angle α ($C_0 = \pi \tan^2 \alpha$, $C_1 = 0$) and perfect spheres with a tip radius R ($C_0 = -\pi$, $C_1 = 2R\pi$) can be described. As regards the required solution of the elastic indentation problem, the solution outlined in Jäger et al. (2007a), applicable only to tip shapes characterized by $C_0 > 0$ and $C_1 > 0$, is extended to a more general solution also including the special case of spherical tip shapes ($C_0 < 0$ and $C_1 > 0$, $\rho \le \rho_{\max}$, with $\rho_{\max} = \sqrt{-C_1^2/(4C_0\pi)}$). According to the so-called Sneddon solution (Sneddon 1965), the relation between the penetration h [m] and the corresponding load P [N] is given for an axisymmetric indenter of shape $f(\rho)$ penetrating an elastic half-space by

$$h = a \int_{\rho=0}^{a} \frac{f'(\rho)d\rho}{\sqrt{a^2 - \rho^2}} \qquad P = 2\frac{E}{1-\nu^2} \int_{\rho=0}^{a} \frac{\rho^2 f'(\rho)d\rho}{\sqrt{a^2 - \rho^2}} \; . \tag{B.4}$$

Hereby, a [m] is the radius of the projected contact area A_c, E is Young's modulus, ν is Poisson's ratio, and $f' = df/d\rho$. Inserting Equation (B.2) into Equation (B.4) gives the penetration and the applied load as a complex function of the contact radius a, reading

$$h = \frac{1}{2\sqrt{C_0}} \left(ia\sqrt{\pi} \left(\log\left[-\frac{i(C_1^2 + 4a^2 C_0 \pi)}{\sqrt{C_0}} \right] - \log\left[4aC_1\sqrt{\pi} + \frac{i(-C_1^2 + 4a^2 C_0 \pi)}{\sqrt{C_0}} \right] \right) \right) , \tag{B.5}$$

$$\begin{aligned} P &= \frac{E}{1-\nu^2} \frac{1}{8C_0^{3/2}\sqrt{\pi}} \left(4aC_1\sqrt{C_0}\pi - i(C_1^2 - 4a^2 C_0 \pi) \right. \\ &\quad \left. \left(\log\left[-\frac{i(C_1^2 + 4a^2 C_0 \pi)}{\sqrt{C_0}} \right] - \log\left[4aC_1\sqrt{\pi} + \frac{i(-C_1^2 + 4a^2 C_0 \pi)}{\sqrt{C_0}} \right] \right) \right) \\ &= MF(a) \end{aligned} \tag{B.6}$$

where M is the indentation modulus, with $M = E/(1-\nu^2)$ and

$$\begin{aligned} F(a) &= \frac{1}{8C_0^{3/2}\sqrt{\pi}} \left(4aC_1\sqrt{C_0}\pi - i(C_1^2 - 4a^2 C_0 \pi) \right. \\ &\quad \left. \left(\log\left[-\frac{i(C_1^2 + 4a^2 C_0 \pi)}{\sqrt{C_0}} \right] - \log\left[4aC_1\sqrt{\pi} + \frac{i(-C_1^2 + 4a^2 C_0 \pi)}{\sqrt{C_0}} \right] \right) \right) \end{aligned} ,\tag{B.7}$$

is a function depending only on geometrical properties, such as the tip shape (described by C_0 and C_1) and the contact radius a. It is noted, that for arbitrary values of C_0 and C_1 Equations (B.5) and (B.6) always give real numbers for h and P. For negative values of C_0 (spherical shape), the contact radius is restricted by

$$a \le \rho_{\max} = \sqrt{\frac{-C_1^2}{4C_0\pi}} \; , \tag{B.8}$$

with ρ_{max} as the maximum possible radius ρ.

Based on the analytical solution of the elastic indentation problem (Equations (B.5) and (B.6)) for the tip shape given in Equation (B.3), the viscoelastic solution is obtained by the application of the method of functional equations (Lee and Radok 1960). Hereby, the elastic operators P, M, and $F(a)$ in Equation (B.6) are replaced by their Laplace transforms $\widehat{P(s)}$, $\widehat{M(s)}$, and $\widehat{F(a(s))}$, giving after re-arrangement

$$F\widehat{(a(s))} = \frac{\widehat{P(s)}}{\widehat{M(s)}} = \frac{1}{s\widehat{M(s)}}s\widehat{P(s)} = \widehat{\bar{Y}(s)}s\widehat{P(s)} \ , \tag{B.9}$$

where $1/(s\widehat{M(s)})$ was replaced by the Laplace transform of $\bar{Y}(t)$, referred to as indentation compliance function in the following. Back-transformation to the time domain gives

$$F(a(t)) = \int_0^t \bar{Y}(t-\tau)\frac{dP(\tau)}{d\tau}d\tau \ . \tag{B.10}$$

The left-hand side of Equation (B.10) depends only on geometric properties, i.e., the constant parameters C_0 and C_1, and on the experimentally obtained contact radius $a(t)$. The right-hand side of Equation (B.10), on the other hand, depends on the mechanical properties of the viscoelastic half-space represented by the indentation compliance function $\bar{Y}(t)$ and the load history $P(t)$. The still unknown contact radius a is determined from the measured penetration h using Equation (B.5).

For identification of viscoelastic model parameters for the materials presented in the following section, a fractional dash-pot is used. The respective creep-compliance function reads

$$J(t) = J_{\mathrm{a}}(t/\bar{\tau})^k \ , \tag{B.11}$$

where J_{a} [GPa^{-1}] is the creep compliance at $t = \bar{\tau}$ and k [-] is the creep exponent, with $0 \leq k \leq 1$. $\bar{\tau}$ is introduced for dimensional reasons and is set equal to 1 s. The fractional dash-pot is able to cover a wide range of material behavior from pure elastic ($k = 0$) to pure viscous ($k = 1$) materials. Considering the indentation compliance function for incompressible materials, with $\bar{Y}(t) = J(t)/4$, Equation (B.10) becomes, for the fractional dash-pot and the holding phase of a trapezoidal load history (Jäger et al. 2007b),

$$
\begin{aligned}
F_{\mathrm{H}}(J_{\mathrm{a}}, k, t) &= \int_0^t 1/4 J(t-\tau)\frac{dP(\tau)}{d\tau}d\tau \\
&= \frac{P_{\mathrm{max}}}{4\tau_{\mathrm{L}}}\left\{ J_{\mathrm{a}}\frac{1}{(k+1)}\left(\frac{1}{\bar{\tau}}\right)^k \left[t^{k+1} - (t-\tau_{\mathrm{L}})^{k+1}\right] \right\} \ ,
\end{aligned}
\tag{B.12}
$$

where τ_{L} [s] is the loading duration. In order to determine model parameters from nanoindentation-test data, the error between the analytical model response (Equation

(B.12)) and $F(a(t))$ obtained from the nanoindentation-test data (Equation (B.7)), denoted as F_{exp}, is minimized within the holding phase by adapting the unknown model parameters J_{a} and k. The mentioned error is defined by

$$R(J_{\text{a}}, k) = \frac{e(J_{\text{a}}, k)}{u} \; , \tag{B.13}$$

with

$$e^2(J_{\text{a}}, k) \;\; = \;\; \sum_{i=1}^{n}[F_{\text{exp}}\{a[h(t_{\text{i}})]\} - F_{\text{H}}(J_{\text{a}}, k, t_{\text{i}})]^2 \;\; < \tag{B.14}$$

and

$$u^2 = \sum_{i=1}^{n} F_{\text{exp}}^2(t_{\text{i}}) \; , \tag{B.15}$$

with t_{i} denoting different time instants within the holding phase.

As regards the double-indentation technique, the tip-shape function $f(\rho)$ is replaced by the effective tip shape $f_{\text{eff}}(\rho) = (1 - h_{\text{r}}/h_{\text{max}})f(\rho)$. Considering $f_{\text{eff}}(\rho)$ in the presented identification scheme, the functions describing the tip shape given in Equations (B.7) and (B.5) are adapted, reading $F_{\text{exp,eff}}(a) = (1 - h_{\text{r}}/h_{\text{max}})F_{\text{exp}}(a)$ and $h_{\text{eff}} = (1 - h_{\text{r}}/h_{\text{max}})h$. Moreover, $t = 0$ refers to the beginning of the second load cycle (point 4 in Figure B.1(b)).

B.4   Materials and experimental setup

Three different polymers, i.e., low density polyethylene (LDPE), polymethyl methacrylate (PMMA), and polycarbonate (PC), are considered in this study. The respective values for Young's modulus and Poisson's ratio were taken from the literature and are listed in Table B.1. Nanoindentation tests were conducted at room temperature using

Table B.1: Young's modulus and Poisson's ratio of considered polymers

Polymer (source)	LDPE (www.matweb.com)	PMMA (www.matweb.com)	PC (Bayer Industry Services)
Young's modulus [GPa]	0.139–0.35	1.8–3.1	2.3–2.4
Poisson's ratio [-]	0.38	0.35–0.4	0.37

a Hysitron Triboindenter nanoindenter (Hysitron, Minneapolis, MN, USA) with a three-sided Berkovich diamond tip and a cono-spherical tip with a nominal tip radius of 5 μm. All tests were performed with a closed loop feedback control, providing a constant load during the holding phase of the test. As the drift correction gave unstable results, the drift correction was de-activated for all nanoindentation tests conducted.

The load history of the single indents (see Figure B.1(a)) is characterized by a loading phase with a duration of 3 s followed by a holding phase of 20 s at maximum load. During double indentation, the load was applied in 0.2 s in the first load cycle and then reduced to 1 µN in 0.2 s. After a holding phase of 20 s at a load of 1 µN, the load was increased again in 3 s to 50 % of the load applied in the first load cycle, and held constant for 20 s. In order to study the dependence of the identified model parameters on the load considered during the nanoindentation test, the following maximum loads were applied: (i) LDPE: 1000, 750, 500, 250, 125, 50 µN for the Berkovich tip and 750, 500, 375, 250, 125, 50, 25 N for the spherical tip; (ii) PMMA: 10000, 7500, 5000, 2500, 1000, 500, 250, 100, 50 µN for both tip shapes; (iii) PC: 10000, 7500, 5000, 2500, 1000, 60 µN for both tip shapes.

For determination of the macroscopic creep-compliance function, bending-beam-rheometer tests were performed. Hereby, a specimen with the height h [mm] and the width b [mm] is placed horizontally on two bearings (spacing $l = 102$ mm). During the test, a constant load F is applied for 240 s at the midspan of the beam. The compliance function $J(t)$ is obtained from the measured increase of the mid-span deflection $u(t)$ by extending the solution for the elastic case

$$u = \frac{Fl^3}{4bh^3}\frac{1}{E} = \frac{Fl^3}{4bh^3}\frac{1}{2(1+\nu)G} = \frac{Fl^3}{12bh^3}\frac{1}{G} \tag{B.16}$$

where an incompressible material behavior (Poisson's ratio $\nu = 0.5$) is assumed, to the case of viscoelastic deviatoric behavior, replacing $1/G$ by $J(t)$, reading

$$J(t) = \frac{12bh^3}{Fl^3}u(t) \tag{B.17}$$

B.4.1 Tip-shape calibration

The area function of the Berkovich tip was obtained by the standard calibration procedure outlined in Oliver and Pharr (1992) using fused quartz (FQ) as calibration material. For the cono-spherical tip, on the other hand, additionally single crystal aluminum (Al) was used for the calibration, giving access to the area function for larger penetrations (up to 1.2 µm). The calibration procedure, however, is the same for both materials and tip shapes:

1. Perform indents in a material with given elastic properties (e.g., fused quartz) in the depth range of the indentation experiments.

2. Compute the projected contact area $A_c = \pi/4(S/M)^2$, where S [N/m] is the initial unloading slope of the load-penetration curve and M is the indentation modulus, with $M = E/(1 - \nu^2)$, where $E = 72$ GPa and $\nu = 0.17$ for fused quartz.

3. Plot A_c for different contact depths h_c, with $h_c = h - 0.75 P_{max}/S$, and approximate the so-obtained relation by

$$A_c = C_0 h_c^2 + C_1 h_c , \tag{B.18}$$

where C_0 [-] and C_1 [m] are constants describing the tip shape.

The machine compliance, required for determination of the correct penetration depth in the calibration procedure, was determined according to Hysitron Inc. (2006) using the Berkovich tip.

Figure B.3 shows the area function $A_{tip}(f(\rho))$ for the Berkovich and the cono-spherical tip. Although the shape of the Berkovich tip is well approximated by a cone over the

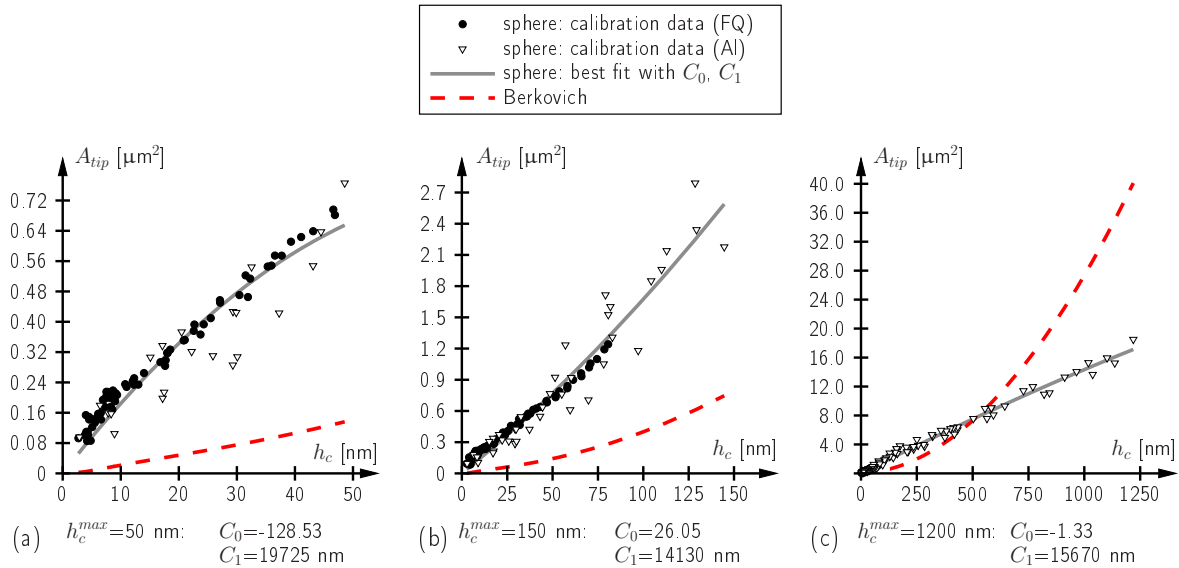Figure B.3: Area function A_{tip} for Berkovich and cono-spherical tip plotted for different penetration depths (values for C_0 and C_1 refer to cono-spherical tip)

whole penetration range (C_0 and C_1 remain positive and approximately constant), the shape of the cono-spherical tip changes from spherical (Figure B.3(a)) to conical (Figure B.3(b)) and again to spherical (Figure B.3(c)). These findings were also observed in scanning-electron-microscopy images (see Figure B.4), showing the mentioned change of the tip shape from spherical, to conical, and again to spherical.

B.5   Results and discussion

All three polymers were tested considering different values for the maximum load using the single- and double-indentation technique using the Berkovich and the cono-spherical tip. For each maximum load, at least nine indents were conducted and mean values for the
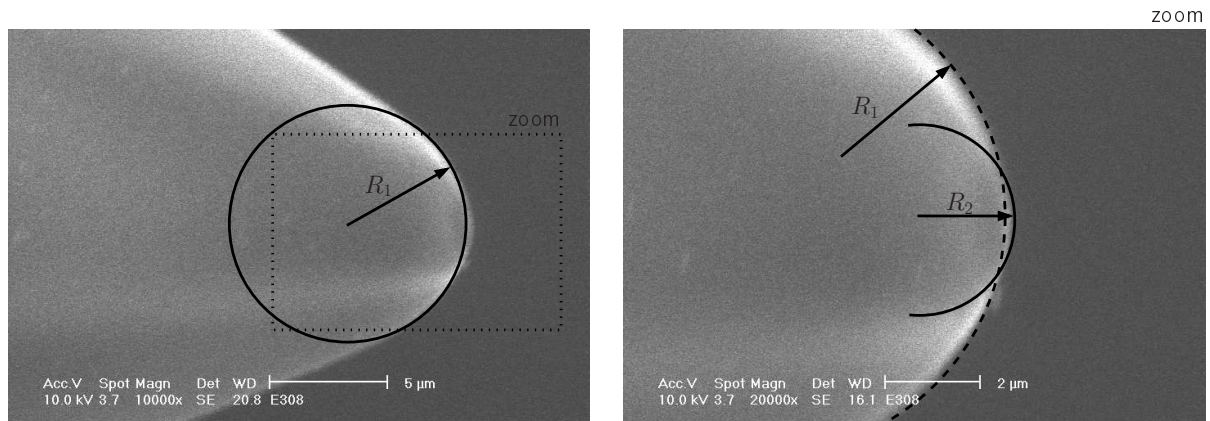
Figure B.4: Scanning electron microscope image of employed cono-spherical tip showing the change of the tip shape

identified parameters for the fractional dashpot, J_a and k, were computed. Figures B.5 to B.7 show the identified model parameters as a function of the maximum penetration depth which is directly related to the respective maximum applied loads, for LDPE, PMMA, and PC obtained for single and double indentation for both tip shapes.

For all four test setups (single and double indentation using a Berkovich or a cono-spherical tip) a higher variation of the creep exponent at small loads is observed. This variation is assigned to the influence of the drift during NI testing, which is more pronounced for small penetrations.

As regards the results from testing with the Berkovich tip, both methods reveal a similar load dependence of J_a and k for all three materials, reaching a constant value of both parameters as the maximum load increases (see Table B.2). Comparing the identified parameters obtained from single- and double indentation, the single-indentation technique was found to overestimate the initial creep compliance for all three polymers, which is explained by the occurrence of plastic deformation. The creep exponent, on the other hand, is only slightly underestimated by the single-indentation technique.

The results obtained from testing with the cono-spherical tip show a quite different dependence of the identified parameters on the maximum load. For very small penetration depths, for which the tip shape is spherical (see Subsection B.4.1), the single- and double-indentation technique give the same values for the model parameters. Furthermore, these values agree very well with the results from double indentation using the Berkovich tip. However, with increasing penetration depth, the model parameters obtained from single indentation using the cono-spherical tip increase continuously. This increase is explained by the larger amount of plastic deformation as the penetration depth increases. The model parameters obtained from double indentation, on the other hand, show a different behavior with the highest value for both parameters at a minimum penetration depth of about 300 nm. Although the initial creep compliance seems to reach a constant value
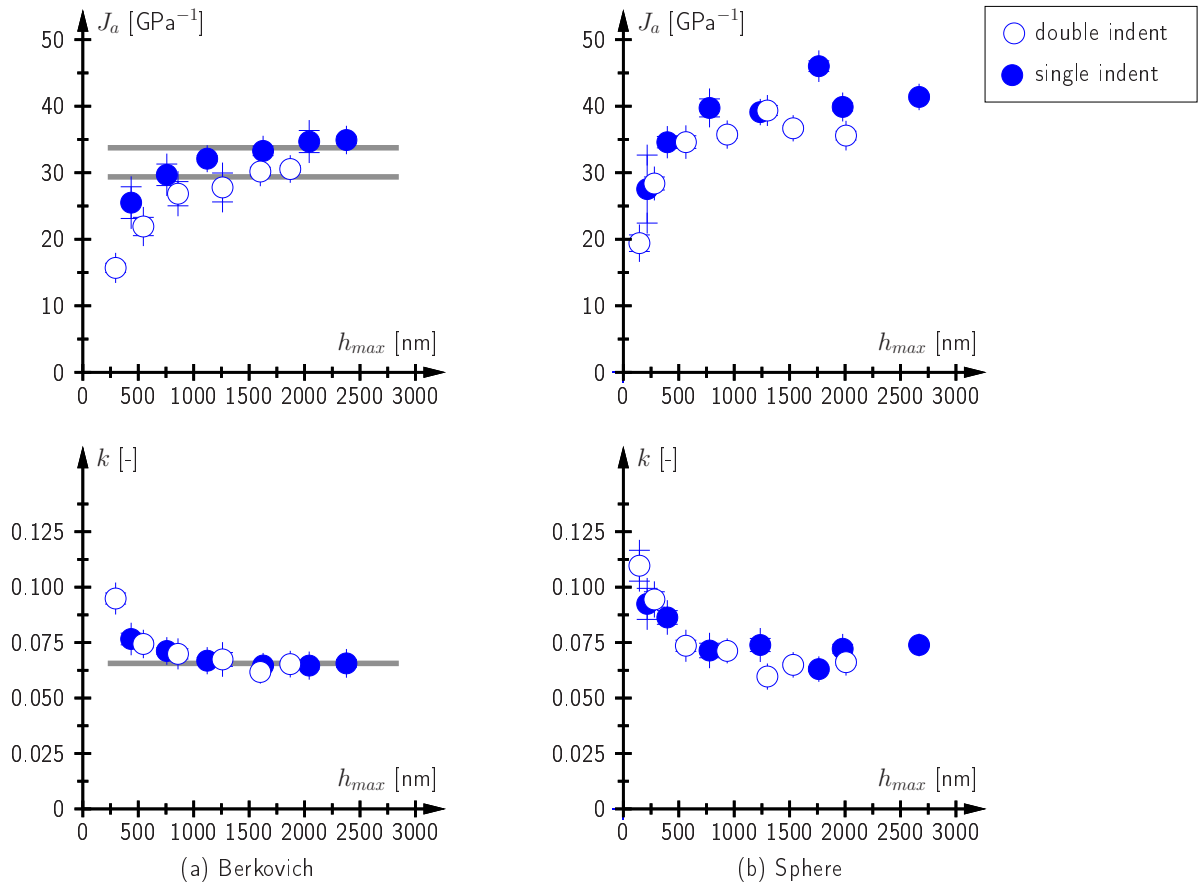
Figure B.5: Fractional dash-pot parameters for LDPE obtained from single- and double indentation using (a) a Berkovich tip and (b) a cono-spherical tip for different values of $h_{\max}$

Table B.2: Initial creep compliance J_a and creep exponent k for considered polymers obtained from single- and double-indentation testing using a Berkovich and a cono-spherical tip

		Test method	LDPE	PMMA	PC
Initial creep compliance J_a[GPa^{-1}]	Berkovich	single-indentation	33.75	1.00	1.77
		double-indentation	28.84	0.81	1.01
	cono-spherical		27.00	0.90	1.10
Creep exponent k [-]	Berkovich	single-indentation	0.065	0.093	0.037
		double-indentation	0.066	0.105	0.049
	cono-spherical		0.090	0.090	0.045

for increasing penetration depth, the creep exponent increases continuously. This variation of the identified parameters is assigned to the tip shape, changing from spherical to
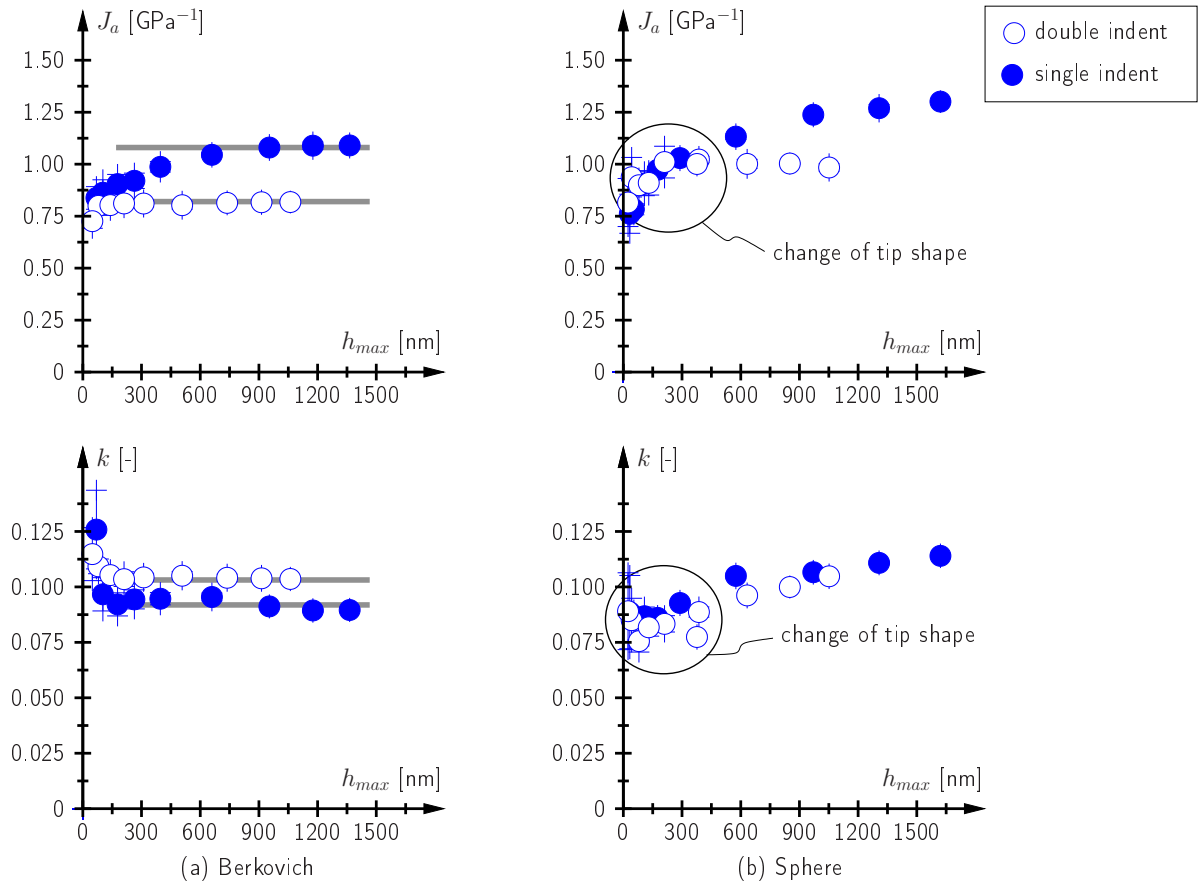
Figure B.6: Fractional dash-pot parameters for PMMA obtained from single- and double indentation using (a) a Berkovich tip and (b) a cono-spherical tip for different values of $h_{\max}$

conical and to spherical again (see Figure B.3). As the employed calibration procedure for the tip shape is based on two parameters (C_0 and C_1), the complicated tip shape is well approximated only for small penetration depths (within the first spherical region). In fact, for such penetration depths, both the single- and double-indentation technique give the similar results to those obtained from double indentation using the Berkovich tip, highlighting the purely viscoelastic behavior in case of penetration using a spherical tip.

In order to assess the identified model parameters, the creep-compliance function (Equation (B.11)) is plotted for all three polymers using the parameters given in Table B.2 (see Figure B.8) and compared with the creep-compliance function obtained from bending-beam-rheometer tests using Equation (B.17). In contrast to the results obtained from single indentation, the creep-compliance function corresponding to model parameters identified via double indentation shows a good agreement with the macroscopic test results for all three materials considered. Especially in case of PC, showing the highest
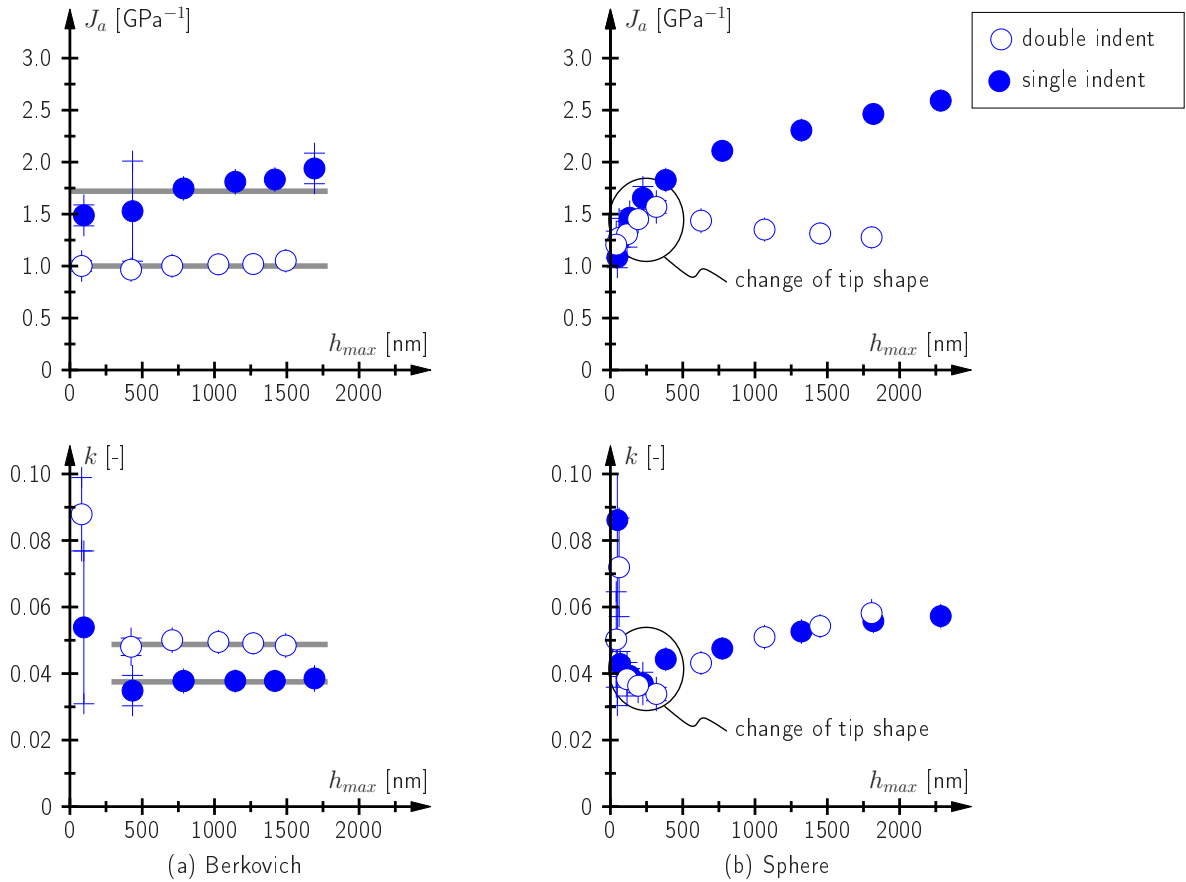
Figure B.7: Fractional dash-pot parameters for PC obtained from single- and double indentation using (a) a Berkovich tip and (b) a cono-spherical tip for different values of $h_{\max}$

amount of plastic deformation, the parameters identified via single indentation lead to a creep-compliance function significantly overestimating the macroscopic properties. The creep-compliance function corresponding to the model parameters identified via double indentation, on the other hand, agrees well with the compliance function obtained from the bending-beam-rheometer test.

B.6   Summary and conclusions

The identification of viscoelastic model parameters from indentation tests was dealt with in this paper. Accounting for the plastic material response during the loading phase of indentation tests, results from single and double indentation using a Berkovich and a spherical tip were presented. The parameters for the fractional dash-pot, describing the viscoelastic behavior of the three types of polymers considered, were determined from back-calculation using the increase of penetration during the holding phase of the indentation test. Based on the so-obtained model parameters, the following conclusions
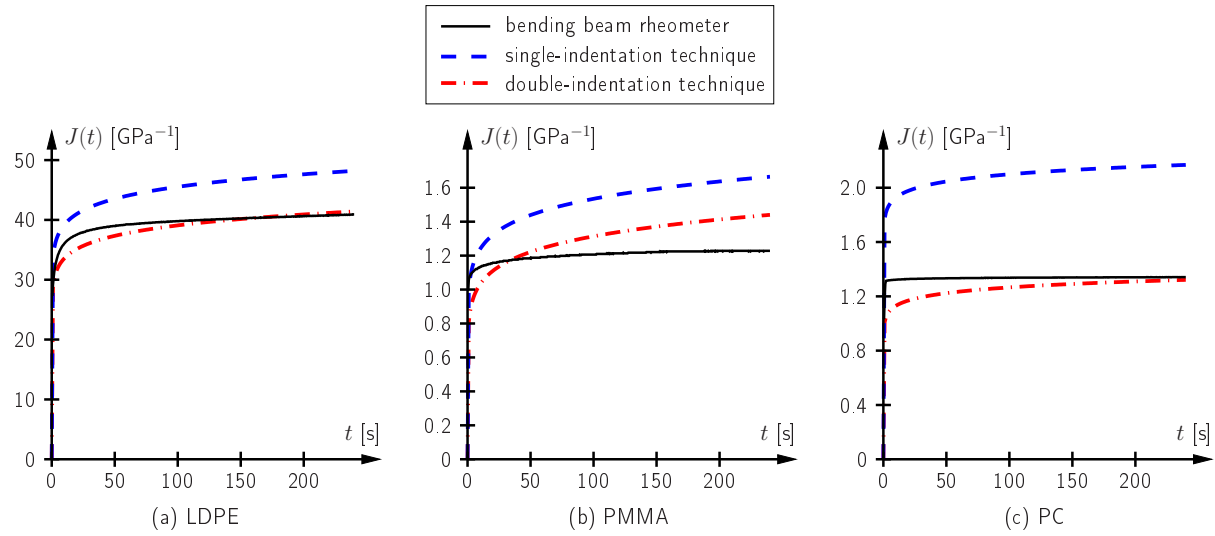
Figure B.8: Creep-compliance function obtained from single- and double-indentation technique using a Berkovich tip for (a) LDPE, (b) PMMA, and (c) PC compared with creep-compliance functions obtained from bending-beam-rheometer tests

can be drawn:

1. The initial creep compliance of the fractional dash-pot identified via single indentation overestimates the creep compliance obtained from double indentation, which is explained by assigning the plastic deformation to the viscoelastic material response, giving higher values for the initial creep compliance.

2. For spherical tip shapes (within the first spherical region of the cono-spherical tip), the same parameters were identified using single and double indentation, indicating that no plastic deformation occurred during the indentation process. Furthermore, the identified parameters agreed well with results from double indentation using the Berkovich tip indicating the correct consideration of the plastic deformation in the presented double-indentation technique.

3. The parameters determined via single indentation lead to a creep-compliance function significantly overestimating the creep-compliance function obtained from bending-beam-rheometer tests. The creep-compliance function obtained from the model parameters identified via double indentation using the Berkovich tip as well as using the spherical tip, on the other hand, showed good agreement with the macroscopic properties, highlighting the good performance of the presented double-indentation technique.

In summary, both the double-indentation technique as well as the use of spherical indenters were found to be appropriate for considering/avoiding plastic deformation during

the identification of viscoelastic model parameters for materials exhibiting viscoelastic and plastic material behavior. The conventional single-indentation technique using a Berkovich tip, on the other hand, may be employed in exceptional cases of materials dominated by viscoelastic material response, such as low-density polyethylene.

Publication C

Identification of viscoelastic model parameters by means of cyclic nanoindentation testing (Jäger and Lackner 2008)

Authored by Andreas Jäger and Roman Lackner

A method for the identification of model parameters describing the time-dependent material behavior by means of cyclic nanoindentation is presented. Hereby, the complex shear modulus of the material sample is determined from the prescribed amplitude in the load history, the measured amplitude in the penetration history, and the phase shift between the peak values for the load and the penetration. The parameters for a specific viscoelastic model are obtained by comparing the experimentally-obtained storage and loss moduli – both depending on the frequency used during cyclic testing – with the analytical expressions for the respective viscoelastic model. The presented method is applied to low-density polyethylene, giving access to the parameters of the fractional dash-pot which is used to describe the viscoelastic behavior. The obtained results are compared with results from nanoindentation (static) creep tests, considering different maximum loads. Finally, the performance of the presented method is assessed by comparing the creep-compliance functions corresponding to the model parameters identified by nanoindentation with the macroscopic creep-compliance function obtained from bending-beam-rheometer tests.

C.1   Introduction

The nanoindentation technique is a well known tool for the identification of mechanical properties at the micro- and nanometer scale of materials. In case of elastic or elasto-plastic materials, Young's modulus can be determined from the unloading phase of the nanoindentation test (Oliver and Pharr 1992). Recently, methods for the identification of viscoelastic properties from materials exhibiting time-dependent response were developed (see, e.g., Cheng et al. (2000, 2005); Larrson and Carlsson (1998); Sakai and Shimizu (2001); Lu et al. (2003); Cheng and Cheng (2004); Jäger et al. (2007a)). Hereby, the measured increase of the penetration during the so-called holding phase is compared with the respective analytical solution for the mathematical problem of a rigid indenter penetrating a viscoelastic halfspace (Lee and Radok 1960). Another method for the identification of viscoelastic parameters is characterized by cyclic loading (Oliver and Pharr 1992; Pethica and Oliver 1987; Loubet et al. 1995; Syed Asif et al. 1999, 2001). Hereby, an oscillating load is applied to the tip and the amplitude of the penetration history and phase shift between the peak values for the penetration and the prescribed load history is measured. With these two parameters, the complex modulus and the phase angle of the material sample can be determined. Cyclic nanoindentation was applied in several studies for the mechanical characterization of polymers (Hayes et al. 2004; Odegard et al. 2005; Park et al. 2004; White et al. 2005; Li and Bhushan 2002). In all these publications, the viscoelastic behavior of the polymers was, if at all, described by a Kelvin–Voigt model.

In this paper, a tool for identification of parameters for various linear viscoelastic models, representing the time-dependent behavior of the material sample, is presented. For this purpose, the modeling of the dynamic response of the nanoindentation system in terms of complex stiffnesses is dealt with in the following section. Moreover, based on the complex stiffness of the whole system, determined from the measured load and penetration amplitude and the phase shift, the complex shear moduli of the tested material sample will be extracted, giving access to the parameters for a chosen viscoelastic model. The presented technique for parameter identification is illustrated for low-density polyethylene, with the material and testing specifications given in Section C.3. In order to assess the performance of the presented method, the obtained model parameters are compared with results from nanoindentation (static) creep tests and bending-beam-rheometer tests given in Section C.4.

C.2   Cyclic nanoindentation testing

During cyclic nanoindentation testing, the indenter tip is loaded by a constant load $\bar{P}$ superimposed by a sinusoidal cyclic load, giving a total load of $P(t) = \bar{P} + P_0 \sin(\omega t)$, with P_0 as the load amplitude and $\omega = 2\pi f$ as the angular frequency (f is the cyclic frequency). The amplitude of the penetration history and the phase shift between the peak

values of the load and the penetration history are recorded. Both test results depend not only on the tip-sample interaction but also on the dynamic behavior of the experimental set-up (see Figure C.1). Whereas the load frame can be modeled as a spring with the
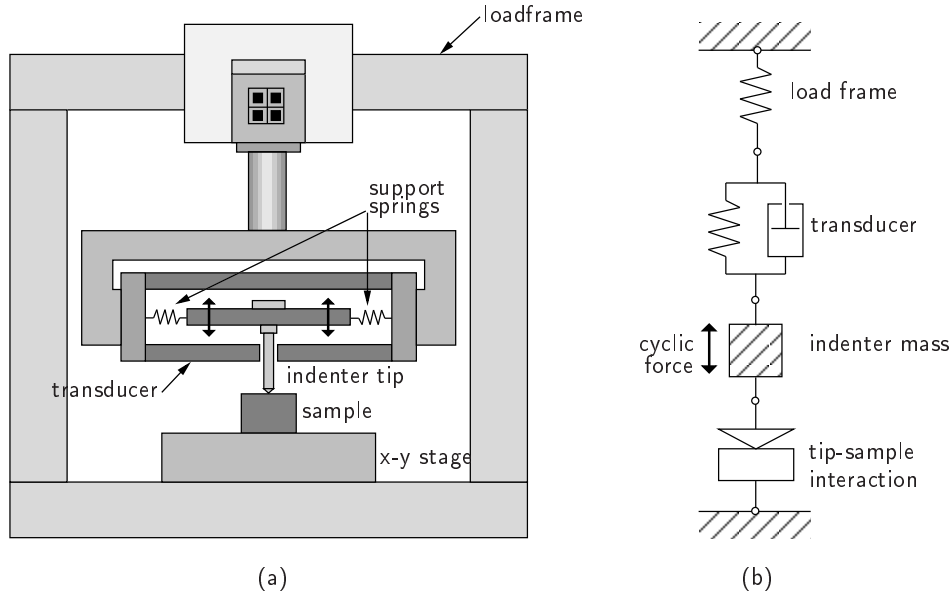

Figure C.1: (a) Nanoindentation system and (b) mechanical representation of different components.

stiffness c_f [N/m], the mechanical behavior of the transducer controlling the applied load is approximated by a Kelvin–Voigt element, with the spring stiffness c_t [N/m] and the damping coefficient D_t [Ns/m]. The mass of the indenter tip m [g] and the parameters c_f, c_t, and D_t are determined during the calibration of the nanoindentation-testing equipment (Hysitron Inc. 2006). Finally, the interaction between the indenter tip and the sample material within the mechanical model depicted in Figure C.1(b) is considered by the contact stiffness S [N/m], given by

$$S = \frac{\mathrm{d}P}{\mathrm{d}h} = 2M\frac{\sqrt{A_\mathrm{c}}}{\sqrt{\pi}} \tag{C.1}$$

where P [N] is the load, h [m] is the penetration, M [GPa] is the indentation modulus, and A_c [m^2] is the contact area. The penetration history, $h(t)$, resulting from the sinusoidal loading is given by

$$h(t) = h_0 \sin(\omega t - \phi) \tag{C.2}$$

where h_0 is the amplitude of the penetration history and ϕ is the phase angle. The ratio between the amplitude in the prescribed force history and the measured penetration history gives the complex stiffness of the mechanical model as

$$\frac{F_0}{h_0(\omega)} = |c^*_\mathrm{total}(\omega)| = |c'_\mathrm{total}(\omega) + ic''_\mathrm{total}(\omega)| = \sqrt{c'^2_\mathrm{total}(\omega) + c''^2_\mathrm{total}(\omega)} \tag{C.3}$$
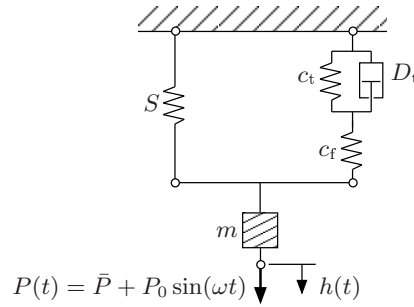
Figure C.2: Mechanical model representing the nanoindentation system loaded by cyclic force $P(t)$.

with c'_{total} and c''_{total} as the total storage and loss stiffness, respectively. The phase angle ϕ is defined by

$$\tan \phi(\omega) = \frac{c''_{\text{total}}(\omega)}{c'_{\text{total}}(\omega)} \tag{C.4}$$

Based on the mechanical model given in Figure C.2, the complex stiffness is given by

$$c^*_{\text{total}}(\omega) = S^*(\omega) + c^*_{\text{m}}(\omega) + c^*_{\text{f+t}}(\omega) \tag{C.5}$$

where S^* [N/m] and $c^*_{\text{f+t}}$ [N/m] represent the complex stiffness of the tip-sample interaction and the nanoindentation-testing equipment, respectively, and

$$c^*_{\text{m}}(\omega) = -m\omega^2 \tag{C.6}$$

accounts for the inertia of the indenter mass, with $c'_{\text{m}} = -m\omega^2$ and $c''_{\text{m}} = 0$. The storage and loss stiffness corresponding to the complex stiffness of the nanoindentation-testing equipment, $c^*_{\text{f+t}}$, are obtained as (see, e.g., Findley et al. (1989))

$$c'_{\text{f+t}}(\omega) = \frac{c_{\text{f}} c_{\text{t}}(c_{\text{f}} + c_{\text{t}}) + D_{\text{t}}^2 c_{\text{f}} \omega^2}{(c_{\text{f}} + c_{\text{t}})^2 + D_{\text{t}}^2 \omega^2} \text{ and } c''_{\text{f+t}}(\omega) = \frac{(c_{\text{f}} + 2c_{\text{t}})c_{\text{f}} D_{\text{t}} \omega}{(c_{\text{f}} + c_{\text{t}})^2 + D_{\text{t}}^2 \omega^2} \tag{C.7}$$

Assuming the stiffness of the load frame to be much higher than the stiffness of the transducer, setting $c_{\text{f}} = \infty$, the storage and loss stiffness given in Equations (C.7) reduce to

$$c'_{\text{f+t}} = c_{\text{t}} \text{ and } c''_{\text{f+t}}(\omega) = D_{\text{t}}\omega \tag{C.8}$$

In the case of elastic material response and assuming a rigid indenter tip, the indentation modulus M appearing in Equation (C.1) for the contact stiffness S can be expressed by the bulk modulus K and the shear modulus μ_0, reading

$$M = \frac{E}{1 - \nu^2} = 4\mu_0 \frac{3K + \mu_0}{3K + 4\mu_0} \tag{C.9}$$

For $K = \infty$, $M = 4\mu_0$ representing the special case of incompressible material behavior. The complex contact stiffness representing the tip-sample interaction is obtained

by replacing the indentation modulus M in Equation (C.1) by the complex indentation modulus M^* of the viscoelastic model representing the material sample, reading for the case of incompressible materials

$$S^* = 2M^*\frac{\sqrt{A_\mathrm{c}}}{\sqrt{\pi}} = 8\mu^*\frac{\sqrt{A_\mathrm{c}}}{\sqrt{\pi}} \tag{C.10}$$

with the storage and loss stiffness given as

$$S' = 8\mu'\frac{\sqrt{A_\mathrm{c}}}{\sqrt{\pi}} \text{ and } S'' = 8\mu''\frac{\sqrt{A_\mathrm{c}}}{\sqrt{\pi}} \tag{C.11}$$

Finally, the storage and loss stiffness of the whole mechanical model are given by

$$c'_\mathrm{total}(\omega) = 8\sqrt{\frac{A_\mathrm{c}}{\pi}}\mu'(\omega) - m\omega^2 + c_\mathrm{t} \text{ and } c''_\mathrm{total}(\omega) = 8\sqrt{\frac{A_\mathrm{c}}{\pi}}\mu''(\omega) + D_\mathrm{t}\omega \tag{C.12}$$

In order to identify the underlying rheological model describing the time-dependent behavior of the material sample and, finally, to identify the respective model parameters, the complex moduli for different viscoelastic models are determined from the Laplace–Carson transformation of the creep-compliance function $J(t)$ and provided in Tables C.1 and C.2.

Table C.1: Creep-compliance function for different viscoelastic models.

Model	Creep-compliance function $J(t)$
Spring	$1/\mu_0$
Dash-pot	t/η
Maxwell	$1/\mu_0 + t/\eta$
Kelvin–Voigt	$1/\mu_0(1 - \exp(-\mu_0 t/\eta))$
Burgers	$1/\mu_0 + 1/\mu_\mathrm{v}(1 - \exp(-\mu_\mathrm{v} t/\eta_\mathrm{v})) + t/\eta$
Fractional dash-pot	$J_\mathrm{a}(t/\tau)^k$
Power law	$J_0 + J_\mathrm{a}(t/\tau)^k$

Table C.2: Storage and loss moduli for viscoelastic models listed in Table C.1.

Model	Storage modulus μ'	Loss modulus μ''
Spring	μ_0	0
Dash-pot	0	$\eta\omega$
Maxwell	$\dfrac{\eta^2\omega^2/\mu_0}{1+\eta^2\omega^2/\mu_0^2}$	$\dfrac{\eta\omega}{1+\eta^2\omega^2/\mu_0^2}$
Kelvin–Voigt	μ_0	$\eta\omega$
Burgers*	$\dfrac{p_1q_1\omega^2 - q_2\omega^2(1-p_2\omega^2)}{p_1^2\omega^2+(1-p_2\omega^2)^2}$	$\dfrac{p_1q_2\omega^3 + q_1\omega(1-p_2\omega^2)}{p_1^2\omega^2+(1-p_2\omega^2)^2}$
Fractional dash-pot	$\dfrac{1}{J_a}\dfrac{\omega^k}{\Gamma(1+k)}\cos\left(\dfrac{k\pi}{2}\right)$	$\dfrac{1}{J_a}\dfrac{\omega^k}{\Gamma(1+k)}\sin\left(\dfrac{k\pi}{2}\right)$
Power law	$\dfrac{J_0 + J_a\Gamma(1+k)\omega^{-k}\cos(\frac{k\pi}{2})}{J_0^2 + 2J_0J_a\Gamma(1+k)\omega^{-k}\cos(\frac{k\pi}{2}) + J_a^2\Gamma^2(1+k)\omega^{-2m}}$	$\dfrac{J_a\Gamma(1+k)\omega^{-k}\sin(\frac{k\pi}{2})}{J_0^2 + 2J_0J_a\Gamma(1+k)\omega^{-k}\cos(\frac{k\pi}{2}) + J_a^2\Gamma^2(1+k)\omega^{-2k}}$

*$p_1 = \eta/\mu_0 + \eta/\mu_v + \eta_v/\mu_v$, $p_2 = (\eta\eta_v)/(\mu_0\mu_v)$, $q_1 = \eta$, $q_2 = (\eta\eta_v)/\mu_v$

The still unknown model parameters describing the viscoelastic behavior of the material sample are determined from the experimentally obtained complex stiffness c^*_{total} and the phase angle ϕ, both being a function of the pre-specified angular frequencies ω, according to the procedure outlined in Figure C.3.

Remark 1: The change of the contact area A_c in time was not considered. Since the penetration amplitude corresponding to the oscillating part of the load history, $P_0 \sin(\omega t)$, is in the range of only a few nanometers (commonly 1–3 nm), the variation of the contact area is negligible.

Remark 2: The creep deformation associated with the constant part of the load history, $\bar{P}$, on the other hand, results in a continuous increase of the contact area. During the nanoindentation test, the contact area is computed as a mean value over several load cycles. If the material shows asymptotic creep (as in case of the polymer considered in this paper) and the number of load cycles considered for determination of c^*_{total} and ϕ is small, the influence of the creep deformation associated with $\bar{P}$ can be neglected. However, one should keep in mind that, especially for small penetrations, the change of the contact area may influence the identified model parameters.

C.3   Materials and experimental program

In this study, low-density polyethylene (LDPE), with its Young's modulus ranging from 0.139 to 0.35 GPa (see, e.g., matweb (2007)), and a Poisson's ration of 0.39 is considered. Nanoindentation tests were conducted at room temperature using a Hysitron Triboindenter nanoindenter with a three-sided Berkovich diamond tip and a cono-spherical tip with a nominal tip radius of 5 μm. The area functions for both tip shapes were obtained by the standard calibration procedure outlined in Oliver and Pharr (1992) using fused quartz (FQ) as calibration material. All tests were performed in the nanoDMA$^©$ module, where the tip is loaded by a constant load $\bar{P}$ and a cyclic load at a predefined frequency, with $P = \bar{P} + P_0 \sin(\omega t)$. Tests were conducted for frequencies ranging from 15 to 170 Hz. For each frequency, c^*_{total} and ϕ are computed from 100 load cycles. In addition to the frequency and the amplitude P_0, $\bar{P}$ was varied in the experimental program (see Table C.3). For each $(\bar{P}, P_0)$-pair, nine indents were performed.

Table C.3: Constant and oscillating part of load histories considered in the experimental program

Tip	$\bar{P}/P_0$ [μN]					
Berkovich	5/0.2	10/0.2	20/0.2	50/1.0	100/2	200/5
Cono-spherical	5/0.2	10/0.2	20/0.2	–	–	–

1. Determine c'_{total} and c''_{total} using Equations (C.3) and (C.4) for the considered frequencies ω_{i}, reading

$$c'_{\text{total}}(\omega_{\text{i}}) = |c^*_{\text{total}}(\omega_{\text{i}})| \cos \phi(\omega) \text{ and } c''_{\text{total}}(\omega_{\text{i}}) = |c^*_{\text{total}}(\omega_{\text{i}})| \sin \phi(\omega) \quad \text{(C.13)}$$

2. Compute storage and loss shear moduli of the material sample from Equations (C.12) as

$$\mu'_{\text{exp}}(\omega_{\text{i}}) = \frac{1}{8}\sqrt{\frac{\pi}{A_{\text{c}}}} \left[c'_{\text{total}}(\omega_{\text{i}}) + m\omega_{\text{i}}^2 - c_{\text{t}} \right] \text{ and}$$

$$\mu''_{\text{exp}}(\omega_{\text{i}}) = \frac{1}{8}\sqrt{\frac{\pi}{A_{\text{c}}}} \left[c''_{\text{total}}(\omega_{\text{i}}) - D_{\text{t}}\omega_{\text{i}} \right] \quad \text{(C.14)}$$

Hereby, the parameters m, c_{t}, and D_{t} are obtained from the calibration of the system. The contact area A_{c} is computed from the contact height h_{c}, with $h_{\text{c}} = h - 0.75\bar{P}/S'$.

3. Identify the parameters for the chosen viscoelastic model by minimizing the error between the experimentally-obtained shear moduli (Equations (C.14)) and the expressions for the viscoelastic models given in Table C.2, with the model parameters as unknowns. For the case of the fractional dash-pot model, the error

$$R = \frac{e(J_{\text{a}}, k)}{u} \quad \text{(C.15)}$$

with

$$e^2(J_{\text{a}}, k) = \sum_{i=1}^{n} \left[(\mu'_{\text{exp}}(\omega_{\text{i}}) - \mu'_{\text{model}}(J_{\text{a}}, k, \omega_{\text{i}}))^2 \right.$$

$$\left. + (\mu''_{\text{exp}}(\omega_{\text{i}}) - \mu''_{\text{model}}(J_{\text{a}}, k, \omega_{\text{i}}))^2 \right] \quad \text{(C.16)}$$

and

$$u^2 = \sum_{i=1}^{n} \left[\mu'_{\text{exp}}(\omega_{\text{i}})^2 + (\mu''_{\text{exp}}(\omega_{\text{i}})^2 \right] \quad \text{(C.17)}$$

is minimized during identification of model parameters, where n is the number of different frequencies considered in the nanoindentation-testing program. In Equations (C.15) and (C.16), J_{a} is the initial creep compliance and k is the creep exponent of the fractional dash-pot model, with $0 \leq k \leq 1$.

Figure C.3: Flowchart for identification of model parameters from cyclic nanoindentation tests.

C.4   Results and discussion

Figures C.4 and C.5 show the mean values of the storage and loss shear moduli, μ'_{exp} and μ''_{exp}, obtained from cyclic nanoindentation testing for different frequencies and different values of $\bar{P}$. For the Berkovich tip, both the mean values and the standard deviation
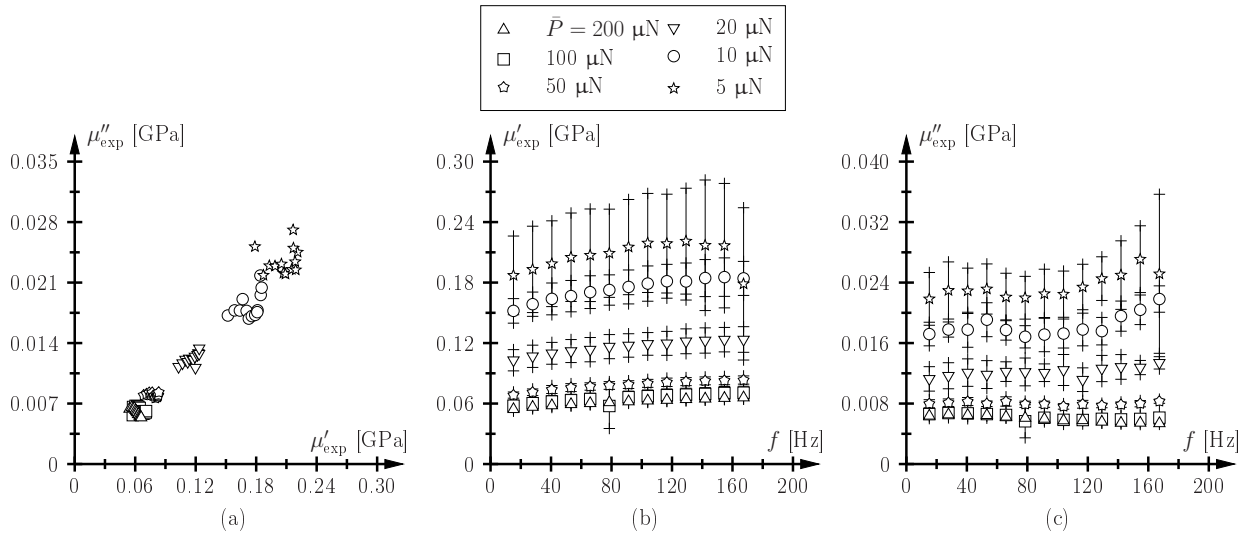

Figure C.4: (a) Cole–Cole diagram, mean values and standard deviation for (b) storage modulus μ'_{exp} and (c) loss modulus μ''_{exp} as a function of frequency for different values of $\bar{P}$ (Berkovich tip).
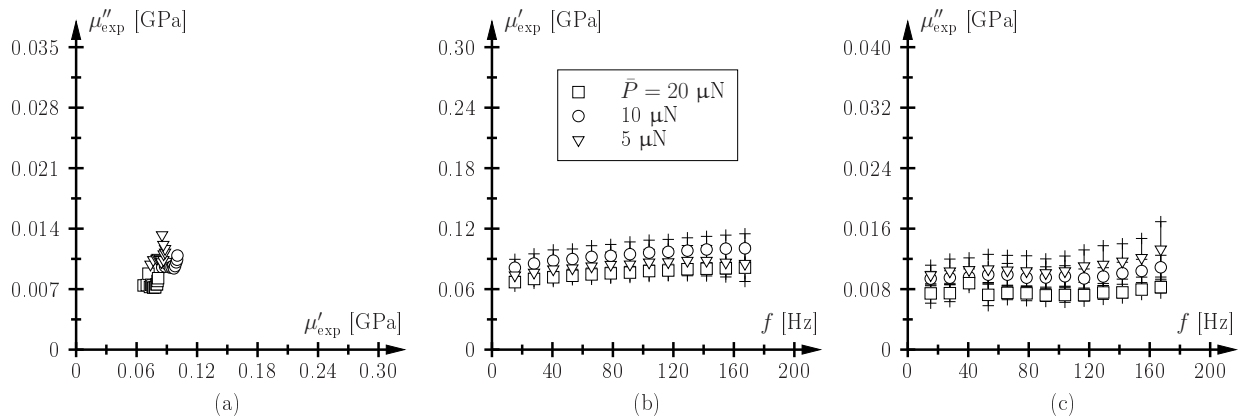
Figure C.5: (a) Cole–Cole diagram, mean values and standard deviation for (b) storage modulus μ'_{exp} and (c) loss modulus μ''_{exp} as a function of frequency for different values of $\bar{P}$ (cono-spherical tip).

of the storage and loss modulus decrease with increasing load. The same trend of the material parameters for an increased load $\bar{P}$ and, consequently, an increased penetration was observed during nanoindentation (static) creep tests. This behavior may be explained by the microstructure of LDPE, characterized by crystals with a lamellar thickness in

the order of 10 nm embedded in an amorphous phase (Cheremisinoff 1989). Thus, with increasing penetration, the effective material behavior is measured and the influence of the LDPE microstructure decreases. The results obtained from cyclic testing with the cono-spherical tip show the same dependence of the material parameters on the penetration.

The viscoelastic behavior of LDPE is described by a fractional dash-pot, which was already employed in Jäger and Lackner (2007) for parameter identification from nanoindentation (static) creep tests. For each set of nine indents, the parameters for the fractional dash-pot, the initial creep compliance J_a and the creep exponent k, were determined and mean values for both parameters were computed. Figure C.6 shows a comparison between the experimental results and the respective model response for the storage and loss modulus, μ' and μ'', as a function of the cyclic frequency f. The good agreement between the

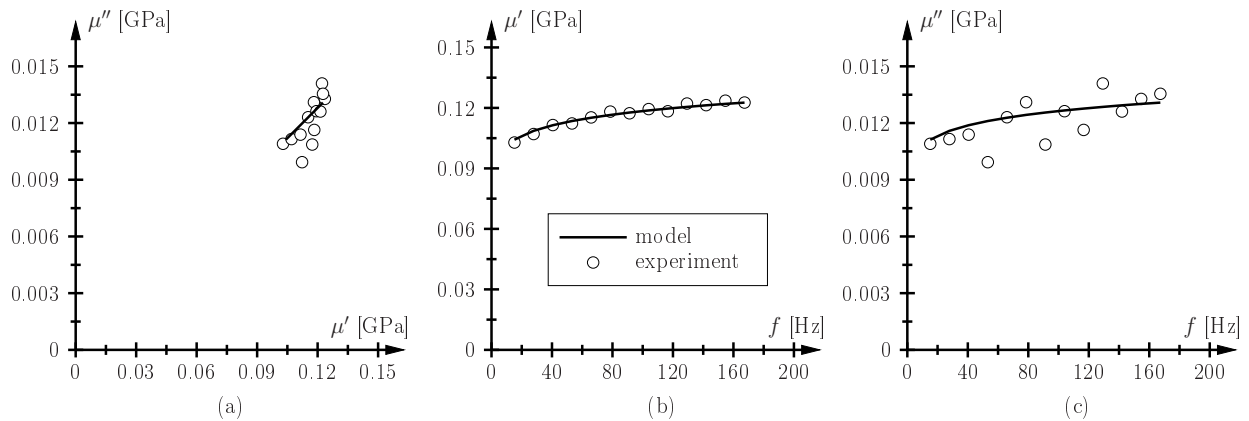Figure C.6: Comparison of experimental results and model response obtained from parameter identification: (a) Cole–Cole diagram, (b) storage modulus μ', and (c) loss modulus μ'' (experimental data for $\bar{P} = 20$ µN and $P_0 = 0.2$ µN).

experimental results and the model response for the storage and loss modulus confirms the proper choice of the fractional dash-pot for representing the viscoelastic response of LDPE.

In order to assess the results obtained from cyclic testing, the identified model parameters are compared with data from static creep tests. As regards the latter, parameter identification from nanoindentation (static) creep tests is based on the measured increase of penetration during the so-called holding phase of the measured penetration history (Jäger et al. 2007a,b) (see Figure C.7(a)). In case of materials showing – in addition to viscoelastic – also plastic material response, the plastic deformation might be considered by the application of the so-called double-indentation technique (Jäger and Lackner 2007). Hereby, the effect of plastic deformation is determined by adapting the experimental set-up (change of load history, see Figure C.7(b)) and considered in the employed parameter identification scheme. For a detailed description of both methods, the reader is referred to Jäger et al. (2007a) and Jäger and Lackner (2007).
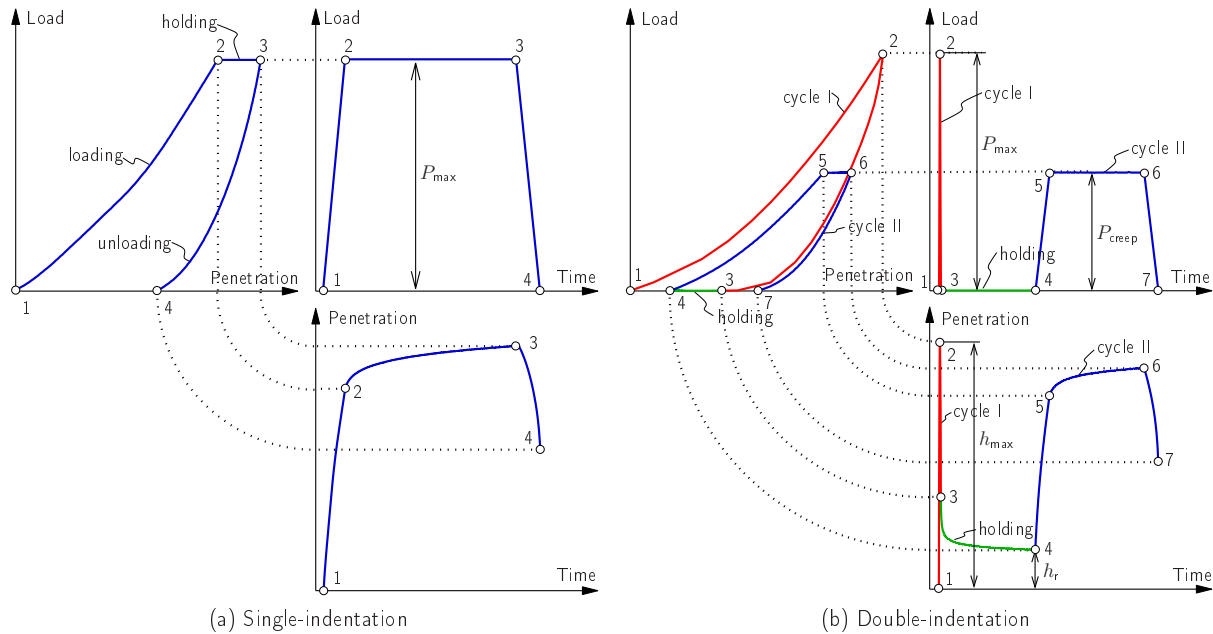
Figure C.7: Load–penetration curve, load history, and penetration history for (a) single-indentation test and (b) double-indentation test on material exhibiting elastic, viscous, and plastic material response (Jäger and Lackner 2007).

Figure C.8 shows the mean values of the identified model parameters for LDPE as a function of the maximum penetration, for both static creep tests (single- and double-indentation technique, see Jäger and Lackner (2007)) and cyclic testing using both tip shapes. As regards the results obtained by the Berkovich tip, both the single- and double-indentation technique reveal a similar load dependence of J_a and k, reaching a constant value of both parameters as the maximum load increases. This load dependence highlights again the influence of the LDPE microstructure on the measured material behavior. Comparing the obtained parameters, the single-indentation technique is found to overestimate the initial creep compliance, which is explained by the occurrence of plastic deformation assigned to the viscoelastic behavior during parameter identification. The creep exponent, on the other hand, is approximately the same for both techniques.

The creep tests conducted with the cono-spherical tip give only reliable results for small penetration depth (Jäger and Lackner 2007). The approximation of the tip shape in the employed parameter-identification scheme is not able to describe the complex tip shape for higher penetration depth. Hence, only tests conducted with small loads, characterized by a maximum penetration of about 150 nm, give reliable results.

The mean values of the fractional dash-pot parameters determined by cyclic testing are in good agreement with the parameters determined from the nanoindentation (static) creep tests. As regards the Berkovich tip, the same increase of the initial creep compliance J_a with increasing penetration was found. Also the values for the creep exponent k
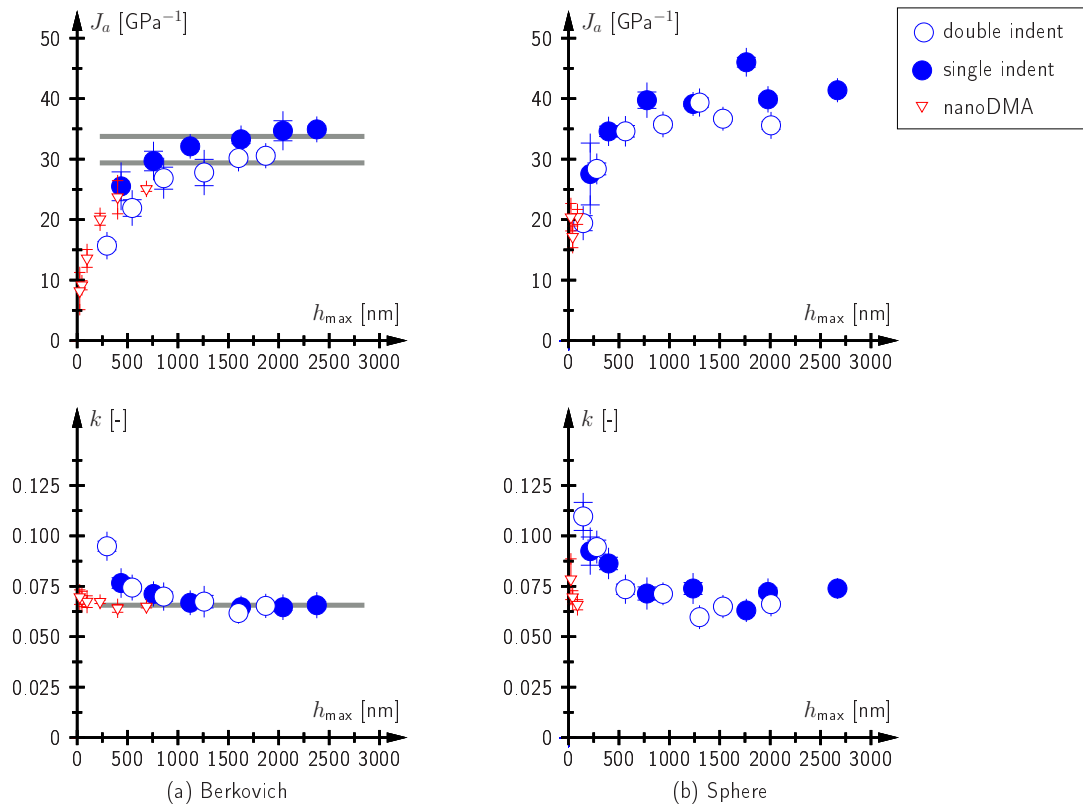
Figure C.8: Fractional dash-pot parameters for LDPE obtained from cyclic nanoindentation testing compared with parameters determined via single- and double-indentation testing using (a) a Berkovich tip and (b) a conospherical tip for different values of h_{max}.

correspond well for all three methods.

In order to assess the identified model parameters, the creep-compliance function $J(t)$ for the fractional dash-pot (see Table C.1) is plotted using the parameters obtained from different techniques and penetration depths (see Figure C.9) and compared with the creep-compliance function obtained from bending-beam-rheometer tests (Jäger and Lackner 2007). The creep-compliance function corresponding to the model parameters identified via the single-indentation technique slightly overestimates the macroscopic test results. This effect is explained by the plastic deformations occurring during the loading phase, which are not taken into account during parameter identification. The results obtained from double indentation, on the other hand, agree well with the bending-beam-rheometer test results, approaching the macroscopic creep compliance with increasing penetration. The creep-compliance functions identified via cyclic testing, corresponding to the different load levels, show the same increase of the compliance with increasing penetration, highlighting the influence of the LDPE microstructure on the mechanical behavior.
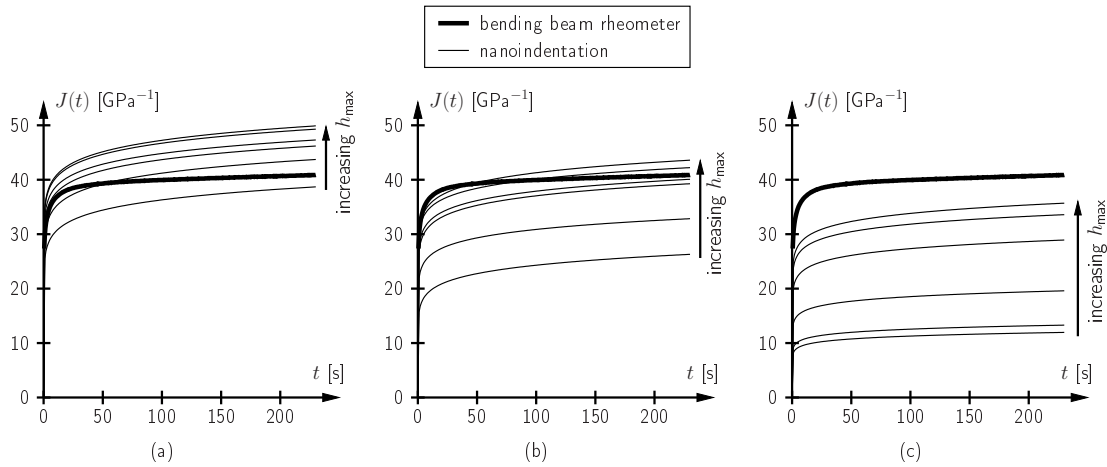
Figure C.9: Creep-compliance function for LDPE using model parameters iden-
tified by nanoindentation testing using the Berkovich tip and different
maximum loads compared with the creep-compliance function obtained
from bending-beam-rheometer tests: (a) Single-indentation technique, (b)
double-indentation technique, and (c) cyclic testing.

C.5   Summary and conclusions

The identification of viscoelastic model parameters from cyclic nanoindentation tests was
dealt with in this paper. Results from cyclic testing of low-density polyethylene (LDPE)
using a Berkovich and a cono-spherical tip were presented. The parameters for the
fractional dash-pot, describing the viscoelastic behavior of LDPE, were identified from
back-calculation using the measured complex shear modulus. The obtained results are
compared with parameters obtained from nanoindentation (static) creep tests using the
single- and double-indentation technique. Furthermore, the creep-compliance function
$J(t)$ of the fractional dash-pot corresponding to the parameters obtained from the dif-
ferent techniques was assessed by the creep-compliance function obtained from bending-
beam-rheometer tests (Jäger and Lackner 2007). Based on the so-obtained results, the
following conclusions can be drawn:

1. The fractional dash-pot is well suited for the description of the viscoelastic behavior
   of LDPE over the frequency range considered in the experimental program.

2. The model parameters obtained from cyclic testing agree well with the parameters
   identified by nanoindentation (static) creep tests using the double-indentation tech-
   nique. The model parameter representing the initial creep compliance obtained from
   single-indentation tests, on the other hand, slightly overestimates the creep com-
   pliance obtained from the other two methods. This was explained by the effect of
   plastic deformation, which is not taken into account during parameter identification
   within the single-indentation technique.

3. The creep-compliance function computed using the obtained model parameters increased for all three methods with increasing penetration, showing the influence of the LDPE microstructure and, thus, the length scale of testing, on the identified model parameters. The parameters determined via single indentation lead to a creep-compliance function overestimating the creep-compliance function obtained from bending-beam-rheometer tests. The creep-compliance function corresponding to the parameters identified via double indentation and cyclic testing, on the other hand, showed good agreement with the macroscopic properties, approaching the macroscopic creep-compliance function with increasing penetration. This result underlines the good performance of the latter two methods.

In summary, cyclic testing was found to be appropriate for the identification of viscoelastic model parameters and the obtained results are in good agreement with the parameters obtained from nanoindentation (static) creep tests.

Publication D

Microscale characterization of bitumen – back-analysis of viscoelastic properties by means of nanoindentation (Jäger et al. 2007b)

Authored by Andreas Jäger, Roman Lackner, and Klaus Stangl
Published in *International Journal of Materials Research*, Volume 98(5), pages 404–413

In order to understand the complex thermo-rheological behavior of asphalt, stemming from the viscoelastic nature of bitumen, the nanoindentation (NI) technique is employed. Hereby, the load history applied onto the indenter tip is characterized by a loading, holding, and unloading phase. As regards the identification of viscoelastic properties, a recently published back-analysis scheme, employing the holding phase of the NI test, is extended towards fractional-creep models. In fact, this type of models is found to perfectly describe the viscoelastic behavior of bitumen. Based on the identified viscoelastic model parameters, the influence of loading rate, maximum load, and temperature on these parameters is investigated. Hereby, the temperature dependence of creep parameters follows an Arrhenius-type law. In addition to the model parameters, application of the so-called grid-indentation technique within NI testing provides insight into the bitumen microstructure and the mechanical behavior of the different bitumen phases. The obtained results indicate the existence of a string-like microstructure embedded into a less viscous matrix material.

D.1 Introduction

Bitumen is the binder material of asphalt and determines its complex thermo-rheological behavior. E.g., the low viscosity of asphalt at high temperatures ($T > 135$ °C) is a necessary prerequisite for the construction and compaction process of high-quality asphalt layers. However, when the surface temperature reaches 70 °C during hot summer periods, this viscosity should be significantly higher in order to minimize the development of permanent deformations in asphalt pavements (rutting). The desirable increase of viscosity and, hence, increase of stiffness from hot to medium temperatures ($0 < T < 70$ °C) are, on the other hand, disadvantageous at low temperatures ($T < 0$ °C), causing low-temperature cracking in asphalt pavements.

In general, the viscosity of bitumen can be described by a linear function in the log(viscosity)–temperature diagram (see Figure D.1). This relation may be optimized with respect to
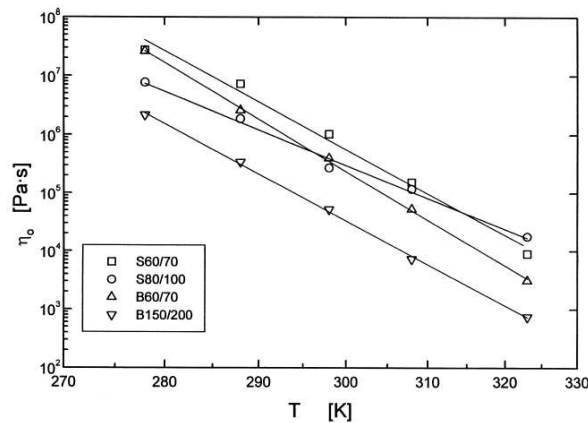

Figure D.1: Temperature dependence of the zero-shear-rate limiting viscosity for different types of bitumen (Partal et al. 1999).

climate conditions and expected traffic load by the proper choice of the crude oil used in the bitumen production process and the so-called cut-point, defining the temperature during vacuum distillation. The goal of this optimization process is threefold:

1. Maintain low viscosities at high temperatures for construction and compaction;

2. Ensure high viscosity and elastic behavior at medium temperatures to avoid rutting; and

3. Ability of stress relaxation (sufficient small viscosity) at low temperatures.

In order to determine the origin of the viscoelastic behavior of bitumen, use of nanoindentation is proposed in this paper. In contrast to macroscopic tests, nanoindentation (NI) gives access to the mechanical properties and the microstructure at small length

scales. In this paper, the mechanical properties obtained from NI testing are combined with chemical-test results and images from environmental scanning electron microscopy (ESEM), giving new insights into the complex thermo-rheological nature of bitumen.

D.2 Methods – nanoindentation

The main goal of NI is the identification of mechanical properties of the indented material. During NI measurements, a tip with defined shape penetrates the specimen surface with the indentation load P [N] and the penetration h [m] recorded as a function of time. Commonly, each indent consists of a loading, holding, and unloading phase (see Figure D.2). During standard interpretation of NI test results, the hardness and the elastic
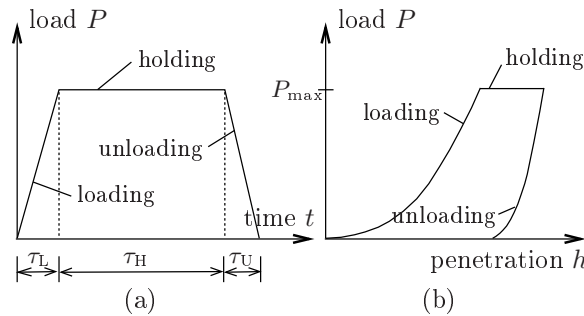

Figure D.2: Illustration of (a) load history and (b) load–penetration curve of NI tests.

material properties are determined:

- The hardness of the material, defined as $H = P_{\max}/A_c$ [Pa], is obtained from the loading phase of the NI test. Hereby, $P_{\max}$ [N] denotes the applied maximum load, and A_c [m^2] is the horizontal projection of the contact area at the end of the loading phase.

- According to Sneddon (1965) and Oliver and Pharr (1992), the Young's modulus E of elastic or elastoplastic materials can be obtained from the relation between the measured initial slope of the unloading curve $S = \mathrm{d}P/\mathrm{d}h|_{h=h_{\max}}$ and the indentation modulus $M = E/(1 - \nu^2)$, reading

$$S = \frac{2}{\sqrt{\pi}} M \sqrt{A_c} \qquad \text{(D.1)}$$

where ν is the Poisson's ratio, and A_c is the projected area of contact.

Parameter identification of materials exhibiting, in addition to elastic and plastic material response, time-dependent behavior (e.g., polymers, bitumen, . . .) requires back-analysis of

the parameters from the holding phase of the measured penetration history $h(t)$. Recently, analytical solutions for the indentation of rigid tips into a viscoelastic halfspace were reported for spherical tips (Cheng et al. 2005) and for perfect conical tips (Vandamme and Ulm 2006).

Since the shape of indenter tips varies in consequence of the production process and in the course of testing due to attrition, the solution for the tip penetration, taking into account the real indenter shape, outlined in Jäger et al. (2007a), is considered. Hereby, the geometrical representation of the indenter shape (with $A_{\text{tip}} = C_0 f(\rho)^2$ for perfect conical tips) is extended to

$$A_{\text{tip}} = \rho^2 \pi = C_0 f(\rho)^2 + C_1 f(\rho) \tag{D.2}$$

where A_{tip} [m^2] is the area of the cross section, and ρ [m] and $f(\rho)$ [m] are the corresponding radius and distance from the apex of the axisymmetric tip, respectively (see Figure D.3). C_0 [-] and C_1 [m] are constants describing the tip shape, which are generally
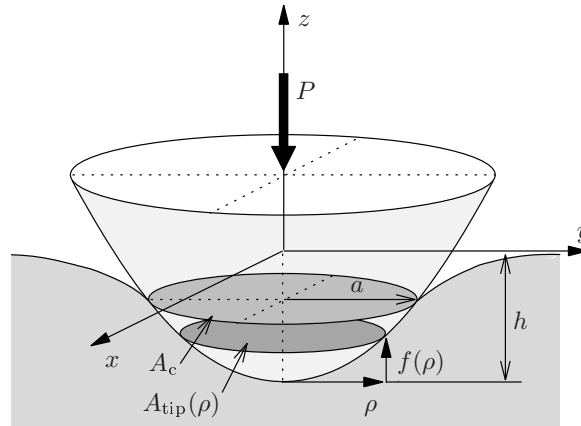

Figure D.3: Contact between a rigid axisymmetric indenter of shape $f(\rho)$ and an infinite halfspace (P is the applied load, h is the penetration, and a is the contact radius).

provided during calibration of the NI equipment.

Based on the solution for the elastic indentation problem for the tip shape given in Equation (D.2), the viscoelastic solution is obtained by the application of the method of functional equations (Lee and Radok 1960) (see Appendix D.6.1). For the identification of viscoelastic model parameters of bitumen, this solution is specialized to two rheological models describing fractional creep: i.e., the nonlinear dash-pot (nlDP) and power-law (PL) creep model (see Figure D.4). The deviatoric creep compliance of both models reads

$$J_{\text{nlDP}} = J_a \left(t/\bar{\tau} \right)^k \tag{D.3}$$

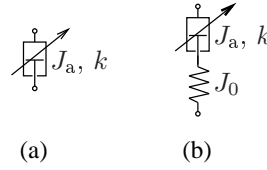$$J_{\text{PL}} = J_0 + J_a \left(t/\bar{\tau} \right)^k \tag{D.4}$$

Figure D.4: Creep models considered for back-analysis of viscoelastic parameters for bitumen: (a) Nonlinear dash-pot (nlDP) model and (b) power-law (PL) model.

where J_0 [GPa^{-1}] is the initial creep compliance describing the elastic behavior, J_a [GPa^{-1}] and k [-] characterize the time dependent behavior. $\bar{\tau}$ [s] is introduced for dimensional reasons and is set equal to 1 s.

In order to determine material parameters from NI test data, the error between the experimentally obtained function $F_{exp}(a)$ (depending on the contact radius a and determined from the penetration history $h(t)$ using Equations (D.10) and (D.12), see Appendix D.6.1) and the analytical result given in Equation (D.28) is minimized within the holding period by adapting the unknown model parameters (see Figure D.5). For the case of the nlDP
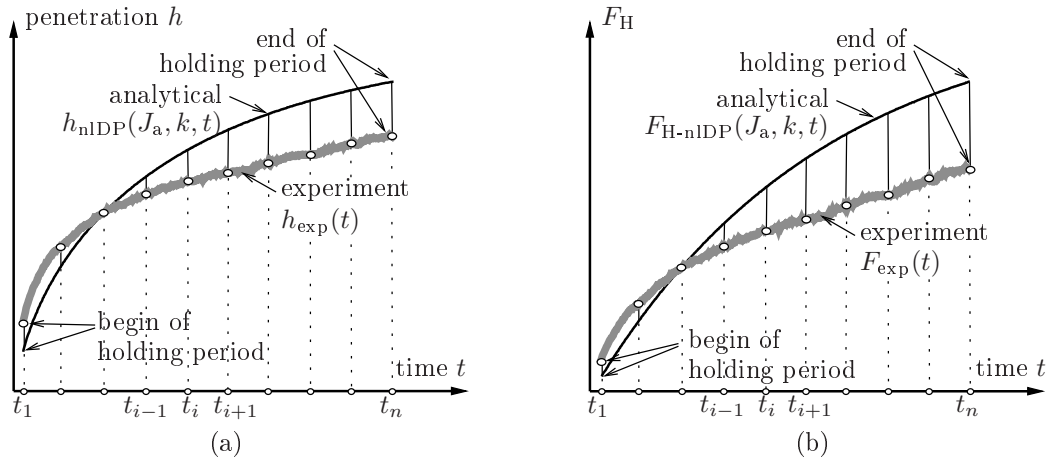

Figure D.5: Illustration of definition of the error used for parameter identification from the holding period of NI test data for the nlDP model: (a) Penetration history $h(t)$ and (b) evolution function F within the holding period.

model, the mentioned error is defined by

$$R_{nlDP}(J_a, k) = \frac{e(J_a, k)}{u} \tag{D.5}$$

with

$$e^2(J_a, k) = \sum_{i=1}^{n} [F_{exp}\{a[h(t_i)]\} - F_{H\text{-}nlDP}(J_a, k, t_i)]^2 \tag{D.6}$$

$$u^2 = \sum_{i=1}^{n} F_{\exp}^2(t_i) \tag{D.7}$$

where n is the number of selected time instants of the holding phase. The error given in Equation (D.5) is minimized by adapting the unknown model parameters J_a and k using a simplex iteration (Press et al. 1996).

D.3   Materials and experimental setup

Three types of bitumen, two plain bitumen (B50/70 and B50/70M4) and one polymer-modified bitumen (PmB60/90), are considered (the given numbers indicate the range of penetration (ÖNORM EN 1426 2000)). The polymer modified bitumen was obtained by the allowance of styrene-butadiene-styrene to the aforementioned B50/70M4. Additionally, aging of B50/70M4 and PmB60/90 was performed by means of the rolling-thin-film-oven test (RTFOT) according to EN 12607-1 (1999) and, subsequently, by the pressure-aging vessel (PAV) according to prEN 14769 (2003). The conventional properties of all three unaged bitumen (denoted as "A") and the RTFOT and PAV-aged bitumen (denoted as "C") are listed in Table D.1. The result from elemental analysis is given in Table D.2.

Table D.1: Conventional properties of considered types of bitumen (A: original bitumen, C: RTFOT+PAV-aged) (parameters according to ÖNORM EN 1426 (2000); ÖNORM EN 1427 (2000); ÖNORM EN 12593 (2000)).

Bitumen	Penetration $[\frac{1}{10}$ mm]	Softening point [°C]	Fraaß breaking point [°C]
B50/70-A	49	50.5	-13
B50/70M4-A	54	48.8	-20
B50/70M4-C	27	64.8	-
PmB60/90-A	73	86.1	-28
PmB60/90-C	36	79.8	-

All NI tests were conducted using a Hysitron Triboindenter nanoindenter with a three-sided Berkovich diamond tip in a dry gas (nitrogen) environment, ensuring no water condensation on the sample surface for temperatures below the dew point. Calibration of the NI testing equipment revealed $C_0 = 24.5$ and $C_1 = 2314$ nm, describing the tip shape (see Equation (D.2)).

Table D.2: Elemental composition (in mass%) of considered types of bitumen (ASTM D5291 2002).

Bitumen	C	H	O	N	S	Σ
B50/70-A	83.0	10.4	-	1.1	5.1	99.6
B50/70M4-A	83.9	10.4	<0.1	0.4	5.0	99.7
B50/70M4-C	83.7	10.5	<0.1	0.5	4.9	99.6
PmB60/90-A	84.3	10.3	0.6	0.4	4.3	99.9
PmB60/90-C	84.0	10.2	0.9	0.5	4.4	100.0

D.4   Presentation of results and discussion

The presented parameter identification scheme was applied to the types of bitumen listed in Table D.1. For each type of bitumen, grid indentation (Constantinides et al. 2006) characterized by $10{\times}10$ indents was performed. Figure D.6 shows the frequency plots
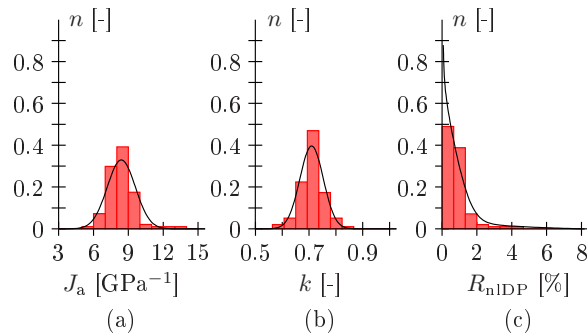

Figure D.6: Identification of model parameters for B50/70-A tested at -1 °C: Frequency plots for (a) J_a [GPa^{-1}], (b) k [-], and (c) error R_nlDP [%] (NI test conditions: P_max =20 µN, $\dot{P} = \mathrm{d}P/\mathrm{d}t$ =40 µNs^{-1}, τ_H =5 s).

for J_a, k, and the error R_nlDP for B50/70-A tested at -1 °C. The values for the error R_nlDP are less than 3 %, confirming the proper choice of the nlDP model for representing the viscoelastic response of bitumen. The obtained frequency plots for J_a and k are approximated by a Gaussian distribution, giving mean values and standard deviations for the model parameters. For the considered type of bitumen (B50/70-A), the mean values of the model parameters corresponding to $T = -1\,°\mathrm{C}$ are: $J_\mathrm{a} = 8.39$ GPa^{-1} and $k = 0.71$. In the following, the outlined mode of parameter identification is employed to study

- the influence of the loading rate and the maximum load on the identified parameters,

- the temperature dependence of the model parameters, and

- the microstructure and the mechanical properties of the different bitumen phases.

D.4.1   Influence of loading rate and maximum load

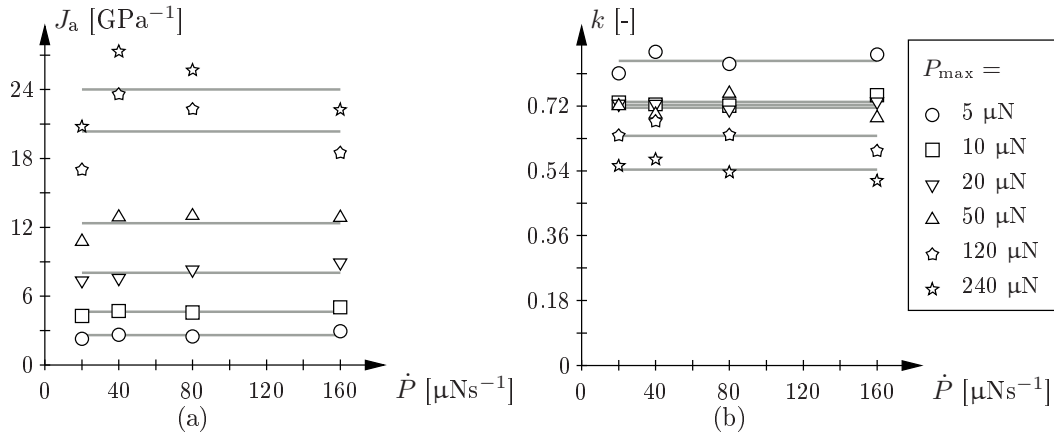Figure D.7 shows the mean values of the nlDP model parameters for different loading rates

Figure D.7: Influence of loading rate and maximum load on nlDP model parameters: Mean value of (a) J_a [GPa^{-1}] and (b) k [-] (bitumen B50/70-A tested at T =-1 °C; P_max =5, 10, 20, 50, 120, 240 μN; $\dot{P}$ = dP/dt =20, 40, 80, 160 μNs^{-1}; τ_H =5 s (for P_max = 10, 20 μN) and 10 s (for P_max = 5, 50, 120, 240 μN)).

and different values for the maximum load obtained from grid indentations on bitumen B50/70-A at -1 °C (with $\dot{P}$ = dP/dt =20, 40, 80, 160 μNs^{-1} and P_max =5, 10, 20, 50, 120, 240 μN). Whereas the influence of the loading rate on the parameters is quite small for all considered load levels, the maximum load itself has a high impact on the obtained model parameters (see Figure D.8). By increasing the maximum load, J_a increases until
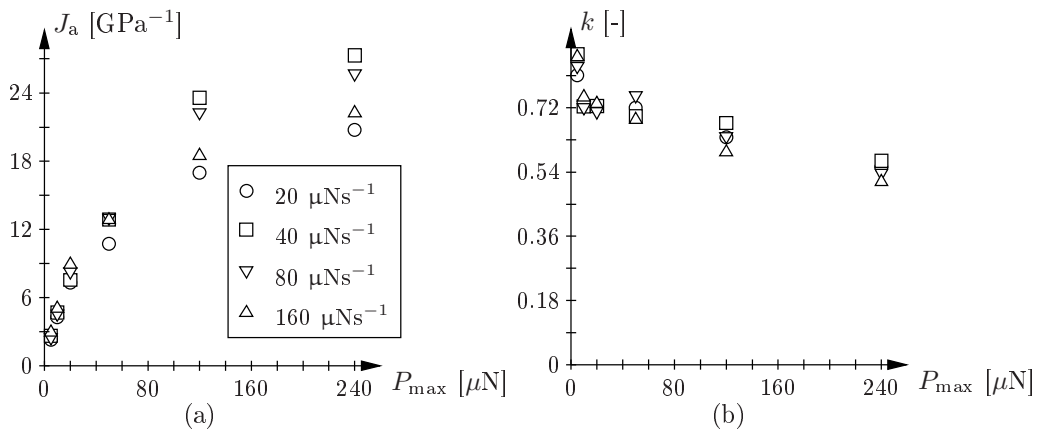

Figure D.8: Influence of maximum load on nlDP model parameters: Mean values for (a) J_a [GPa^{-1}] and (b) k [-] (bitumen B50/70-A tested at T =-1 °C; P_max =5, 10, 20, 50, 120, 240 μN; $\dot{P}$ = dP/dt =20, 40, 80, 160 μNs^{-1}; τ_H =5 s (for P_max = 10, 20 μN) and 10 s (for P_max =5, 50, 120, 240 μN)).

it seems to reach a limiting value. The parameter k, on the other hand, decreases almost continuously with increasing maximum load (see Figure D.8(b)). This variation of the identified model parameters with the maximum load and, consequently, with the penetration depth is explained by the bitumen microstructure, consisting of viscous strings embedded into a low-viscous matrix (see Subsection D.4.3)

The back-analysis scheme itself provides a unique solution during identification of J_a–k pairs corresponding to the different maximum loads. The identified J_a–k pairs corresponding to different maximum loads were used in the analytical solution for the penetration history given in Figure D.9. As the maxiumum load used for parameter identification increases, the variation in the penetration histories decreases, indicating the decreased influence of the bitumen microstructure as the penetration depths during parameter identification increase.
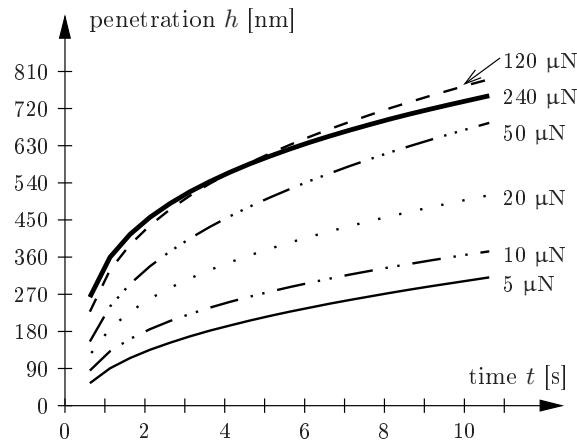

Figure D.9: Analytical solution for penetration history $h(t)$ for $P_{\max} = 50$ μN, $\dot{P} = 80$ μNs^{-1}, τ_H =10 s (given values refer to maximum load used in NI tests for parameter identification, leading to different J_a–k pairs).

D.4.2   Temperature dependence of model parameters

Accounting for the thermo-rheological behavior of bitumen, the influence of the temperature on model parameters is studied by conducting NI tests at different temperatures. Figures D.10(a) and (b) show mean values of the nlDP model parameters for bitumen B50/70-A tested at T =-4.5; -1; 2; 5.5; 9 °C. Whereas J_a increases from -4.5 to -1 °C, slightly decreases from -1 to 2 °C, and finally increases again from 2 to 9 °C, the parameter k increases continuously with increasing temperature. The temperature dependence of the parameter k is approximated by two lines, with the slope of the lines being different for temperatures below -1 °C and for temperatures above 2 °C (see Table D.3). The increase of both J_a and k indicate the expected increase of the creep compliance with increasing temperature. The change of the parameters between -1 and 2 °C might be related to
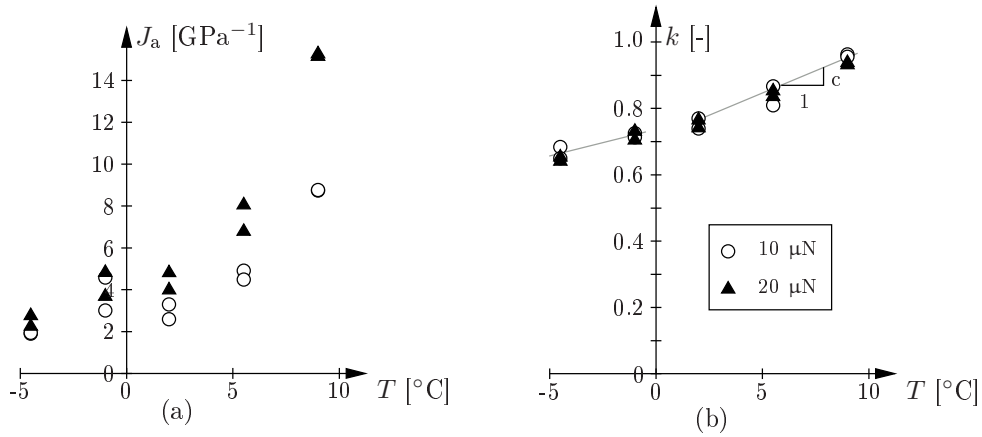
Figure D.10: Temperature dependence of nlDP model parameters for bitumen B50/70-A: Mean values for (a) J_a [GPa^{-1}] and (b) k [-] (NI test conditions: P_{max} =10, 20 µN, $\dot{P} = dP/dt$ =20, 40 µNs^{-1}, τ_H =10 s).

chemo-physical processes, observed during testing of bitumen by means of modulated differential scanning calorimetry, where an exothermic peak was found for B50/70-A at this temperature range (Jäger 2004).

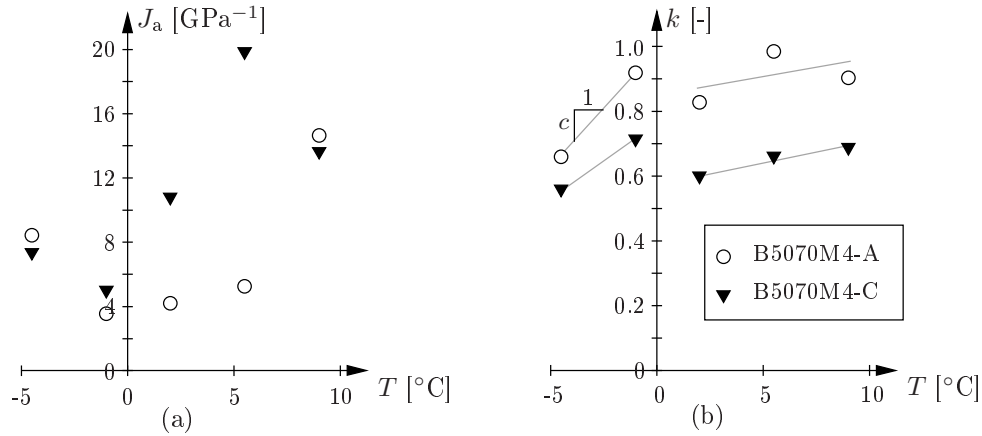Figures D.11 and D.12 show mean values of the nlDP model parameters for the bitumen

Figure D.11: Temperature dependence of nlDP model parameters for bitumen B50/70M4-A/ -C: Mean values for (a) J_a [GPa^{-1}] and (b) k [-] (NI test conditions: P_{max} =10 µN, $\dot{P} = dP/dt$ =20 µNs^{-1}, τ_H =10 s).

B50/70M4 and PmB60/90M4 (A- and C-aged) tested at T =-4.5; -1; 2; 5.5; 9 °C. As regards J_a, a decrease from -4.5 to -1 °C, followed by an increase from -1 to 9 °C was observed for both types of bitumen and aging states. The parameter k, on the other hand, increases from -4.5 to -1 °C, slightly decreases from -1 to 2 °C, and finally increases again from 2 to 9 °C (for the values of c, see Table D.3). As for the bitumen B50/70-A, the change of J_a between -4.5 and -1 °C and the change of k between -1 and 2 °C is assigned to
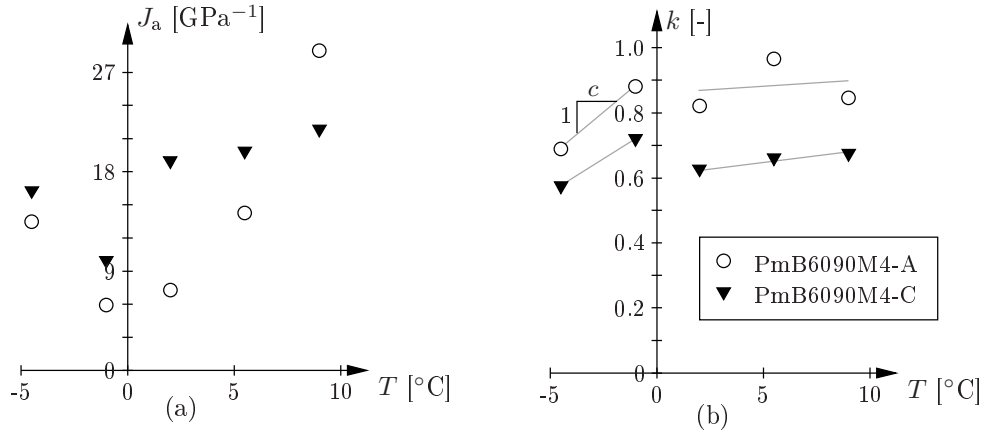
Figure D.12: Temperature dependence of nlDP model parameters for bitumen PmB60/90M4-A/ -C: Mean values for (a) J_a [GPa^{-1}] and (b) k [-] (NI test conditions: P_{max} =10 μN, $\dot{P} = dP/dt$ =20 μNs^{-1}, τ_H =10 s).

Table D.3: Ratio of the activation energy and the gas constant E_a/R, and slope c describing the temperature dependence of k for considered types of bitumen.

Bitumen	E_a/R [K]	c (-4.5 to -1 °C) [°C^{-1}]	c (2 to 9 °C) [°C^{-1}]
B50/70-A	13 000	0.018	0.028
B50/70M4-A	10 300	0.074	0.011
B50/70M4-C	6 700	0.044	0.013
PmB60/90-A	12 500	0.055	0.003
PmB60/90-C	5 400	0.041	0.007

changes in the molecular structure observed by means of modulated differential scanning calorimetry.

The temperature dependence of J_a depicted in Figures D.13 and D.14 is well-described by an Arrhenius-type law in the temperature regime outside the aforementioned rearrangement of molecules, reading:

$$J_a = \bar{J}_a(\bar{T}) \exp\left[-\frac{E_a}{R}\left(\frac{1}{T} - \frac{1}{\bar{T}}\right)\right] \tag{D.8}$$

where $\bar{T}$ [K] is the reference temperature, R [J mol^{-1}K^{-1}] is the gas constant, and E_a [J mol^{-1}] is the activation energy. The ratio of the activation energy and the gas constant, E_a/R, is given in Table D.3 for all considered types of bitumen. Interestingly, the activation energy for bitumen B50/70-A computed for the whole tested temperature range (dashed line in Figure D.13), with $E_a/R = 8\,500$ K, agrees very well with the value
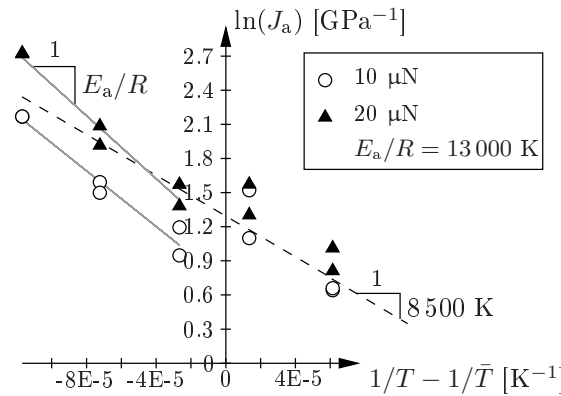
Figure D.13: Identification of Arrhenius-type law describing the temperature dependence of J_a [GPa^{-1}] for bitumen B50/70-A ($\bar{T} = 273$ K).
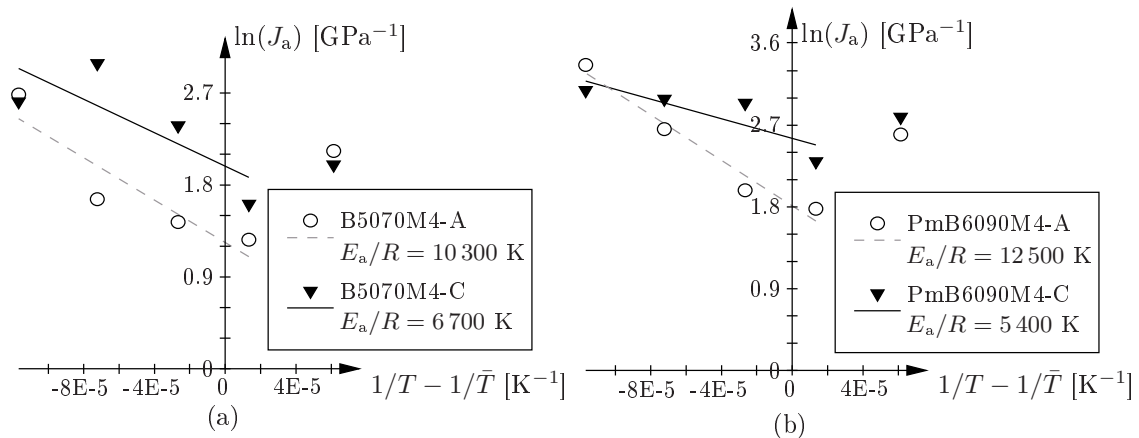

Figure D.14: Identification of Arrhenius-type law describing the temperature dependence of J_a [GPa^{-1}] for bitumen B50/70M4-A/-C and PmB60/90M4-A/-C ($\bar{T} = 273$ K).

obtained from macroscopic bending-beam-rheometer tests of bitumen, revealing a value of E_a/R of 9 000 K (Lackner et al. 2005).

Finally, the obtained values for J_a and k for bitumen B50/70-A were compared with the results obtained from standard bitumen tests, such as the bending beam rheometer (BBR) and the dynamic shear rheometer (DSR) operating in different temperature regimes. Figure D.15 shows a good agreement between the obtained parameters from NI and the respective standard-test data. The obtained NI data fit well into the larger temperature range covered by the standard test methods (-24 to 40 °C).

D.4.3   Bitumen treated as a multiphase composite

Bitumen is the remaining part during crude-oil distillation and, hence, its chemical composition strongly depends on the origin of the crude oil. Its main constituents are hy-
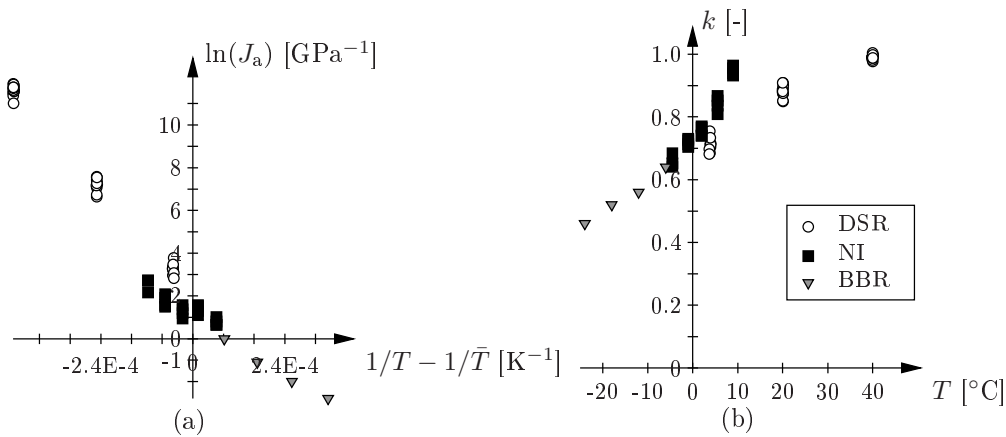
Figure D.15: Comparison of model parameters (a) J_a [GPa^{-1}] and (b) k [-] obtained from NI testing with DSR and BBR data for bitumen B50/70-A ($\bar{T} = 273$ K).

drocarbons with different amount of polarity, and a molecular mass ranging from 300 to 100 000 g/mol (Shell-Bitumen-U.K. 1990; Hobson 1984). This complex chemical composition results in an arrangement within the molecular cocktail in bitumen, characterized by a string-like structure embedded in a matrix substance (Rozeveld et al. 1997). Interestingly, the string-like structures change their properties with aging (see Figure D.16) (Stangl et al. 2006) and they align under external loading (Rozeveld et al. 1997).

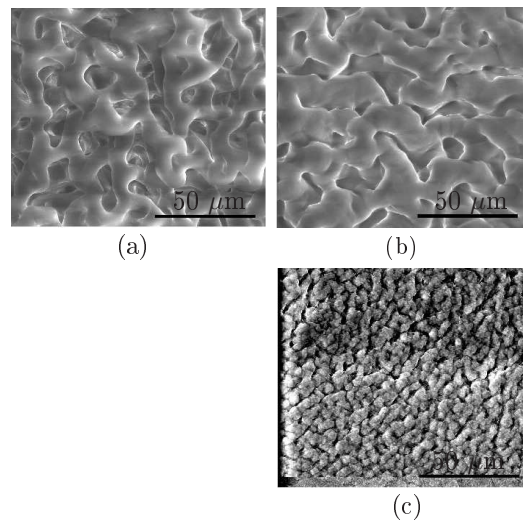Figure D.16: Environmental scanning electron microscopy (ESEM) images of (a) unaged, (b) RTFOT-aged, and (c) RTFOT+PAV-aged bitumen B50/70 (Stangl et al. 2006).

In order to identify the mechanical properties of the two bitumen phases, the grid indentation technique (Constantinides et al. 2006) is employed. With the characteristic dimension of the bitumen microstructure of 10 μm (diameter of strings according to Stangl et al.

(2006)), the distance between adjacent grid points is set to 5 μm. Using a Berkovich tip for the indentation experiments, the distance between adjacent indents of 5 μm gives a maximum penetration of 400 nm, ensuring no interaction between two adjacent indents (see Figure D.17).
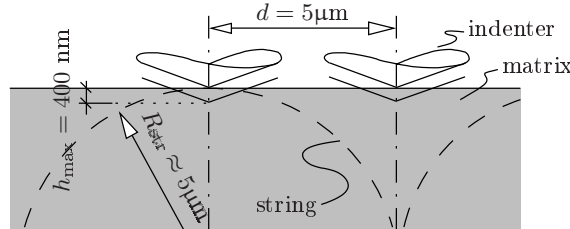
Figure D.17: Determination of appropriate distance between adjacent grid points from (i) bitumen microstructure and (ii) the maximum penetration depth.

Figure D.18 shows frequency plots and the corresponding grid plots for the parameters of
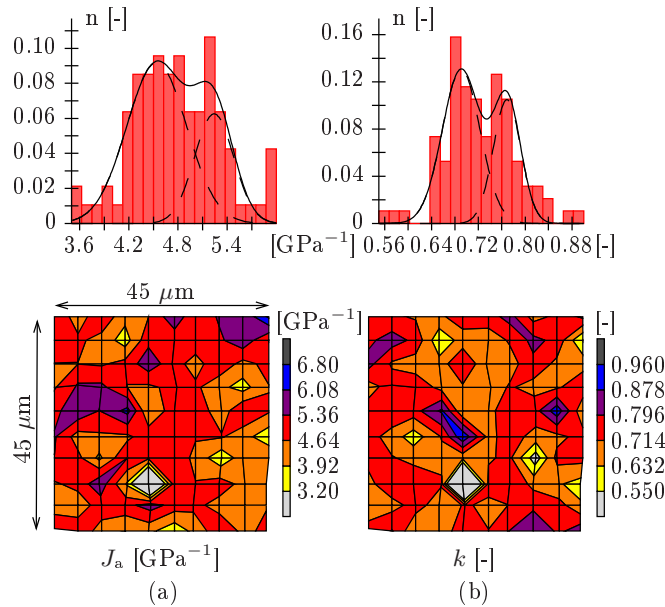
Figure D.18: Frequency plot and corresponding grid plot for parameters of nlDP model: (a) J_a [GPa^{-1}] and (b) k [-] (bitumen B50/70-A tested at T =-1 °C, P_{max}=10 μN, τ_L =0.25 s, τ_H =5 s).

the nlDP model obtained from grid indentation on B50/70-A tested at -1 °C. The grid plots confirm the microstructure already observed by ESEM (Rozeveld et al. 1997; Stangl et al. 2006), showing a string like microstructure with typical dimensions of about 10 μm embedded into a matrix material. The histograms emphasize the presence of two bitumen phases exhibiting different mechanical behavior. Whereas the strings show lower values of J_a and k, higher values for the matrix are observed. The approximation of the frequency

plots by two Gaussian distributions gives the mean values and the standard deviation of the model parameters for the two bitumen phases.

D.5   Concluding remarks

The identification of viscoelastic properties of bitumen and its material phases by means of nanoindentation was presented in this paper. Hereby, the back-analysis scheme proposed in Jäger et al. (2007a) was extended towards implementation of two fractional creep models, i.e., the nonlinear dash-pot and the power-law model. In order to identify the material parameters of bitumen and to validate the performance of the proposed analysis scheme, NI tests on different types of bitumen were performed for different loading rates, maximum loads, and at different temperatures. The parameters for the nlDP model were determined from the holding period of the obtained penetration histories. Based on the so-obtained parameters, the following conclusions can be drawn:

1. The increase of the maximum load resulted in a significant variation of the model parameters. This effect was attributed to the microstructure of bitumen present at the scale of NI testing.

2. The loading rate, on the other hand, showed marginal influence on the parameters, reflecting the ability of the presented parameter identification scheme to capture time-dependent material behavior.

3. The temperature dependence of the parameter J_a was successfully described by an Arrhenius-type law. The change of the bitumen microstructure, observed earlier by means of modulated differential scanning microscopy, was reflected by a variation of the model parameters in the respective temperature regime.

4. The model parameters obtained from NI testing fit well into results from standard test methods.

5. The results from grid indentation gave insight into the microstructure of bitumen showing the string-like structure already observed by environmental scanning electron microscopy. Hereby, the strings were described by lower values of the viscoelastic model parameters, whereas higher values for the matrix were observed.

The nonlinear dash-pot (nlDP) model employed for parameter identification gave excellent agreement between the experimentally-obtained NI penetration curves and the model response. According to bending-beam-rheometer tests the nlDP model is able to capture both, the short- as well as the long-term response of bitumen.

D.6 Appendix

D.6.1 Analytical solution for viscoelastic indentation problem – specialization for power-law model

D.6.1.1 Elastic indentation problem

For the solution of the elastic indentation problem, i.e., a rigid indenter penetrating the elastic halfspace (see Figure D.3), the so-called Sneddon solution (Sneddon 1965) is employed and specialized for the function $f(\rho)$ describing the tip shape, with

$$f(\rho) = \frac{1}{2C_0}\left(\sqrt{C_1^2 + 4C_0\rho^2\pi} - C_1\right) \tag{D.9}$$

Here, ρ [m] is the radius of the axisymmetric tip, and C_0 [-] and C_1 [m] are constants describing the tip shape. According to Jäger et al. (2007a), the penetration h [m] and the corresponding load P [N] are related through the contact radius a,

$$h = a\sqrt{\frac{\pi}{C_0}}\arctan\frac{2a\sqrt{C_0\pi}}{C_1} \tag{D.10}$$

$$
\begin{aligned}
P &= 4\pi\frac{E}{1-\nu^2}\frac{2a^3}{3C_1}\,{}_2F_1\left(1/2; 2; 5/2; -\frac{4a^2C_0\pi}{C_1^2}\right) \\
&= MF(a) \tag{D.11}
\end{aligned}
$$

where M is the indentation modulus, with $M = E/(1-\nu^2)$, and $F(a)$ is a function depending only on geometric properties, such as the tip shape (described by C_0 and C_1) and the contact radius a, reading

$$F(a) = 4\pi\frac{2a^3}{3C_1}\,{}_2F_1\left(1/2; 2; 5/2; -\frac{4a^2C_0\pi}{C_1^2}\right) \tag{D.12}$$

In Equations (D.11) and (D.12), ${}_2F_1(a; b; c; z)$ denotes a hypergeometric function, defined as (see, e.g., Abramowitz and Stegun (1972))

$$
{}_2F_1(a; b; c; z) = \frac{\Gamma(c)}{\Gamma(b)\Gamma(c-b)}\int_0^1\frac{t^{b-1}(1-t)^{c-b-1}}{(1-tz)^a}\mathrm{d}t \tag{D.13}
$$

D.6.1.2 Viscoelastic indentation problem – Consideration of trapezoidal load history

The elastic indentation problem outlined in the previous subsection is extended to linear viscoelasticity by the method of functional equations (Lee and Radok 1960). Following

the method of functional equations, the viscoelastic solution for the indentation problem is obtained from the elastic solution by replacing the elastic operators P, M, and $F(a)$ in Equation (D.11) by their Laplace transforms $\widehat{P(s)}$, $\widehat{M(s)}$, and $\widehat{F(a(s))}$, giving

$$\widehat{P(s)} = \widehat{M(s)}\widehat{F(a(s))} \tag{D.14}$$

Re-arrangement yields an expression for the Laplace transform of the function $F(a(s))$ as

$$\widehat{F(a(s))} = \frac{\widehat{P(s)}}{\widehat{M(s)}} = \frac{1}{s\widehat{M(s)}}s\widehat{P(s)} = \widehat{\bar{Y}(s)}s\widehat{P(s)} \tag{D.15}$$

where $1/(s\widehat{M(s)})$ was replaced by the Laplace transform of $\bar{Y}(t)$, in the following referred to as indentation compliance function. Considering that (i) a multiplication by s in the Laplace domain is equivalent to a derivation in the time domain and (ii) a multiplication of two Laplace-transformed functions is equivalent to the convolution product of the two functions in the time domain, $F(t)$ is obtained from Equation (D.15) as

$$F(t) = \int_0^t \bar{Y}(t-\tau)\frac{\mathrm{d}P(\tau)}{\mathrm{d}\tau}\mathrm{d}\tau \tag{D.16}$$

with $P(t)$ representing the load history.

Since indentation tests are commonly conducted under load control, Equation (D.16) is specified to the trapezoidal load history depicted in Figure D.2(a), reading

$$P(t) = \begin{cases} P_{\mathrm{L}}(t) = t/\tau_{\mathrm{L}}P_{\mathrm{max}} \text{ for } 0 \leq t \leq \tau_{\mathrm{L}} \\ P_{\mathrm{H}}(t) = P_{\mathrm{max}} \text{ for } \tau_{\mathrm{L}} \leq t \leq \tau_{\mathrm{L}} + \tau_{\mathrm{H}} \\ P_{\mathrm{U}}(t) = (\tau_{\mathrm{L}} + \tau_{\mathrm{H}} + \tau_{\mathrm{U}} - t)/\tau_{\mathrm{U}}P_{\mathrm{max}} \\ \quad \text{for } \tau_{\mathrm{L}} + \tau_{\mathrm{H}} \leq t \leq \tau_{\mathrm{L}} + \tau_{\mathrm{H}} + \tau_{\mathrm{U}} \end{cases} \tag{D.17}$$

where τ_{L}, τ_{H}, and τ_{U} are the loading, holding, and unloading durations, respectively. Considering the load history $P(t)$ given in Equation (D.17) in Equation (D.16), the function $F(t)$ becomes for the loading and holding regime

$$\begin{aligned} F_{\mathrm{L}}(t) &= \int_0^t \bar{Y}(t-\tau)\frac{\mathrm{d}}{\mathrm{d}\tau}P_{\mathrm{L}}(\tau)\mathrm{d}\tau \\ &= \frac{P_{\mathrm{max}}}{\tau_{\mathrm{L}}}\int_0^t \bar{Y}(t-\tau)\mathrm{d}\tau \end{aligned} \tag{D.18}$$

$$\begin{aligned} F_{\mathrm{H}}(t) &= \int_0^{\tau_{\mathrm{L}}} \bar{Y}(t-\tau)\frac{\mathrm{d}}{\mathrm{d}\tau}P_{\mathrm{L}}(\tau)\mathrm{d}\tau + \int_{\tau_{\mathrm{L}}}^t \bar{Y}(t-\tau)\frac{\mathrm{d}}{\mathrm{d}\tau}P_{\mathrm{H}}(\tau)\mathrm{d}\tau \\ &= \frac{P_{\mathrm{max}}}{\tau_{\mathrm{L}}}\int_0^{\tau_{\mathrm{L}}} \bar{Y}(t-\tau)\mathrm{d}\tau \end{aligned} \tag{D.19}$$

Based on F_{L} and F_{H} in Equations (D.18) and (D.19), the history of the penetration, $h(t)$, for the loading and holding time is determined in three steps:

1. First, the indentation compliance function $\bar{Y}(t)$ appearing in Equations (D.18) and (D.19) is determined for the considered viscoelastic model. In the case of elastic material response, the indentation modulus M can be expressed by the bulk modulus K and the shear modulus μ_0, reading

$$
\begin{aligned}
M &= \frac{E}{1-\nu^2} = \frac{\frac{9K\mu_0}{3K+\mu_0}}{1-\left(\frac{3K-2\mu_0}{6K+2\mu_0}\right)^2} \\
&= 4\mu_0\frac{3K+\mu_0}{3K+4\mu_0}
\end{aligned}
\tag{D.20}
$$

In order to determine material parameters for bitumen from NI test data, the indentation modulus M (see Equation (D.20)) is specialized for incompressible materials, with $K = \infty$, giving

$$
M = 4\mu_0
\tag{D.21}
$$

Applying the method of functional equations (Lee and Radok 1960), the elastic constant μ_0 in Equation (D.21) is replaced by the associated Laplace transformed operator $\widehat{\mu(s)}$, reading

$$
\widehat{M(s)} = 4\widehat{\mu(s)}
\tag{D.22}
$$

For the power-law (PL) model $\widehat{\mu(s)}$ is obtained as (see, e.g., Findley et al. (1989)):

$$
\begin{aligned}
\widehat{\mu_{\mathrm{PL}}(s)} &= (s\mathcal{L}\{J_{\mathrm{PL}}\})^{-1} \\
&= \left(s\mathcal{L}\left\{J_0 + J_{\mathrm{a}}\left(\frac{t}{\bar{\tau}}\right)^k\right\}\right)^{-1} \\
&= \left(J_0 + J_{\mathrm{a}}\frac{1}{s^k\bar{\tau}^k}\Gamma(1+k)\right)^{-1}
\end{aligned}
\tag{D.23}
$$

where $\mathcal{L}\{\bullet(t)\}$ denotes the Laplace transformation of $\bullet(t)$. Considering $\widehat{M(s)}$ of the PL model given in Equations (D.22) and (D.23) and applying the inverse Laplace transformation to $\widehat{\bar{Y}(s)} = 1/(s\widehat{M(s)})$, the indentation compliance function $\bar{Y}(t)$ is obtained as

$$
\bar{Y}_{\mathrm{PL}}(t) = \frac{1}{4}\left(J_0 + J_{\mathrm{a}}\left(\frac{t}{\bar{\tau}}\right)^k\right) = \frac{1}{4}J_{\mathrm{PL}}
\tag{D.24}
$$

2. Secondly, considering the indentation compliance function $\bar{Y}(t)$ for the PL model (Equation (D.24)) in Equations (D.18) and (D.19), the function $F(t)$ is obtained for

the loading and holding regime, $F_{\text{L}}(t)$ and $F_{\text{H}}(t)$, as

$$
\begin{aligned}
F_{\text{L-PL}}(t) &= \frac{P_{\max}}{\tau_{\text{L}}} \int_0^t \bar{Y}(t-\tau)\mathrm{d}\tau \\
&= \frac{P_{\max}}{4\tau_{\text{L}}} \left\{ J_0 t + J_{\text{a}} \frac{1}{(k+1)} \left(\frac{1}{\bar{\tau}}\right)^k t^{k+1} \right\}
\end{aligned}
\tag{D.25}
$$

$$
\begin{aligned}
F_{\text{H-PL}}(t) &= \frac{P_{\max}}{\tau_{\text{L}}} \int_0^{\tau_{\text{L}}} \bar{Y}(t-\tau)\mathrm{d}\tau \\
&= \frac{P_{\max}}{4\tau_{\text{L}}} \left\{ J_0 \tau_{\text{L}} + J_{\text{a}} \frac{1}{(k+1)} \left(\frac{1}{\bar{\tau}}\right)^k \left[t^{k+1} - (t-\tau_{\text{L}})^{k+1} \right] \right\}
\end{aligned}
\tag{D.26}
$$

Taking into account that the nlDP model is obtained from the PL model by setting J_0 equal to zero, $F_{\text{L-nlDP}}(t)$ and $F_{\text{H-nlDP}}(t)$ are obtained as

$$
F_{\text{L-nlDP}}(t) = \frac{P_{\max}}{4\tau_{\text{L}}} \left\{ J_{\text{a}} \frac{1}{(k+1)} \left(\frac{1}{\bar{\tau}}\right)^k t^{k+1} \right\}
\tag{D.27}
$$

$$
F_{\text{H-nlDP}}(t) = \frac{P_{\max}}{4\tau_{\text{L}}} \left\{ J_{\text{a}} \frac{1}{(k+1)} \left(\frac{1}{\bar{\tau}}\right)^k \left[t^{k+1} - (t-\tau_{\text{L}})^{k+1} \right] \right\}
\tag{D.28}
$$

3. Finally, the history of the contact radius, $a(t)$, is obtained from combining the expressions for $F_{\text{L}}(t)$ and $F_{\text{H}}(t)$ given in Equations (D.25) to (D.28) with Equation (D.12). The so-obtained (nonlinear) expression for $a(t)$ is solved numerically. With $a(t)$ at hand, the history of the penetration, $h(t)$, is given by Equation (D.10) for a given load history $P(t)$ and the material model describing the behavior of the viscoelastic halfspace.

Concluding remarks

The publications presented in this thesis dealt with the development of novel methods for the identification of viscoelastic parameters by means of nanoindentation (Publications A, B, and C) and with the microscale characterization of bitumen (Publication D). As regards the presented methods for the identification of model parameters, the main findings can be summarized as:

1. The results from Publication A showed, that the tip roundness significantly influences the penetration history (see Figure A.5). The difference in penetration obtained for the real tip shape and the perfect tip shape is most pronounced for small penetration depths and decreases with increasing penetration. Since parameter identification is based on back-calculation by comparing the experimentally-obtained penetration history with the model response, this difference also influences the obtained model parameters. Figure D.19, showing the variation of the fractional dash-pot parameters for increasing tip roundness, highlights the importance of a proper consideration of the real tip shape in the course of parameter identification by means of nanoindentation.
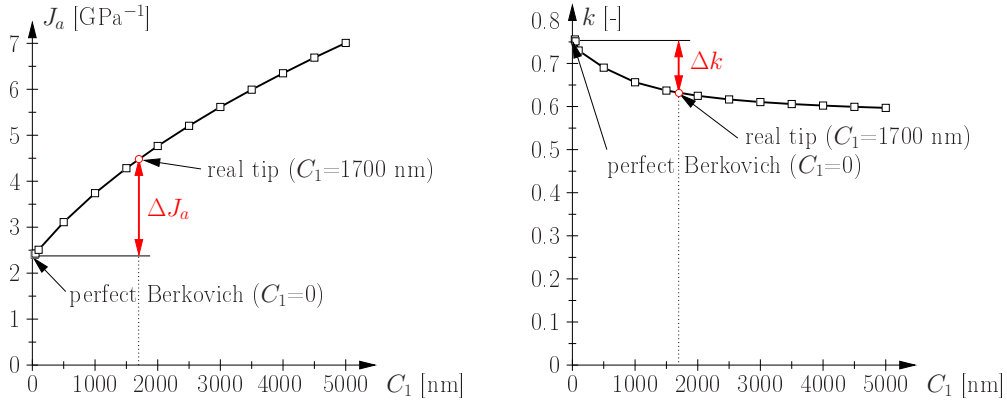

Figure D.19: Influence of tip shape parameter C_1 (which is directly related to the tip radius) on identified fractional dash-pot parameters J_a and k for a given penetration history

2. As shown in Publication B, neglecting plastic deformation in the course of parameter identification of materials exhibiting in addition to viscoelastic also plastic material response significantly influences the obtained viscoelastic parameters. In this case, the plastic deformation is assigned to the viscoelastic response, leading to wrong model parameters overestimating the viscoelastic deformation. Since the amount of plastic deformation for a specific material is a priori not known, the presented double-indentation technique should be employed first, allowing consideration of the effect of plastic deformation. If the amount of plastic deformation is found to be negligible in comparison to the viscoelastic deformation (small values for the residual penetration h_r, see Figure B.1), as for bitumen, the conventional single-indentation technique may still be applied.

   Use of spherical indenter geometries instead of commonly employed pyramidal indenters reduces the stresses under the tip and, hence, avoids plastic deformation at all. However, for certain mechanical properties of the material sample, plastic deformation may still occur in case of small tip radii and high values for the maximum load. Again, this can be assessed by application of the double-indentation technique.

3. In Publication C, viscoelastic model parameters were determined by comparing the experimentally-obtained storage and loss moduli with the respective analytical expressions for the underlying viscoelastic model. In case of the employed cyclic tests, the selection of the viscoelastic model is performed in the Cole-Cole plot (see Figure D.20) by comparing the experimental results with the respective analytical expressions for the different viscoelastic models.
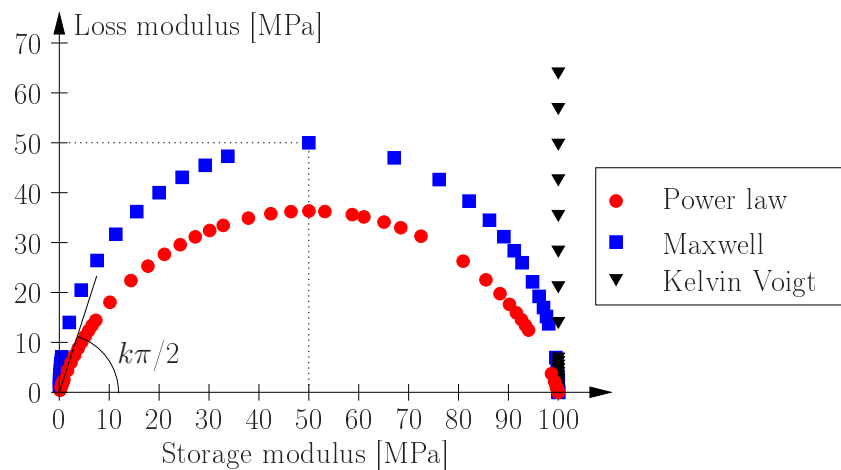

Figure D.20: Cole-Cole plot for different viscoelastic models to be compared with experimental data (see Publication C for the respective analytical expressions for storage and loss moduli)

Comparing all presented methods, one can conclude, that the double-indentation technique, the use of spherical indenter geometries, and the application of cyclic nanoindentation are suitable for back-calculation of viscoelastic properties. Figure D.21 shows a behavior map of viscoelastic-plastic materials and recommendations regarding the parameter-identification method. For materials exhibiting a low resistance to plastic deformation, either spherical tips using the single-indentation method or conical tips using the double-indentation method should be employed for parameter identification. However, the presented single-indentation technique, considering the real tip shape, as well as cyclic nanoindentation may still be applied in the special case of negligible plastic deformation.
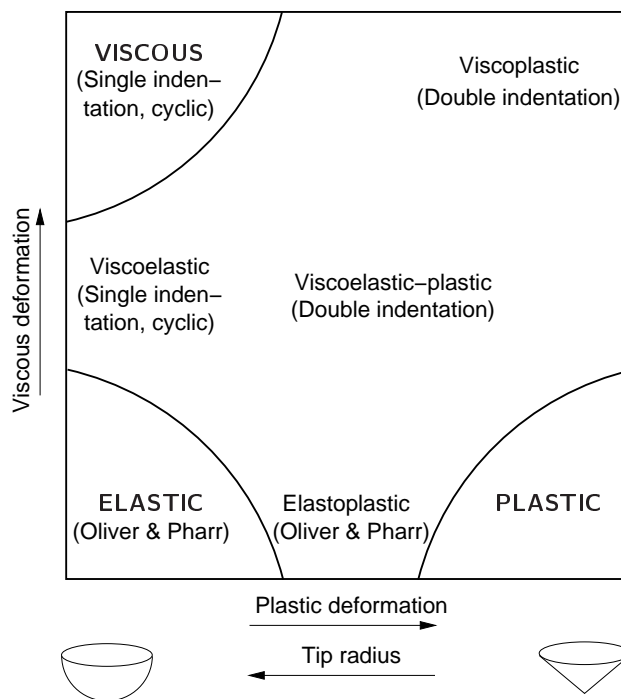

Figure D.21: Schematic behavior map of viscoelastic-plastic materials and recommended parameter-identification method by means of nanoindentation

Bibliography

Abramowitz, M. and Stegun, I. (1972). *Handbook of Mathematical Functions, With Formulas, Graphs, and Mathematical Tables*. Dover, New York.

Aigner, E. and Lackner, R. (2007). Micormechanics-based determination of viscous properties of asphalt concrete. *Journal for Materials in Civil Engineering ASCE*. submitted for publication.

Aigner, E., Lackner, R., and Pichler, C. (2007). 'Bottom-up' multiscale modeling of viscoelastic properties of asphalt. In Loizos, A., Scarpas, T., and Al-Quadi, I., editors, *Proceedings of the International Conference on Advanced Characterisation of Pavement and Soil Engineering Mechanics Volume 1*, pages 123–135. Taylor & Francis Group.

ASTM D5291 (2002). *Standard test method for instrumental determination of carbon, hydrogen and nitrogen in petroleum products and lubricants*. ASTM International, West Conshohocken.

Cheng, L., Xia, X., Scriven, L., and Gerberich, W. (2005). Spherical-tip indentation of viscoelastic material. *Mechanics of Materials*, 37:213–226.

Cheng, L., Xia, X., Yu, W., Scriven, L., and Gerberich, W. (2000). Flat-punch indentation of viscoelastic material. *Journal of Polymer Science: Part B: Polymer Physics*, 38:10–22.

Cheng, Y.-T. and Cheng, C.-M. (2004). Scaling, dimensional analysis, and indentation measurements. *Materials Science and Engineering R*, 44:91–149.

Cheremisinoff, N. (1989). *Handbook of Polymer Science and Technology: Performance Properties of Plastics and Elastomers*, volume 2. Marcel Dekker Inc., New York.

Constantinides, G., Ravi, K., Ulm, F.-J., and Van Vliet, K. (2006). Grid indentation analysis of composite microstructure and mechanics: Principles and validation. *Material Science and Engineering: A*, 430(1-2):189–202.

EN 12607-1 (1999). *Bitumen and bituminous binders – Determination of the resistance to hardening under the influence of heat and air – Part 1: RTFOT method*. European committee for standardization, Brussels.

Findley, W., Lai, J., and Onaran, K. (1989). *Creep and relaxation of nonlinear viscoelastic materials.* Dover Publications, New York.

Füssl, J., Lackner, R., Eberhardsteiner, J., and Mang, H. (2008). Failure modes and effective strength of two-phase materials determined by means of numerical limit analysis. *Acta Mechanica*, 195:185–202.

Goodman, L. and Keer, L. (1965). The contact stress problem for an elastic sphere indenting an elastic cavity. *International Journal of Solids and Structures*, 1:407–415.

Graham, G. (1965). The contact 426 problem in the linear theory of viscoelasticity. *International Journal of Engineering Science*, 3(1):27–46.

Graham, G. (1967). Contact problem in linear theory of viscoelasticity when time dependent contact area has any number of maxima and minima. *International Journal of Engineering Science*, 5(6):495–514.

Hayes, S., Goruppa, A., and Jones, F. (2004). Dynamic nanoindentation as a tool for the examination of polymeric materials. *Journal of Materials Research*, 19(11):3298–3306.

Hobson, G. (1984). *Modern petroleum technology, Part II*, volume 5. The Institute of Petroleum, London.

Hunter, S. (1960). The hertz problem for a rigid spherical indenter and a viscoelastic half-space. *Journal of the Mechanics and Physics of Solids*, 8(219–234).

Hysitron Inc. (2006). *Triboindenter User Manual.* Minneapolis, MN.

Jäger, A. (2004). Microstructural identification of bitumen by means of atomic force microscopy (AFM), modulated differential scanning calorimetry (MDSC), and reflected light microscopy (RLM). Master's thesis, Vienna University of Technology, Vienna.

Jäger, A. and Lackner, R. (2007). Finer-scale extraction of viscoeasltic properties from nanoindentation characterized by viscoelastic-plastic response. *Strain.* accepted for publication.

Jäger, A. and Lackner, R. (2008). Identification of viscoelastic model parameters by means of cyclic nanoindentation testing. *International Journal of Materials Research.* accepted for publication.

Jäger, A., Lackner, R., and Eberhardsteiner, J. (2007a). Identification of viscoelastic properties by means of nanoindentation taking the real tip geometry into account. *Meccanica*, 42:293–306.

Jäger, A., Lackner, R., and Stangl, K. (2007b). Microscale characterization of bitumen – back-analysis of viscoelastic properties by means of nanoindentation. *International Journal of Materials Research*, 98(5):404–413.

Johnson, K. (1992). *Contact Mechanics.* Cambridge University Press, Cambridge.

Kappl, K. (2007). *Bewertung und Modellierung des Verformungsverhaltens von Asphalten mit Hilfe zyklischer Triaxialprüfungen, [Assessment and modelling of permanent deformation behaviour of bituminous mixtures with triaxial cyclic compression tests].* PhD thesis, Vienna University of Technology, Faculty of Civil Engineering. In German.

Krabbenhoft, K., Lyamin, A., Hjiaj, M., and Sloan, S. (2005). A new discontinuous upper bound limit analysis formulation. *International Journal for Numerical Methods in Engineering*, 63(7):1069–1088.

Lackner, R., Blab, R., Jäger, A., Spiegl, M., Kappl, K., Wistuba, M., Gagliano, B., and Eberhardsteiner, J. (2004). Multiscale modeling as the basis for reliable predictions of the behavior of multi-composed materials. In Topping, B. and Mota Soares, C., editors, *Progress in Computational Structures Technology*, pages 153–187. Saxe-Coburg Publications, Stirling.

Lackner, R., Spiegl, M., Blab, R., and Eberhardsteiner, J. (2005). Is low-temperature creep of asphalt mastic independent of filler shape and mineralogy? – Arguments from multiscale analysis. *Journal of Materials in Civil Engineering (ASCE)*, 17(5):485–491.

Larrson, P. and Carlsson, S. (1998). On microindentation of viscoelastic polymers. *Polymer Testing*, 17(1):49–75.

Lee, E. (1955). Stress analysis in visco-elastic bodies. *Quarterly of Applied Mathematics*, 13:183–190.

Lee, E. and Radok, J. (1960). The contact problem for viscoelastic bodies. *Journal of Applied Mechanics*, 27:438–444.

Li, X. and Bhushan, B. (2002). A review of nanoindentation continuous stiffness measurement technique and its applications. *Materials Characterization*, 48:11–36.

Loubet, J., Lucas, B., and Oliver, W. (1995). Some measurements of viscoelastic properties with the help of nanoindentation. In Smith, D., editor, *International Workshop on Instrumented Indentation*, pages 31–34.

Lu, H., Wang, B., Ma, J., Huang, G., and Viswanathan, H. (2003). Measurements of creep compliance of solid polymers by nanoindentation. *Mechanics of Time-Dependent Materials*, 7:189–207.

Makrodimopoulos, A. and Martin, C. (2006). Lower bound limit analysis of cohesive-frictional materials using second-order cone programming. *International Journal of Numerical Methods in Engineering*, 66(4):604–634.

matweb (2007). *http://www.matweb.com.*

Mori, T. and Tanaka, K. (1973). Average stress in matrix and average elastic energy of materials with misfitting inclusions. *Acta Metallurgica*, 21:571–574.

Odegard, G., Gates, T., and Herring, H. (2005). Characterization of viscoelastic properties of polymeric materials through nanoindentation. *Experimental Mechanics*, 45(2):130–136.

Oliver, W. and Pharr, G. (1992). An improved technique for determining hardness and elastic modulus using load and displacement sensing indentation experiments. *Journal of Materials Research*, 7(6):1564–1583.

ÖNORM EN 12593 (2000). *Bitumen und bitumenhaltige Bindemittel – Bestimmmung des Brechpunktes nach Fraaß [Bitumen and bituminous binders – Determination of the Fraass breaking point]*. Österreichisches Normungsinstitut, Vienna. In German.

ÖNORM EN 1426 (2000). *Bitumen und bitumenhaltige Bindemittel – Bestimmmung der Nadelpenetration [Bitumen and bituminous binders – Determination of needle penetration]*. Österreichisches Normungsinstitut, Vienna. In German.

ÖNORM EN 1427 (2000). *Bitumen und bitumenhaltige Bindemittel – Bestimmmung des Erweichungspunktes – Ring- und Kugel-Verfahren [Bitumen and bituminous binders – Determination of softening point – Ring and Ball method]*. Österreichisches Normungsinstitut, Vienna. In German.

Oyen, M. (2005). Spherical indentation creep following ramp loading. *Journal of Materials Research*, 20(8):2094–2100.

Oyen, M. and Cook, R. (2003). Load-displacement behavior during sharp indentation of viscous-elastic-plastic materials. *Journal of Materials Research*, 18(8):139–150.

Oyen, M., Cook, R., Emerson, J., and Moody, N. (2004). Indentation response of time-dependent films on stiff substrates. *Journal of Materials Research*, 19(8):2487–2497.

Park, K., Mishra, S., Lewis, G., Losby, J., Fan, Z., and Park, J. (2004). Quasi-static and dynamic nanoindentation studies on highly crosslinked ultra-high-molecular-weight polyethylene. *Biomaterials*, 25:2427–2436.

Partal, P., Martinez-Boza, F., Conde, B., and Gallegos, C. (1999). Rheological chracterization of synthetic binders and unmodified bitumens. *Fuel*, 78:1–10.

Perrson, A. (1964). *On the stress distribution on cylindrical elastic bodies in contact*. PhD thesis, Chalmers Tekniska Hogskola, Göteborg.

Pethica, J. and Oliver, W. (1987). Tip surface interactions in STM and AFM. *Physica Scripta*, T19:61–66.

Pharr, G. and Bolshakov, A. (2002). Understanding nanoindentation unloading curves. *Journal of Materials Research*, 17(10):2660–2671.

prEN 14769 (2003). *Bitumen and bituminous binders – Accelerated long-term ageing – Pressure ageing vessel (PAV)*. European committee for standardization, Brussels.

Press, W., Teukolsky, S., Vetterling, W., and Flannery, B. (1996). *Numerical Recipes in Fortran 77: The Art of Scientific Computing*, volume 1 of *Fortran Numerical Recipes*. Cambridge University Press, Cambridge.

Radok, J. (1957). Visco-elastic stress analysis. *Quarterly of Applied Mathematics*, 15:189–202.

Rozeveld, S., Shin, E., Bhurke, A., France, L., and Drzal, L. (1997). Network morphology of straight and polymer modified asphalt cements. *Microscopy Research and Technique*, 38:529–543.

Sakai, M. (2002). Time-dependent viscoelastic relation between load and penetration for an axisymmetric indenter. *Philosophical Magazine A*, 82(10):1841–1849.

Sakai, M. (2003). Elastic recovery in the unloading process of pyramidal microindentation. *Journal of Materials Research*, 18(7):1631–1640.

Sakai, M. and Shimizu, S. (2001). Indentation rheometry for glass-forming materials. *Journal of Non-Crystalline Solids*, 282:236–247.

Sakai, M., Shimizu, S., and Ito, S. (2002). Viscoelastic indentation of silicate glasses. *Journal of the American Ceramic Society*, 85(5):1210–1216.

Shell-Bitumen-U.K. (1990). *The Shell bitumen handbook*, volume 1. Shell Bitumen UK, Chertsey.

Shimizu, S., Yanagimoto, T., and Sakai, M. (1999). Pyramidal indentation load depth curve of viscoelastic materials. *Journal of Materials Research*, 14(10):4075–4086.

Sneddon, I. (1965). The relation between load and penetration in the axisymmetric Boussinesq problem for a punch of arbitrary profile. *International Journal of Engineering Science*, 3:47–57.

Spiegl, M. (2007). *Tieftemperaturverhalten von bituminsen Baustoffen - labortechnische Ansprache und numerische Simulation des Gebrauchsverhaltens [Low-temperature behavior of bituminous materials - assessment of performance behavior by means of laboratory testing and numerical simulation]*. PhD thesis, Vienna University of Technology, Faculty of Civil Engineering. In German.

Stangl, K., Jäger, A., and Lackner, R. (2006). Microstructure-based identification of bitumen performance. *International Journal of Road Materials and Pavement Design*, 7:111–142.

Steuermann, E. (1939). On hertz theory of local deformation of compressed bodies. *Comptes rendues (Doklady) de lAcademie des Sciences de lURSS*, 25:359–361.

Stilwell, N. and Tabor, D. (1961). Elastic recovery of conical indentations. *Proceedings of the Physical Society*, 78:169–179.

Syed Asif, S., Wahl, K., and Colton, R. (1999). Nanoindentation and contact stiffness measurement using force modulation with a capacitive load-displacement transducer. *Review of Scientific Instruments*, 70(5):2408–2413.

Syed Asif, S., Wahl, K., Colton, R., and Warren, O. (2001). Quantitative imaging of nanoscale mechanical properties using hybrid nanoindentation and force modulation. *Journal of Applied Physics*, 90(3):1192–1200.

Thurn, J. and Cook, R. (2002). Simplified area function for sharp indenter tips in depth-sensing indentation. *Journal of Materials Research*, 17(5):1143–1146.

Ting, T. (1966). The contact stress between a rigid indenter and a viscoelastic half-pace. *Journal of Applied Mechanics*, 33:845–854.

Ting, T. (1968). Contact problems in linear theory of viscoelasticity. *Journal of Applied Mechanics*, 35:248–254.

Ulm, F.-J., Delafargue, A., and Constantinides, G. (2005). Experimental microporomechanics. In L. Dormieux, F.-J. U., editor, *Applied Micromechanics of Porous Materials (CISM Courses and Lectures No. 480)*, Vienna. Springer.

Vandamme, M. and Ulm, F.-J. (2006). Viscoelastic solutions for conical indentation. *International Journal of Solids and Structures*, 43(10):3142–3165.

White, C., Vanlandingham, M., Drzal, P., Chang, N.-K., and Chang, S.-H. (2005). Viscoelastic characterization of polymers using instrumented indentation. ii. dynamic testing. *Journal of Polymer Science: Part B: Polymer Physics*, 43:1812–1824.

Yang, W. (1966). Contact problem for viscoelastic bodies. *Journal of Applied Mechanics*, 33:395–401.

Zhang, C. Y., Zhang, Y.W., Zeng, K.Y., and Shen, L. (2005). Nanoindentation of polymers with a sharp indenter. *Journal of Materials Research*, 20(6):1597–1605.

Curriculum Vitae
Dipl.-Ing. Andreas JÄGER

Personal Data

Name:	Andreas Jäger
Academic Degree:	Dipl.-Ing.
Date of Birth:	1.12.1977
Place of Birth:	Melk, Austria
Citizenship:	Austria

Education

09/1992 – 06/1997	Höhere Technische Bundeslehranstalt Krems, Krems, Austria
	VET College in Civil Engineering
	Graduation with distinction
10/1998 – 04/2004	Vienna University of Technology, Vienna, Austria
	Diploma studies in Civil Engineering
	Graduation with distinction
05/2004 – 03/2008	Vienna University of Technology, Vienna, Austria
	Doctoral studies
	Dissertation at the Institute for Mechanics of Materials and Structures

Work Experience

10/1997 – 05/1998	Military service in Melk
07/1998 - 08/1998	Franz Chlastak, architect, Vienna
07/1999 - 08/1999	IC-Konsulenten, civil engineers, Vienna
07/2000 - 08/2000	IC-Konsulenten, civil engineers, Vienna
04/2001 - 09/2001	magk, architects, Vienna
07/2002 - 09/2002	Johannes Unterreiter, civil engineer, Völkermarkt
05/2004 – present	Vienna University of Technology, Vienna, Austria
	Research assistant at the Institute for Mechanics of
	Materials and Structures
	Scientific staff at the Christian Doppler Laboratory for
	Performance Based Optimization of Flexible Pavements